CryoEM Structural Analysis of Pannexin 1 Channels

Xueyao Jin
Fushun, China

B.S. Biological Science, Lanzhou University, China, 2010

A Dissertation presented to the Graduate Faculty
of the University of Virginia in Candidacy for the Degree of
Doctor of Philosophy

Department of Molecular Physiology and Biological Physics

University of Virginia
July, 2018

© 2018 Xueyao Jin

All rights reserved

Abstract

Pannexin 1 (Panx1) is a tetra-spanning, oligomeric, ubiquitously expressed, single membrane protein channel that mediates nucleotides such as ATP release upon activation. Panx1 channels are involved in diverse physiological and pathological processes such as blood pressure regulation, apoptotic cell clearance, inflammation, neurological disorders, and cancer progression and metastasis. Panx1 channels can be activated by various mechanisms including mechanical stress, increased extracellular potassium or intracellular calcium, receptor-mediated signaling pathways, and caspase cleavage of the distal C-terminus. Despite extensive knowledge about the physiology of Panx1 channels, there is much to learn about their structure and molecular basis for channel regulation.

We use negative-stain electron microscopy (EM) and electrophysiology to explore the conformational changes and channel property associated with caspase cleavage-mediated activation. We find that Panx1 channels activated by caspase cleavage display a prominent ‘pore’, voltage-independent gating and outwardly rectifying unitary conductance (<100 pS) at depolarized potentials. Our results support the model that caspase cleavage activates Panx1 channel by removing the pore-associated C-terminal autoinhibitory tails.

We use single-particle electron cryomicroscopy (cryoEM) and electrophysiology to investigate the structure and function of Panx1 channels. We determined the three-dimensional (3D) structure of lipid nanodisc-embedded, C-terminally truncated frog Panx1 at 7 Å resolution. The 3D reconstruction reveals that Panx1 is a heptameric channel, with seven subunits surrounding a central seven-fold symmetric pore axis. The oligomeric state differs from hexameric connexin and octameric innexin hemichannels. A large entrance vestibule resides at the cytoplasmic surface, whereas the extracellular surface displays a narrow pore. The 3D reconstruction clearly resolves the transmembrane (TM) α-helices, which fold as a 4-helix bundle in each subunit. The 4-helix bundle structure of Panx1 recapitulates a similar subunit design with other oligomeric, tetra-spanning membrane protein channels such as connexins (Cxs), innexins (Inxs) and leucine-rich repeat-containing 8 (LRRC8) channels. Rigid body fitting reveals that the monomeric structure of Panx1 resembles LRRC8A channel more than INX-6. Electrophysiological recordings show that the C-terminally truncated Panx1 channels are in a closed conformation, which can be activated by the α1D adrenoceptor-mediated signaling pathway. This result suggests that activation of the α1D adrenoceptor results in phosphorylation of a cytoplasmic site on Panx1 that elicits a transmembrane conformational change to open the extracellular gate. Our work reveals the previously unknown architecture of pannexin channels with respect to the oligomeric state (heptameric), channel and pore dimensions, and the arrangement of the TM helices in each subunit.

Table of Contents

Abbreviations

2D: two-dimensional

3D: three-dimensional

α1DR: α1 adrenergic receptor

ATP: adenosine triphosphate

β-ME: β-mercaptoethanol

BLASTP: basic local alignment search tool program

BSA: bovine serum albumin

Ca^{2+}: calcium ion

CALHM1: calcium homeostasis modulator 1

cAMP: cyclic adenosine monophosphate

CBX: carbenoxolone

CCD: charge-coupled device

CCR5: C-C chemokine receptor type 5

CD: circular dichroism

CD4: cluster of differentiation 4

C. elegans: Caenorhabditis elegans

CHS: cholesterol hemisuccinate

CL: cytoplasmic loop

CMC: critical micellar concentration

CNS: central nervous system

CO_2: carbon dioxide

CPM: 7-diethylamino-3-(4'-maleimidylphenyl)-4-methylcoumarin

cryoEM: electron cryomicroscopy

CT: carboxyl terminus

CTF: contrast transfer function

Cx: connexin

CXCR-4: C-X-C chemokine receptor type 4

DDM: n-dodecyl-β-D-maltopyranoside

DFA: differential filtration assay

DIDS: 4,4'-Diisothiocyano-2,2'-stilbenedisulfonic acid

DM: n-decyl-β-D-maltopyranoside

DQE: detective quantum efficiency

DSP: dithio-*bis*(succinimidylpropionate)

E. coli: Escherichia coli

EDTA: ethylenediaminetetraacetic acid

EGFP: enhanced green fluorescent protein

EL: extracellular loop

EM: electron microscopy

ER: endoplasmic reticulum

Fab: Fragment antigen-binding

FFA: fluefenamic acid

FSC: fourier shell correlation

FSEC: fluorescent size-exclusion chromatography

FTSA: fluorescent thermal stability assay

GJC: gap junction channel

GPCR: G-protein coupled receptor

HC: hemichannel

HEK: human embryonic kidney

HEPES: (4-(2-hydroxyethyl)-1-piperazineethanesulfonic acid

HIV: human immunodeficiency virus

HPLC: high-pressure liquid chromatography

IBD: inflammatory bowel disease

IMAC: immobilized metal affinity chromatography

$InsP_3$: inositol 1,4,5-trisphosphate

I-V: current-voltage

Inx: innexin

JNK: c-Jun NH(2)-terminal kinase

K^+: potassium ion

LMNG: lauryl maltose neopentyl glycol

LRRC8: leucine-rich repeat-containing 8

LRRD: leucine-rich repeat domain

MALDI-MS: matrix-assisted laser desorption ionization mass spectrometry

MDCK: Madin-Darby canine kidney

MOI: multiplicity of infection

MSP2N2: membrane scaffold protein 2N2

MWCO: molecular weight cut-off

N2A: neuroblastoma 2A

NMDA: *N*-methyl-D-aspartate receptor

NO: nitric oxide

NT: amino terminus

OG: n-octyl-β-D-glucopyranoside

OGD: oxygen and glucose deprivation

Panx: pannexin

PAR: protease-activated receptor

PBS: phosphate buffered saline

PD: pore domain

PDB: protein data bank

PE: phenylephrine

PKG: protein kinase G

PNGaseF: peptide:N-glycosidase F

pS: picosiemens

PSI-BLAST: position-specific iterative basic local alignment search tool

RI: refractive index

RMSD: root-mean-square deviation

SCAM: substituted cysteine accessibility method

SDS-PAGE: sodium dodecylsulfate polyacrylamide gel electrophoresis

SEC: size exclusion chromatography

SEC-MALS: size exclusion chromatography with multi-angle light scattering

Sf9: *Spodoptera frugiperda*

SFK: Src family kinase

T4L: T4 lysozyme

TDM: n-tridecyl-β-D-maltopyranoside

TEV: tobacco etch virus

TIRF: total internal reflection fluorescence

T_m : melting temperature

TM: transmembrane

TNF: tumor necrosis factor

Tris: tris(hydroxymethyl)aminomethane

UTP: uridine triphosphate

UV: ultraviolet

VPP: Volta phase plate

VRAC: volume-regulated anion channel

WT: wild type

Chapter 1

Introduction

1.1 Pannexin 1 membrane protein channel

1.1.1 General Introduction

Intercellular communication is crucial for the development and normal function of multicellular organisms. There are two mechanisms for intercellular communication: (1) release of small molecules such as neurotransmitters, hormones or nucleotides to the extracellular space through membrane protein channels and (2) formation of intercellular channels that directly connect the cytoplasm of two adjacent cells. These intercellular channels are called gap junction channels (GJCs), which are formed by end-to-end docking of two hemichannels (HCs) from adjacent cells, resulting in junctional structures between apposed membranes separated by a 2-4 nm gap[1]. GJCs allow direct exchange of ions and molecules such as Ca^{2+}, $InsP_3$, cAMP, glucose, glutamate and ATP, for cell-to-cell electrical coupling and metabolic communication[2-6]. Connexins (Cxs) and Innexins (Inxs) are the vertebrate and invertebrate GJCs, respectively. In spite of no amino acid sequence homology[7-11], they share similar structural and functional features.

In 2000, Panchin *et al.* identified two putative sequences in the mammalian genome with limited sequence homology (25-33% identity and up to

46% similarity) to Inxs, by performing BLASTP and PSI-BLAST searches against GenBank using innexin sequences. The newly identified vertebrate homologs of Inxs were named pannexins (Panxs), for their ubiquitous presence in multicellular animals (metazoans) and sequence similarity with Inxs (from the Latin 'pan' meaning 'all' and 'nexus' meaning 'connection')[12,13]. Nonetheless, Inxs retain their original name and are referred to non-chordate homologs ('non-chordate Panxs'). The chordate homologs ('chordate Panxs') are specified as Panxs. Neither Inxs nor Panxs share significant sequence similarity with Cxs[14,15].

1.1.2 Comparison of pannexin channels with connexin and innexin gap junction channels

Despite their lack of sequence homology, Panxs share a common membrane topology with Cxs and Inxs[16,17]. Each protein subunit contains four transmembrane (TM) domains, two extracellular loops (EL1 and EL2), one cytoplasmic loop (CL), and cytoplasmic amino terminus (NT) and carboxyl terminus (CT). Each EL contains conserved cysteine (Cys) residues (Panxs/Inxs contain two; Cxs contain three) (**Figure 1.1**). Cx, Inx and Panx subunits assemble as oligomers to form large-pore channels in the plasma membrane. The large central pore allows permeation of molecules up to 1 kDa[4,16]. Panx channels and GJCs also possess overlapping sensitivity to pharmacological blockers such as carbenoxolone (CBX) and mimetic peptides[18].

The major difference between Panxs and Cxs/Inxs is the capability of forming GJCs. Cx and Inx subunits can assemble as HCs that allow passage of molecules between cytosolic and extracellular space, as well as intercellular GJCs by end-to-end docking of two HCs from adjacent cells that allow direct cell-to-cell communication[16] (**Figure 1.1**). Since Panxs share low sequence homology to Inxs, and the same membrane topology with Cxs and Inxs, it was initially considered that Panx also formed GJCs in vertebrates[10,12,13,19]. For instances, early studies suggested that Panxs form intercellular channels using exogenous expression in paired *Xenopus* oocytes. With long pairing periods, only low levels of currents were measured[19]. Later reports suggested Panx-dependent dye coupling in glioma cells[20]. Nevertheless, it is now widely accepted that Panxs only form single plasma membrane channels, which is supported by a list of evidence[21-23]. Panxs are expressed in single cells such as erythrocytes[24]. In addition, they are also exclusively localized to the membrane regions that do not form cell-to-cell contacts such as apical membranes of airway epithelial cells[25] and kidney epithelial cells[26], postsynaptic membranes of neurons[27] and nonjunctional membranes of the heart[28]. Immunohistological staining of Panxs has shown diffuse instead of typical punctuate staining of gap junctions at cell-to-cell contact points[21,24]. As noted, there are only two conserved Cys residues within each Panx EL in comparison to three in Cxs (**Figure 1.1**). It is known that the conserved Cys residues in Cx ELs can form intramolecular disulfide bonds, which contribute to formation of a β-barrel structure for intercellular docking[29]. The lack of one pair of Cys residues may make Panxs less stable in forming

GJCs. In addition, Panx contains a unique N-linked glycosylation site at Asn residue in the EL, which has not been observed in either Cxs or Inxs[30-32] (**Figure 1.1**). Since Cx GJCs are formed by docking of two HCs from adjacent cells through interaction of their ELs[29], the carbohydrate trees on the glycosylated Panxs may prevent formation of gap junctions by sterically hindering the docking of two Panx channels. Unlike Cx HCs, which are blocked by extracellular Ca^{2+} before forming GJCs, Panx channels are not gated by extracellular Ca^{2+} [33]. Instead, they are gated by intracellular Ca^{2+} [34], indicating that Panx channels are not restricted from opening under physiological conditions.

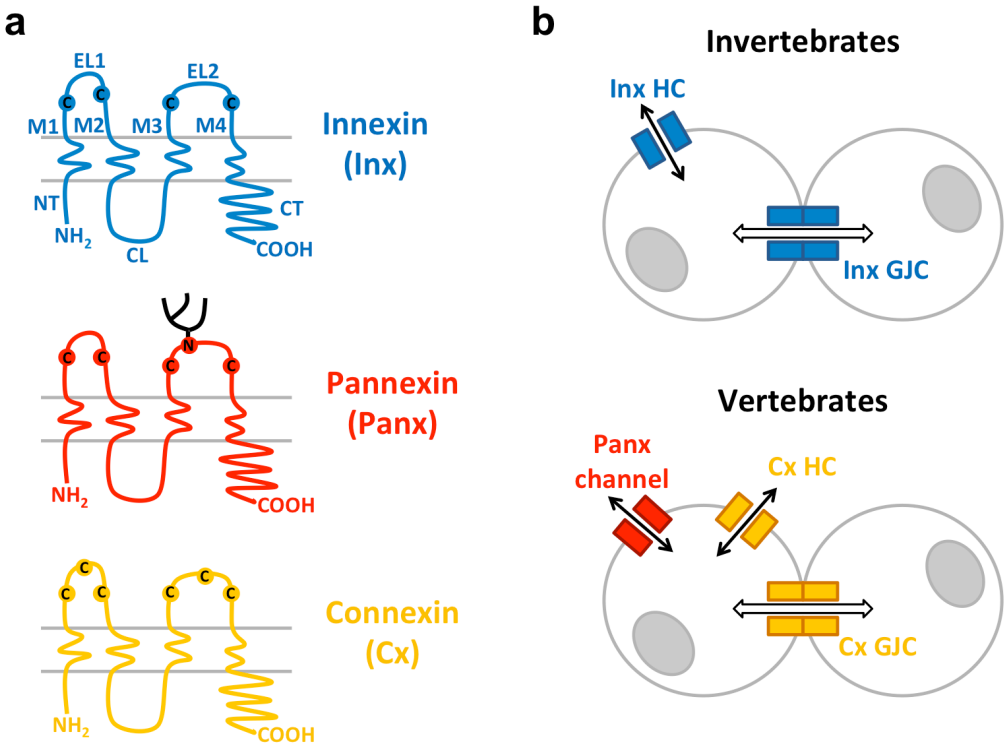

Figure 1.1. Comparison of pannexin channels with connexin and innexin gap junction channels. (a) Membrane topology of innexin, pannexin and connexin. EL1 and EL2, extracellular loops. CL, cytoplasmic loop. NT, amino terminus. CT, carboxyl terminus. M1-M4, transmembrane domains. Cys residues, 'C'. Glycosylation site Asn residue, 'N' with tree-like structure. The gray areas schematize the two lipid layers. **(b)** Pannexin (Panx), connexin (Cx) and innexin (Inx) forms different types of gap junction channels (GJCs) and hemichannels (HCs). (Figure adapted from Scemes *et al.*, 2009)[16]

1.1.3 Pannexin 1: membrane topology and oligomerization

Isotypes. There are three members in the human Panx family: Panx1 (426 aa, 47.6 kDa, chromosome 11q21), Panx2 (677 aa, 74.4 kDa, chromosome 22q13) and Panx3 (392 aa, 44.7 kDa, chromosome 11q24), which share the same tetra-spanning membrane topology[13,23] (**Figure 1.2**).

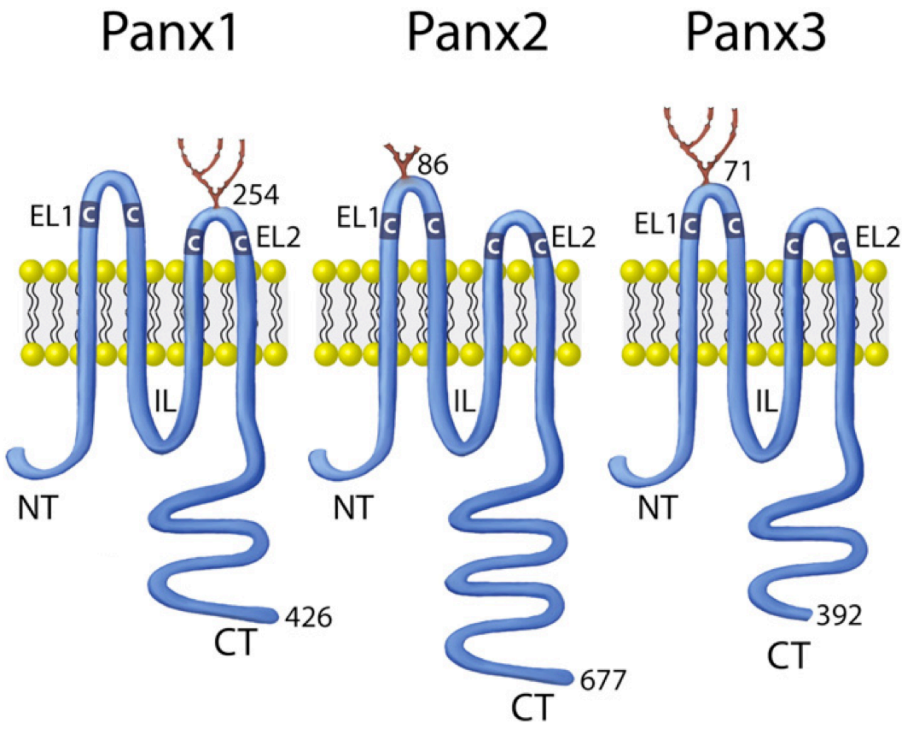

Figure 1.2. Schematic representation of the three pannexin family members. Panx1 (426), Panx2 (677) and Panx3 (392) of varying amino acid lengths are all tetra-spanning integral membrane proteins with N-glycosylation sites at amino-acid 254 (Panx1), 86 (Panx2, predicted), and 71 (Panx3). All pannexins have two cysteine residues in each extracellular loop (C). EL1, EL2 (extracellular loops 1 and 2), IL (intracellular loop), CT (carboxy-terminus) and NT (amino-terminus). (Figure and legend modified from Penuela *et al*., 2013. Reprinted from Elsevier B.V.: Biochim Biophys Acta)[35]

All three Panx paralogs are orthologous, in which Panx1 and Panx3 are more evolutionarily related, whereas Panx2 is more distantly related[13,32,36,37] (**Figure 1.3**). Panx1 is ubiquitously expressed in a wide variety of tissues such as the central nervous system (CNS), digestive system, heart, skeletal muscle, skin, endothelium, testis and ovary. Panx2 is mainly expressed in the CNS, and Panx3 is primarily restricted to bone, skin and cartilage[13,19,32].

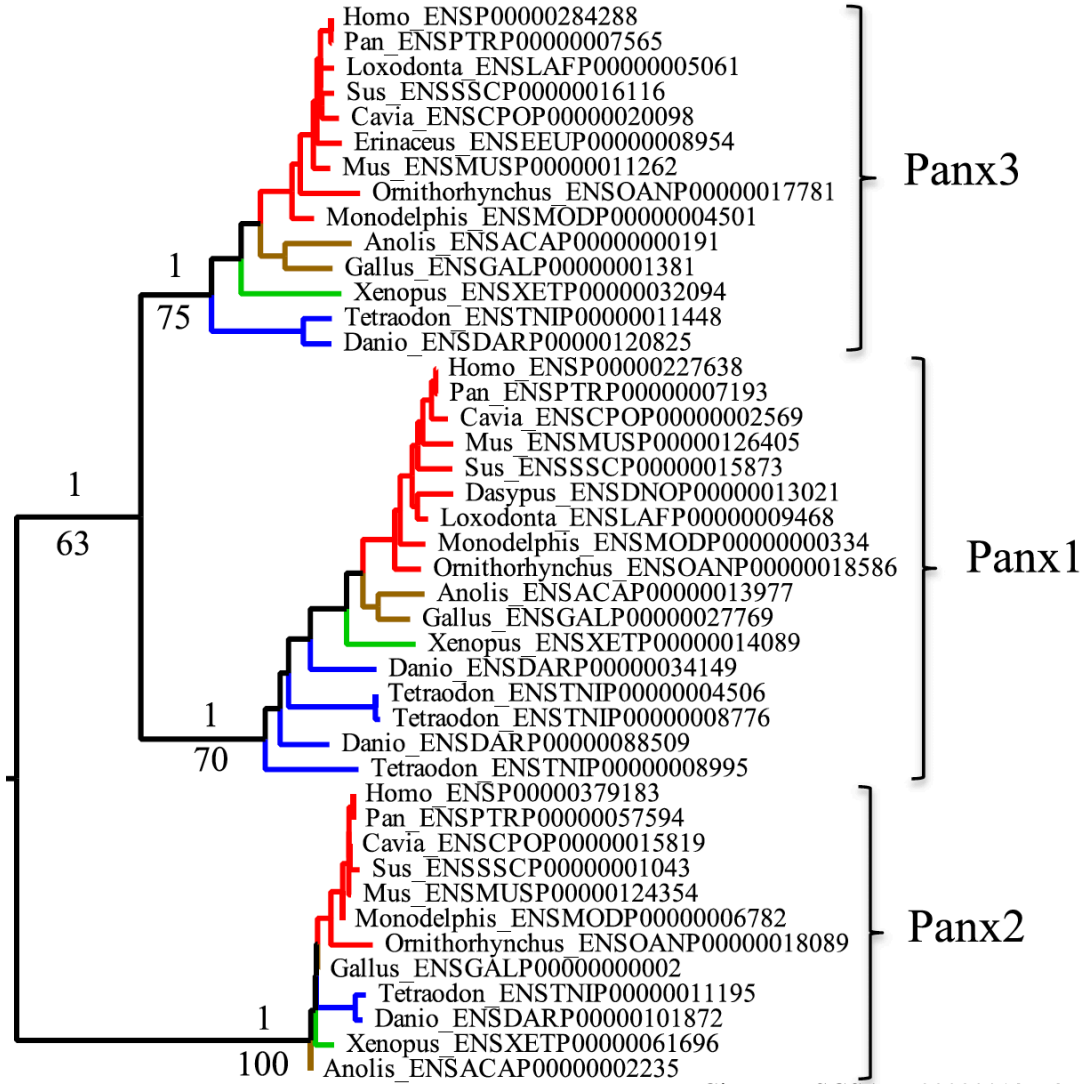

Figure 1.3. Phylogeny of pannexin protein family. Numbers above nodes, robustness of nodes assessed with Bayesian posterior probabilities. Branches are colored according to the taxonomy. (Figure and legend modified from Abascal and Zardoya, 2013. Reprinted from Elsevier B.V.: Biochim Biophys Acta)[37]

Membrane topology. As noted previously, Panx1 consists of four tansmembrane domains (TM1, TM2, TM3 and TM4) that are connected by two extracellular loops (EL1 and EL2) and one cytoplasmic loop (CL), and cytoplasmic amino (NT) and carboxyl (CT) termini [13,24,38] (**Figure 1.4**). In addition to the four TM domains in the plasma membrane, another potential membrane interacting region (I360-G370 in mouse Panx1) in the CT has also been characterized[39] (**Figure 1.4**). Four conserved cysteine residues in the ELs are necessary for the formation of functional Panx1 channels as suggested by site-directed mutagenesis experiments[40-42]. Experiments using substituted cysteine accessibility method (SCAM) have suggested that portions of TM1 and EL1 line the boundary of the channel pore, and the distal end of the CT lines the inner part of the pore[40] (**Figure 1.4**). Interestingly, structural studies on the cytoplasmic regions (NT, CL and CT), by combination of structural prediction tools and circular dichroism (CD) spectroscopy analyses, have suggested that Panx1 contains a significant amount of secondary structures (mainly in α-helices) in this region, estimated at up to 50% of the primary sequence. In contrast, the cytoplasmic regions of Cxs are primarily disordered[39] (**Figure 1.4**).

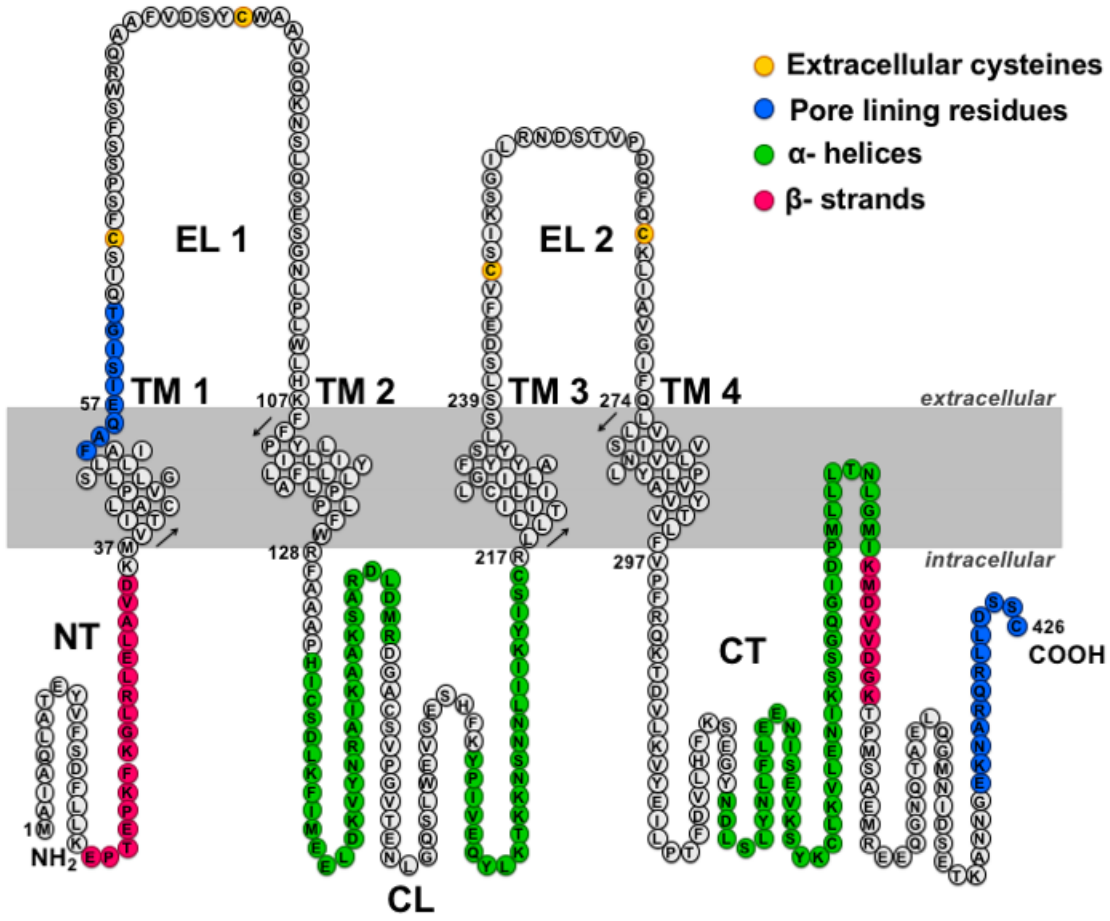

Figure 1.4. Diagram of human pannexin 1 membrane topology showing putative pore lining residues and the secondary structure of cytoplasmic regions. TM1-TM4, transmembrane domains; EL1 and EL2, extracellular loops; CL, cytoplasmic loop; NT, amino terminus; CT, carboxyl terminus. Extracellular cysteine residues (yellow), pore lining residues (blue) identified from SCAM analysis[40] and α-helical regions (green) and β-strands (magenta) suggested by CD spectroscopy [39] are indicated.

Oligomerization. Dodecameric connexin GJCs are formed by the docking of two hexameric HCs, which is confirmed by multiple cryoEM and X-ray structures[43-45]. By analogy to Cxs, it was assumed that Panxs were also hexameric channels because they share the same membrane topology and form similar large-pore membrane channels[13,19,24,30,32]. The stoichiometry of Panxs has been studied by EM and chemical cross-linking experiments. Negative-stain EM of Panxs in native mammalian cell membrane, or purified Panxs from insect cells showed that Panx1 and Panx2 channels have a similar channel topology to connexin HCs[41] (**Figure 1.5a,b**). Panx1 channels were considered to be hexameric on the basis of chemical cross-linking experiments, in which DSP cross-linked Panx1 protein bands on SDS-PAGE migrated at a size expected for hexamers[30] (**Figure 1.5c**). Interestingly, similar cross-linking experiments on Panx2 suggested that they may form heptamers or octamers instead of hexamers[41] (**Figure 1.5d,e**). Although these higher order oligomers have not been reported for Cxs, recent cryoEM structures of INX-6 showed that two octameric INX-6 HCs form a hexadecameric GJC[46,47]. Recent studies by total internal reflection fluorescence (TIRF) microscopy and single-molecule photobleaching analysis of dimeric or trimeric Panx1 concatemers suggested that Panx1 forms a hexameric channel[48]. In summary, on the basis of chemical cross-linking and low-resolution EM, a general conclusion was advanced that Panx1 form a hexameric channel, since there is no compelling high-resolution structural data suggested this conclusion.

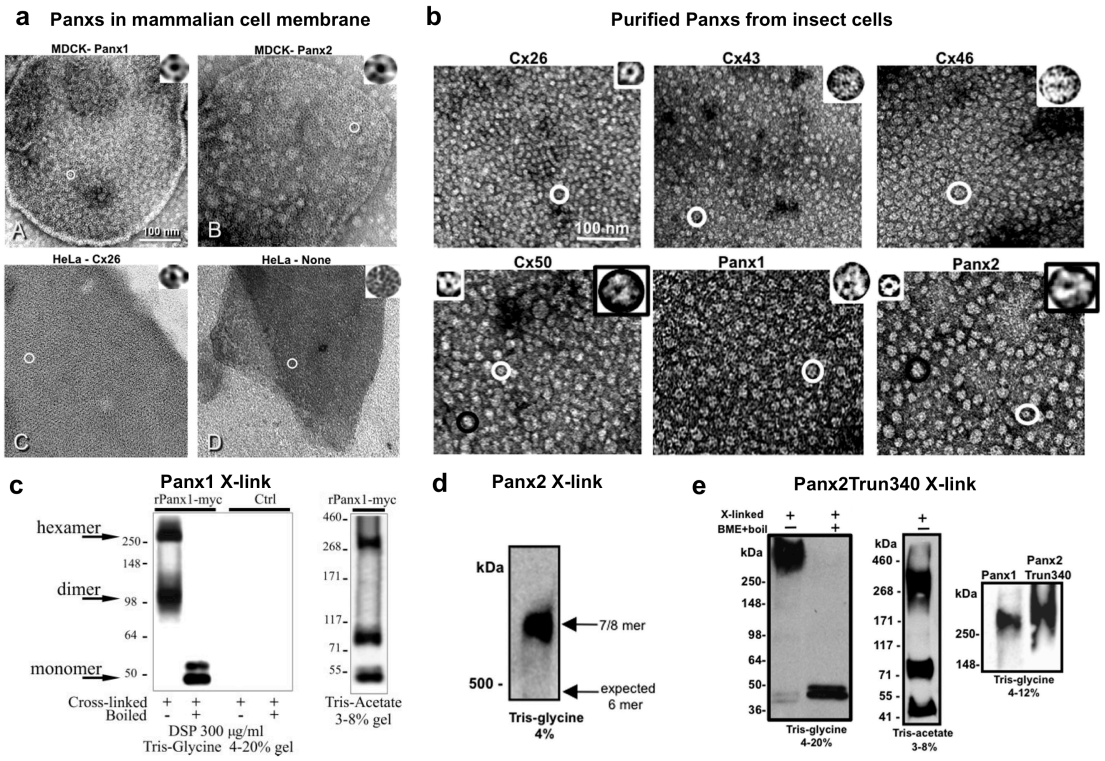

Figure 1.5. Stoichiometric analysis of pannexins by electron microscopy and chemical cross-linking. (a) Panx1 and Panx2 show a channel topology in mammalian cell membrane, very similar to gap junction proteins. Membranes isolated from Panx1 and Panx2 exogenously overexpressed in MDCK cells contain channel-like structures similar in appearance to Cx26 exogenously expressed in HeLa cells. As a negative control, a membrane isolated from parental HeLa cells shows no channel-like structures. **(b)** Isolated pannexin oligomers (pannexons) confirm similar features to connexons. Pannexons and connexons expressed and purified from baculovirus infected Sf9 cells. EM analysis going from a smaller connexin (Cx26 top left image) to Panx2 (bottom right image). The images are displayed at the same magnification to show increasing channel size with increasing monomer size. **(c)** Multimeric nature of Panx1 channels. Left, cross-linking analysis of rPanx1-Myc from mammalian culture cells. HEK-293T parental cells (*Ctrl*) and transiently expressing Myc-tagged recombinant rat Pannexin1 (*rPanx1-Myc*) were solubilized with Triton X-100, chemically cross-linked with 300 µg/ml DSP, separated by SDS-PAGE on a 4–20% gradient gel, and probed with an anti-Myc monoclonal antibody. Boiling of the samples in the presence of 5% β-mercaptoethanol reversed the cross-linking as only the monomers at ~50 kDa are observed. Right, the cross-linked sample was run on a 3-8% Tris acetate gel to better resolve the higher band, using HiMark Pre-stained HMV Protein Standard as reference. **(d)** Cross-linking of a Panx2 for stoichiometric analysis. Cross-linked Panx2 run on a 4% Tris-glycine gel reveals a band located well above a hexamer. This band corresponds to either a heptamer or octamer. **(e)** Cross-linking of a Panx2 truncation mutant for stoichiometric analysis reveal nonhexameric assemblies. To distinguish between an octamer and heptamer stoichiometry, a truncation mutant of Panx2 was constructed so that Panx2 is truncated after Ser340 plus a 30-amino acid tag (370 amino acids total). Left, Panx2 shows the upper band mapping above 250 kDa, suggesting that it is not a hexamer (41 kDa X 6 = 246 kDa) (left lane); cross-linked Panx2 was boiled in the presence of 5% β-

mercaptoethanol and shows the monomeric band mapping as expected ~41 kDa (right lane). Middle, cross-linked Panx2Trun340-V5-His_6 is run on a higher resolving Tris-acetate gel system and is separated into the monomer (41 kDa), the dimer (82 kDa), and the upper band mapping between 268 and 460 kDa. Right, the cross-linked Panx2Trun340-V5-His_6 upper band maps higher than Panx1 hexameric band (~300 kDa). The measured position of the Panx2Trun340-V5-His_6 band is at a position that confirms that the Panx2 oligomer is mostly likely an octamer. (Figure c and corresponding legend modified from Boassa *et al*., 2007. Reprinted from The American Society for Biochemistry and Molecular Biology, Inc. Figure a, b, d, e and corresponding legends modified from Ambrosi *et al*., 2010. Reprinted from The American Society for Biochemistry and Molecular Biology, Inc)[30,41]

1.1.4 Pannexin 1: channel properties

Ionic selectivity. Panx1 forms a non-selective channel in the plasma membrane that allows permeation of ions and molecules up to 1 kDa. Panx1 channels allow efflux of signaling nucleotides such as ATP and UTP[49,50] and small molecules such as glutamate, aspartate, arachidonic acid and its metabolites[51-54], and influx of fluorescent DNA binding dyes such as cationic Yo-Pro and To-Pro dyes, and anionic fluorescein and Lucifer Yellow dyes across the plasma membrane[24,28,49,50,54,55].

Unitary conductance. The unitary conductance is a characteristic single channel property of an ion channel. Panx1 was considered to be a large-conductance (300-500 pS) ion channel for years[49]. Early recordings from human Panx1 channels expressed in *Xenopus* oocytes revealed a large unitary conductance of ~500 pS upon high K^+ activation, with multiple sub-conductance states[49]. A similar large unitary conductance of Panx1 channels was also observed in other cell types such as human erythrocytes upon high K^+ or

hypertonic activation (~450 pS)[24], rat hippocampal neurons upon ischemia-induced activation (~530 pS)[56] and rat atrial cardiac myocytes upon caffeine-induced activation (~300 pS)[57].

Although the evidence cited above supported a large unitary conductance as a property of Panx1 channels, recent studies revealed that Panx1 channels have a much smaller unitary conductance (<100 pS). Recordings from mouse Panx1 expressed in HEK293 cells, without additional physiological stimuli, displayed a smaller single channel conductance of ~70 pS, in which these channels were reported as anion-selective and ATP-impermeable[51,52]. The discrepancies in single channel conductance are probably due to differing channel properties in different cell types. A recent study proposed a model in which Panx1 forms two open channel conformations under different activation states: (1) a large-conductance, non-selective, ATP-permeable conformation induced by various physiological stimuli (e.g. mechanical stress, extracellular potassium or intracellular calcium) and (2) a small-conductance, anion-selective, ATP-impermeable conformation exclusively induced by membrane depolarization[58]. However, Chiu *et al*. showed that small-conductance (~90 pS) Panx1 channels are also capable of releasing ATP or permeating large dyes (To-Pro dyes)[48]. The reasons for these discrepancies in single channel conductance under different activation mechanisms are still unclear, and the nature of the unitary conductance of Panx1 channel needs to be further investigated.

1.1.5 Pannexin 1: channel regulation

Channel activation. Panx1 channels can be activated by various stimuli including mechanical stretch induced by hypotonic stress[24,25,49,59], membrane depolarization[19,49,60], increased extracellular potassium (≥10 mM)[58,61-65] and increased intracellular calcium[34,66] (**Figure 1.6**). Panx1 channels are also activated by receptor-mediated signaling pathways, including G protein-coupled receptors (GPCRs) such as ATP binding to P2Y purinergic receptors (P2Y1 and P2Y2)[34], thrombin binding to protease-activated receptors (PARs)[66,67] and phenylephrine binding to α1 adrenergic (α1D) receptors[66,68-70] via increase of intracellular calcium, as well as ionotropic receptors such as ATP binding to P2X7 purinergic receptors[55,71] and glutamate binding to N-methyl-D-aspartate (NMDA) receptors in neurons[72-74] via Src family kinase (SFK), and other receptors such as insulin binding to insulin receptors in adipocyte[75] and chemokine binding to CXCR4 receptors in T lymphocytes[76] (**Figure 1.6**). A unique activation mechanism is caspase cleavage of the distal C-terminus[50,77-79], which is irreversible in contrast to the reversible activation mechanisms as mentioned above (**Figure 1.6**).

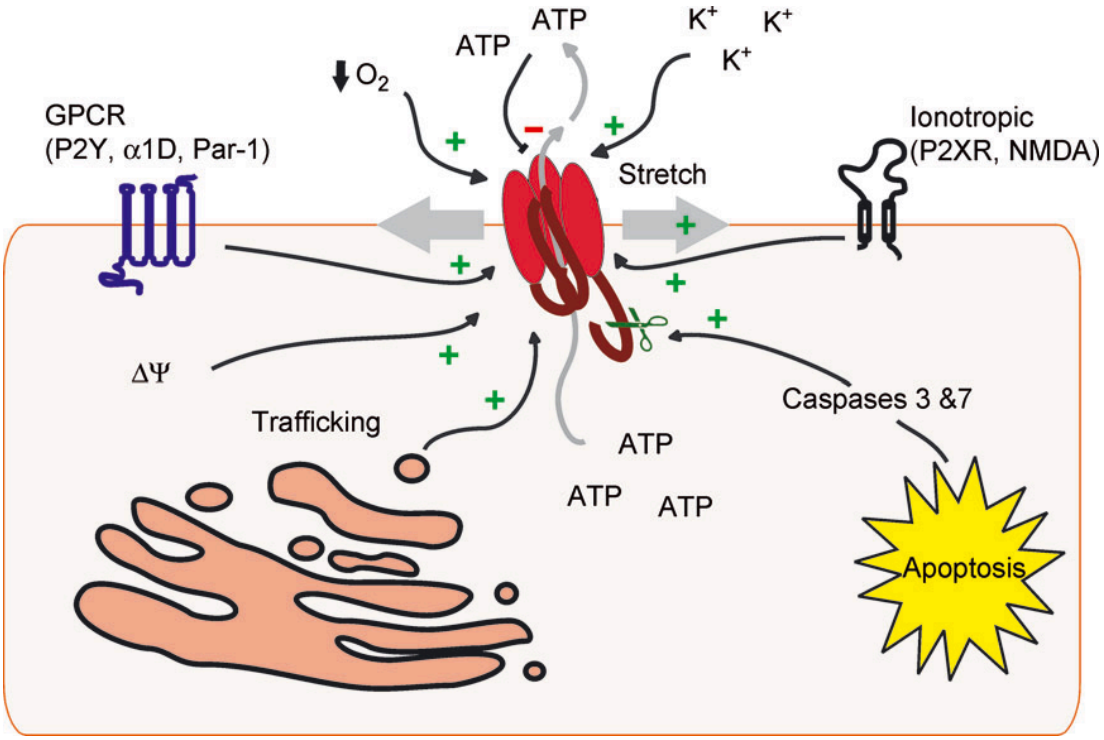

Figure 1.6. Mechanisms of pannexin1 channel modulation. Schematic outlining direct mechanisms of Panx1 channel modulation including activation via plasma membrane stretch/strain, membrane depolarization, extracellular potassium, low oxygen tension, G protein-coupled receptor, caspase cleavage and ionotropic receptors including P2X. (Figure and legend modified from Sandilos and Bayliss, 2012. Reprinted from The Physiological Society: The Journal of Physiology)[80]

Caspase cleavage-mediated activation via a 'ball and chain' mechanism. The definition of 'ball and chain' model is that a channel is blocked by the interaction between an intracellular particle ('ball'), which is tethered to a flexible element ('chain'), and a receptor associated with the pore. The 'ball and chain' model for inactivation of membrane channels was historically described in voltage-gated sodium[81] and *Shaker* potassium channels[82]. Thereafter, several experiments showed that the C-terminus (CT) of connexin may serve as a gating particle via 'ball and chain' mechanism to inactivate GJCs[83-87].

The CT of Panxs is mostly variable in length and sequence, and may play an important role in channel regulation[37]. Several biochemical and physiological studies revealed that caspase cleavage of the CT activates Panx1 channels. As noted previously, SCAM analysis suggested that the distal end of the CT lines the inner part of the channel pore[40]. In addition, a caspase cleavage site ($_{376}$DVVD$_{379}$) in the CT of human Panx1 was also identified (**Figure 1.7**), in which Panx1 channels are activated by caspase cleavage of the CT at this site, resulting in release of nucleotides such as ATP and UTP serving as 'find-me' signals that attract phagocytes for clearance of the dying cells during apoptosis of T lymphocytes[50]. This mechanism was then confirmed in a mouse model[77]. By the use of purified and activated caspase-3, Sandilos *et al*. further confirmed that the caspase cleavage-mediated activation could occur independent of apoptosis. They also showed that purified Panx1 C-terminal tails can inhibit caspase cleavage induced channel activity, and its removal from the channel pore is essential for channel activation[78]. More recently, caspase cleavage-mediated activation of Panx1 at the same C-terminal cleavage site by caspase-11 was observed during lipopolysaccharide-induced pyroptosis[79]. Given these observations, the proposed hypothesis is that the CT functions as a pore-blocking plug to maintain Panx1 channel in an inactive state in a classical 'ball and chain' fashion, and caspase cleavage allows the CT to dissociate from the pore and activate the channel (**Figure 1.8**). Notably, unlike other activation mechanisms that are reversible, caspase cleavage-mediated activation is irreversible.

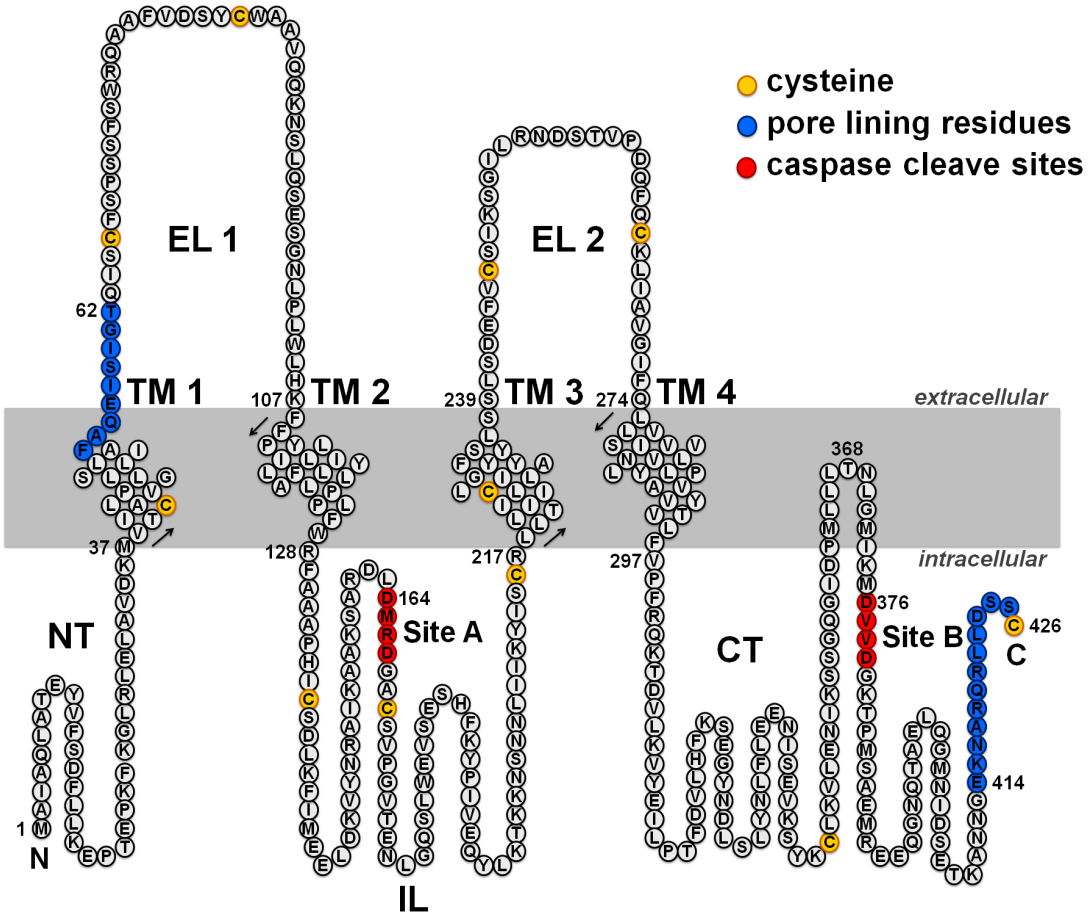

Figure 1.7. Diagram of human Panx1 membrane topology showing putative pore lining residues and the caspase cleavage sites. TM1-TM4: transmembrane domains; EL1 and EL2: extracellular loops; IL: intracellular loop; NT: amino terminus; CT: carboxyl terminus. Cysteine residues (yellow), pore lining residues (blue) identified from SCAM analysis[40] and caspase cleavage sites[50] (red) are indicated.

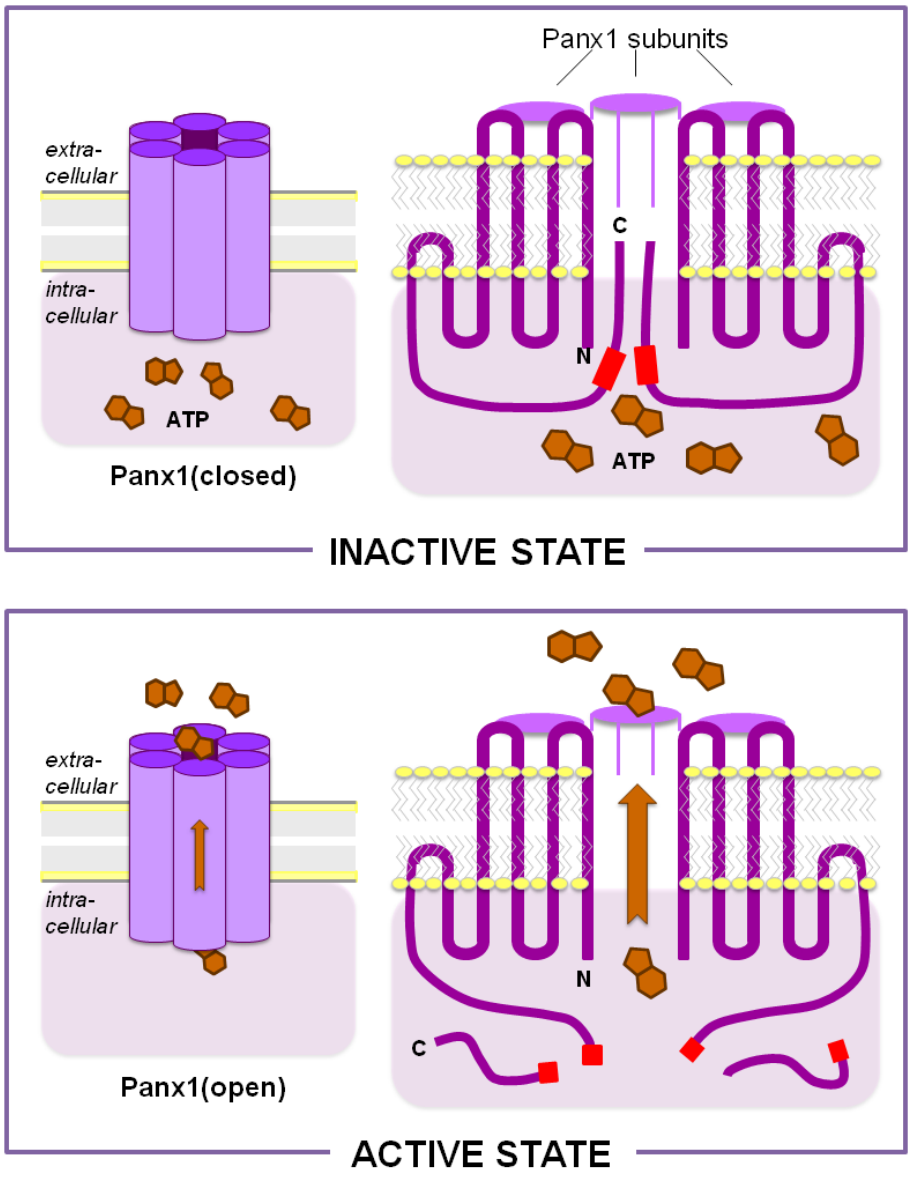

Figure 1.8. Caspase cleavage-mediated activation of Panx1 channels. Left, hexameric representation of Panx1 channels for ATP release upon activation. Right, it is hypothesized that the CT functions as a plug that inactivates the channel by blocking the pore (*upper*). Caspase cleavage activates the channel by releasing the CT, thereby allowing nucleotides such as ATP to be released into the extracellular space (*lower*). (Figure adapted from Billaud *et al*., 2012)[88]

Channel inhibition. Activated Panx1 channels can be inhibited by various factors such as CO_2-mediated cytoplasmic acidification[34] or extracellular acidification[89], negative feedback of ATP release[90], increased intracellular redox potential[42,91,92], S-nitrosylation[93] and arachidonic acid[94].

Panx1 channel activity can also be inhibited by diverse pharmacological blockers, including mimetic peptide against Panx1 EL1 (^{10}Panx1)[95], gap junction blockers such as carboxenone (CBX) and fluefenamic acid (FFA)[33], the transport blocker probenecid[96], chloride channel blocker DIDS[60], anti-malaria drug mefloquine[97], anti-diabetic drug glibenclamide (glyburide)[62], the food additive Brilliant Blue FCF (BB FCF)[98] and the quinolone antibiotic trovafloxacin[99].

1.1.6 Pannexin 1: post-translational modifications

Glycosylation. N-linked glycosylation is the covalent addition of sugar moieties at an asparagine residue. N-linked glycosylation of Panx1 at residue Asn254 (in EL2) (**Figure 1.2, 1.9**) yields three species, a core non-glycosylated protein (Gly0) predominately in the endoplasmic reticulum (ER), a high mannose-glycosylated protein (Gly1) predominately in the early Golgi apparatus, and a complex, mature glycosylated protein (Gly2) predominantly at the cell surface. N-linked glycosylation plays a role in regulating Panx1 trafficking to the plasma membrane, which may affect Panx1 function in different tissues[30-32,36]. N-linked glycosylation may also increase cell surface stability of mature glycosylated

Panx1[100]. Lastly, N-linked glycosylation may sterically prevent formation of Panx1 GJCs[23].

Phosphorylation. Protein phosphorylation is a reversible process where serine, threonine, or tyrosine residues are phosphorylated by kinases for regulating signaling networks. Multiple phosphorylation sites of Panx1 have been predicted on the basis of the amino acid sequences and putative recognition sites for protein kinases[101](**Figure 1.9**). In J774 cells, the Src family kinase (SFK) activates Panx1 channel by ionotropic P2X7 receptors; however, no specific phosphorylation sites were detected in this study[71]. More recently, two SFK-dependent phosphorylation sites of Panx1 were identified (**Figure 1.9**). The first site is Tyr308, in which the NMDA receptors activated Panx1 channels via SFK in rodent hippocampal brain slices[73,74]. The second site is Tyr198, in which TNF-α induced SFK-dependent phosphorylation and activation of Panx1 channels in human venous endothelial cells[102]. These studies showed that SFK-dependent phosphorylation of Panx1 is a crucial regulator in receptor-mediated activation. In addition to SFKs, other kinases such as c-Jun NH(2)-terminal kinase (JNK)[103] and protein kinase G (PKG)[104] may also be involved in regulating Panx1 channel activity.

S-nitrosylation. S-nitrosylation is the covalent addition of nitric oxide (NO) to an exposed cysteine residue. Two cysteine residues in Panx1, Cys40 in the N-terminal pore-lining region and Cys346 in the CT have been considered to be the

S-nitrosylation sites[42,92] (**Figure 1.9**). S-nitrosylation of Panx1 at these two sites closes the channel[93].

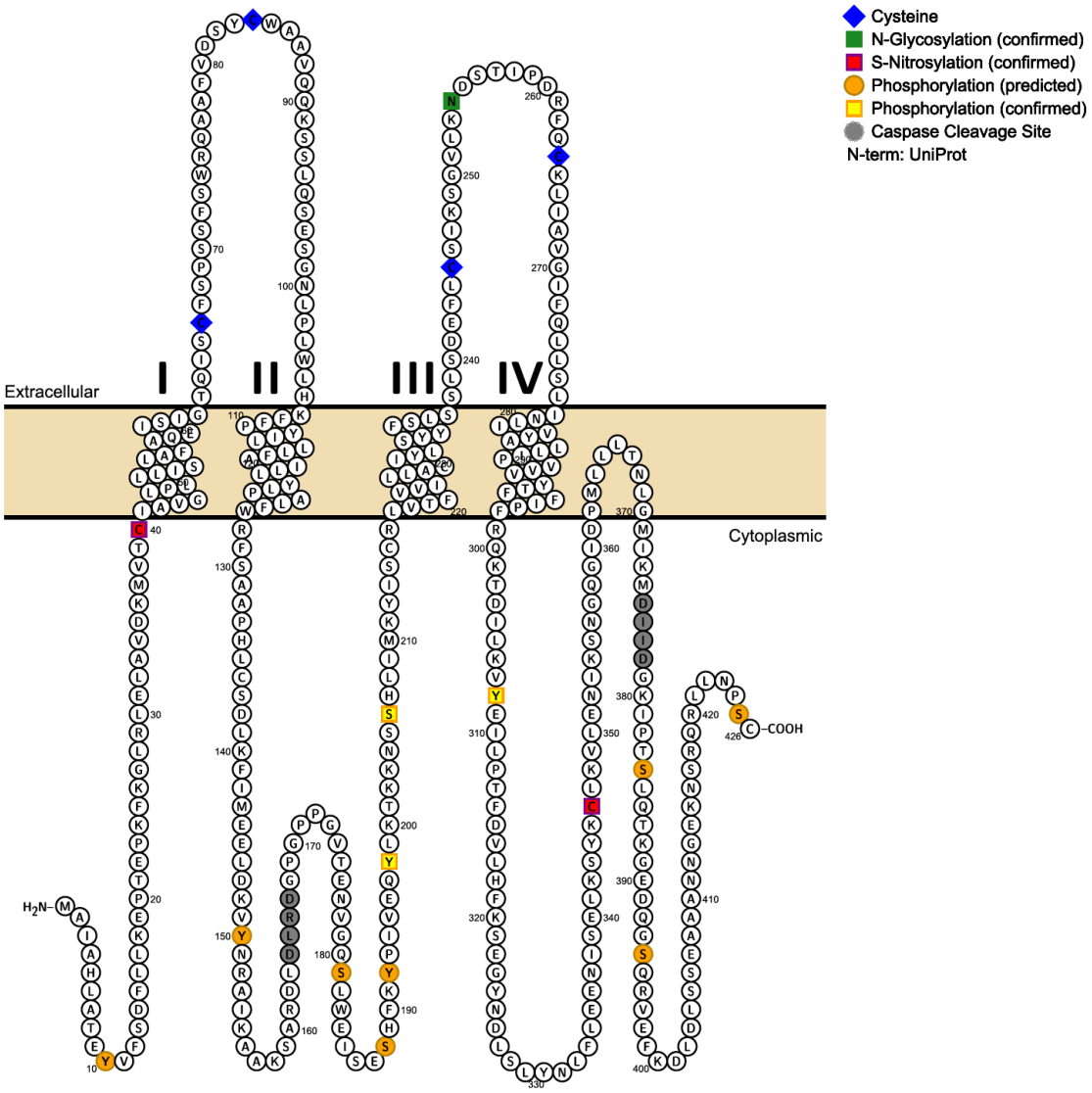

Figure 1.9. Diagram of mouse Pannexin 1 membrane topology and post-translational modifications. Based on sequence analysis using the UniProt database, Pannexin 1 is predicted to contain four transmembrane regions. It contains four conserved extracellular cysteine residues (blue) in the extracellular loops and a confirmed N-glycosylation site (green) necessary for plasma membrane translocation. Multiple post-translational modification sites by S-nitrosylation (pink), phosphorylation (yellow), or proteolytic caspase cleavage (gray) have been confirmed to regulate channel gating. Additional post-translational modifications were predicted and annotated using PhosphoSitePlus (orange) (Figure and legend from Begandt *et al.*, 2017. Reprinted from BMC Cell Biol)[101]

1.1.7 Pannexin 1: role as an ATP release channel in disease

Panx1 as an ATP release channel. The nucleotide adenosine triphosphate (ATP) is classically considered as an intracellular energy molecule for multiple cell functions. ATP also plays a novel role as an extracellular signaling molecule, in which release of ATP from different cell types regulates cell functions. There are two primary mechanisms for ATP release: (1) vesicular-mediated ATP release via exocytosis and (2) channel-mediated ATP release such as connexin hemichannels, purinergic receptors, calcium homeostasis modulator 1 (CALHM1) and volume-regulated anion channels (VRACs)[21,105,106].

Panx1 was initially characterized as an ATP release channel in *Xenopus* oocytes exogenously expressing human Panx1[49]. Subsequently, Panx1 expression was detected in a variety of different cell types that release ATP, including erythrocytes[24,107], neurons and astrocytes in the CNS[61,72,108-110], taste bud cells[111,112], T lymphocyte cells[113-115], airway epithelial cells[25,59], endothelial cells[67] and skeletal and smooth muscle cells[68,69,88]. Particularly, in polarized airway epithelial cells, there was a correlation of Panx1 expression with ATP release sites[25]. ATP release through Panx1 channels is also correlated with an uptake of either negatively or positively charged fluorescent dyes[24,55,96]. As noted previously, Panx1 channels can be activated by ATP binding to P2Y purinergic receptors[34], and inactivated by negative feedback of ATP release[90], which is critical for protecting cells from excessive activation. Furthermore,

pharmacological blockers such as probenecid inhibits both Panx1 channels and ATP release[96].

ATP release by Panx1 channel plays a crucial role in various physiological processes such as taste sensation, airway defense, blood pressure regulation and apoptotic cell clearance, as well as a broad range of pathological processes such as inflammation, neurological disorders, cardiovascular diseases and cancer.

Taste sensation. Panx1 channels were originally considered as the ATP-release channel in taste bud receptor (type II) cells, in which the release of ATP through Panx1 channels subsequently stimulates the presynaptic cells to release serotonin (5-HT) for sensing taste[111,112]. However, later experiments using Panx1 knock out mice showed that type II cells have normal ATP release and taste sensation[52,116,117]. Instead, CALHM1, a voltage-gated ATP-release channel, is necessary for sweet, bitter and umami taste perception[118].

Airway defense. Panx1 channels in airway epithelial cells release ATP under hypotonic stress, regulating ciliary beat frequency and surface liquid volume for mucociliary clearance of pathogens and foreign particles in airway defense[25].

Blood pressure regulation. Panx1 channels are involved in both vasodilation and vasoconstriction. Upon stress activation, Panx1 channels in erythrocytes release ATP, which binds to PY2 receptors in endothelial cells to initiate Ca^{2+} wave propagation, resulting in NO release from endothelial cells to relax smooth muscle cells[24]. In addition to vasodilation, Panx1 channels are also associated with vasoconstriction by phenylephrine-induced activation of α1 adrenergic (α1D) receptor in vesicular smooth muscle cells[68,69].

Apoptotic cell clearance. As noted previously, Panx1 mediates release of nucleotides such as ATP and UTP, which serve as 'find-me' signals to recruit phagocytes for the clearance of dying cells during apoptosis of T lymphocytes[50,119].

Inflammation. Panx1 channels are involved in innate immune response such as inflammasome activation, as well as adaptive immunity such as HIV infection. In macrophages, Panx1 associated with the P2X7 receptor signaling cascade, mediates formation of the inflammasome, a large multiprotein complex that can activate caspase-1 for subsequent release of the pro-inflammatory cytokine interleukin (IL)-1β[55]. Panx1 also forms the Toll-like receptor-independent inflammasome with cryopyrin, in recognition of bacterial molecules passing from endosomes to the cytoplasm[120]. Related to HIV infection, interaction of the HIV-1 envelope trimer with CD4 receptors and co-receptors (CXCR4 and/or CCR5) triggers Panx1 channel opening and ATP release, which subsequently activates

purinergic receptors, thereby facilitating plasma membrane depolarization and viral envelope fusion[121,122].

Neurological disorders. Panx1 plays a role in several neurological disorders such as ischemic stroke, epileptic seizure, Crohn's disease and migraine headache. Obstruction of a cerebral artery by an embolus restricts cerebral blood flow, which impairs the delivery of glucose and oxygen for proper cerebral function and consequently results in an ischemic stroke[123-125]. Panx1 channel is involved in ischemia-induced neuronal death during stroke, in which oxygen and glucose deprivation (OGD) triggers opening of Panx1 channels, resulting in large currents that in turn cause ionic dysregulation, leading to neuronal death[56,72]. Following the discovery of Panx1 activation in epileptiform activity[72], it was proposed that Panx1 plays a critical role in the severity and duration of epileptic seizures. Panx1 is activated by high levels of extracellular potassium generated from epileptiform seizure-like activity, resulting in release of ATP that subsequently activates purinergic receptors to further increase neuronal hyperactivity[63]. Crohn's disease is an inflammatory bowel disease (IBD) and caused by inflammation induced neuron death. It was proposed that Panx1 channels are required for P2X7 receptor mediated enteric neuron cell death in intestinal inflammation in Crohn's disease[126]. Panx1 channels are also activated by neurons stressed during cortical spreading depression, associated with the cause of migraine headaches[127].

Cardiovascular diseases. Panx1 associated with the P2X7 receptor mediates the release of multiple cardioprotectants in response to both ischemic pre- and post-conditioning in rat hearts[128,129]. In contrast to release of cardioprotectants, Panx1 is also implicated in cardiac fibrosis, which impairs cardiac function and can result in heart failure[130].

Cancer. It was initially proposed that Panx1 was tumor suppressive in gliomagenesis, in which exogenous expression of Panx1 in C6 gliomas results in reduced proliferation, motility and anchorage-independent growth[20]. In contrast, Panx1 may play a role in cancer aggressiveness and metastasis by stimulating tumorigenesis and metastasis in melanoma[131] and breast cancer[132].

A better understanding of the structure and function of Panx1 channels will provide insight into these physiological and pathological processes, and hopefully provide clues for novel therapeutic approaches for relevant diseases. For example, the Panx1 inhibitor probenecid has been used for decades as a treatment for gouty arthritis. It was recently shown that probenecid may protect against ischemic brain injury by inhibiting neuronal death and reducing inflammation in the brain[133]. The very recently found inhibition of Panx1 by quinolone antibiotic trovafloxacin may explain the side effects of the widely used quinolone antibiotics for the treatment of bacterial infections, and to develop safer and more potent antibacterials[99].

1.2 Structural studies of other tetra-spanning membrane channels

1.2.1 General introduction

As noted previously, Panxs share a common tetra-spanning membrane topology with Cxs and Inxs. Other membrane channels consisting of similar membrane topology include leucine-rich repeat-containing 8 (LRRC8) protein channels, which are volume-regulated anion channels (VRACs) that allow permeation of anions in response to osmotic swelling[134-136], and calcium homeostasis modulator 1 (CALHM1) ion channels, which are gated by voltage and extracellular Ca^{2+} and permeable to large cations and anions including Ca^{2+} and ATP[137,138]. Structural studies on Cx GJCs date to the 1950s; however, high-resolution structures became available in the last decade for only one Cx member, Cx26[44,45]. The high-resolution structures of Inx-6 and LRRC8A were just recently determined by electron cryomicroscopy (cryoEM) and single particle image analysis[47,139]. The structure of CALHM1 has yet to be determined.

1.2.2 Connexin gap junction channel

As described in Chapter 1.1, connexins (Cxs), the vertebrate gap junction channels (GJCs), are formed by end-to-end docking of two hexameric hemichannels (HCs) from adjacent cells, which mediate intercellular communication by transporting molecules such as Ca^{2+}, $InsP_3$, cAMP and ATP, playing important roles in maintaining tissue homeostasis[1,2]. There are 21 human

Cx isoforms, which differ primarily in their molecular weight and tissue specificity[140]. Cxs are involved in diverse human diseases such as deafness, skin disorders, cardiovascular diseases, lens cataracts, oculodental dysplasia and peripheral neuropathies (e.g. Charcot-Marie-Tooth disease)[141-148].

Historically, structures of gap junctions were studied using electron crystallography of two-dimensional (2D) arrays of channels generated from native tissues or recombinant systems[43,149-152]. The first three-dimensional (3D) reconstruction of Cx GJCs was obtained from negative-stain electron microscopy (EM)[149] and cryoEM[150] of rat liver gap junctions, which showed hexameric architecture of the HCs at 19 Å resolution (**Figure 1.10a,b**). The resolution was primarily limited by disorder in the 2D crystals. The first breakthrough in resolution was from the 3D electron crystallographic structure of a CT-truncated Cx43 GJC expressed in mammalian cells at 7.5 Å in-plane resolution, validating the models of hexameric HCs and dodecameric GJCs and revealing the close packing of 24 transmembrane (TM) helices in each HC[43] (**Figure 1.10c**). Nonetheless, this cryoEM map at subnanometer resolution did not allow accurate assignment of TM helices due to lack of amino acid side chain information. A decade later, a high-resolution structure of Cx26 GJC was determined by X-ray crystallography at 3.5 Å resolution, which clarified the assignment of TM helices, the arrangements between adjacent subunits, the docking interactions between two HCs and the channel pore architecture[44] (**Figure 1.10d**). Additional X-ray crystal structures of Cx26 with and without bound Ca^{2+} were recently determined,

which reveal the Ca^{2+} binding sites at the TM-extracellular gap interface between adjacent subunits[45]. Although structures of Cx26 are determined at near atomic resolution, the cytoplasmic domains have not been observed and resolved, probably due to their structural disorder[153].

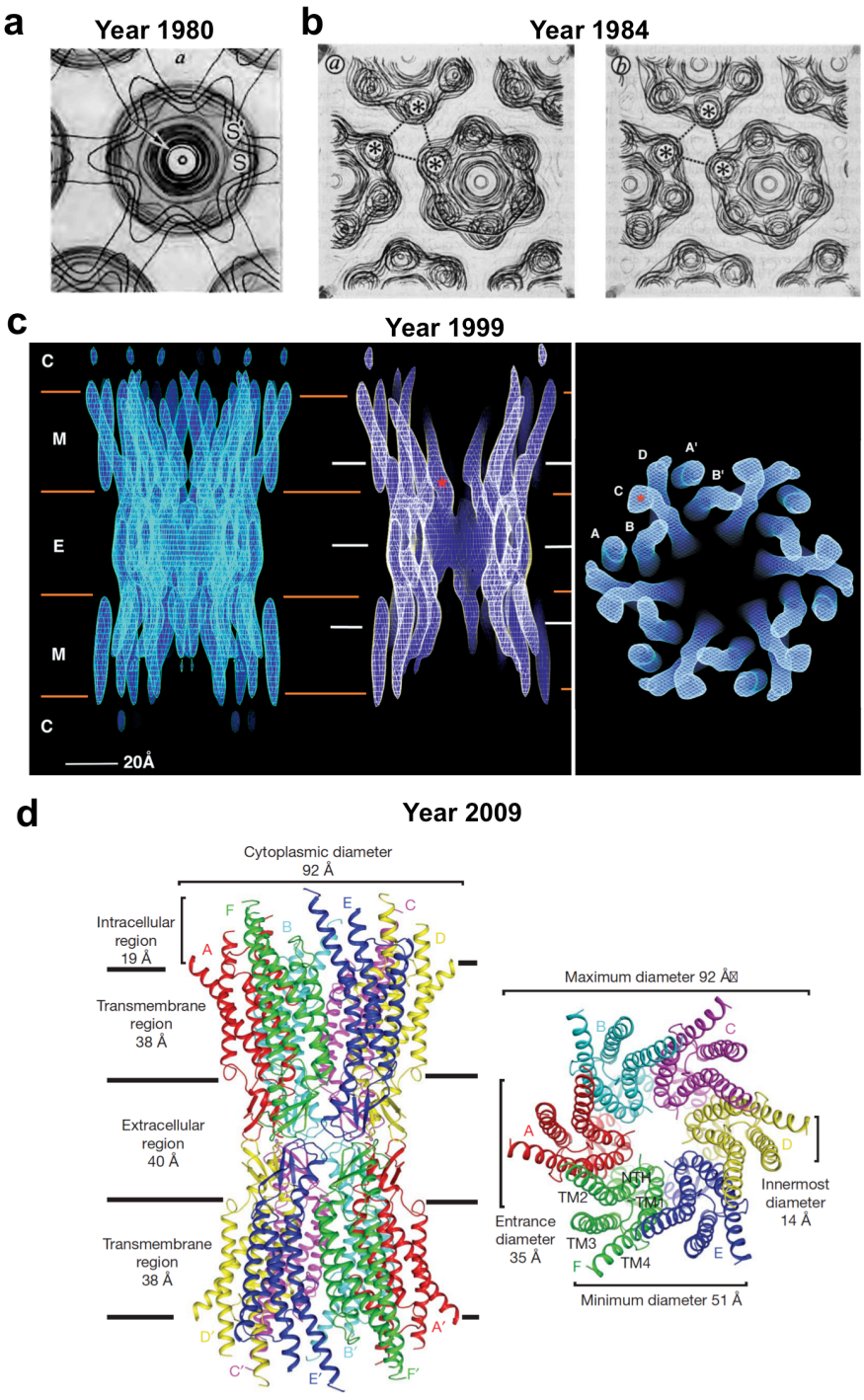

Figure 1.10. Structures of connexin gap junction channels. (a) Map of one half of the gap junction, generated from negatively stained, isolated rat hepatocyte junctions. (Figure and legend modified from Unwin and Zampighi, 1980. Reprinted from Macmillan Publishers Ltd: Nature)[149] **(b)** Map of the gap junction channel without Ca^{2+} (left) and with Ca^{2+} (right) in one of the membrane, generated from frozen, isolated rat liver junctions. (Figure and legend modified from Unwin and Ennis, 1984. Reprinted from Macmillan Publishers Ltd: Nature)[150] **(c)** 3D map of a recombinant gap junction channel at 7.5 Å in the membrane plane and 21 Å in the vertical plane, determined by electron crystallography of C-terminal truncated Cx43 expressed in mammalian cells. (Figure and legend modified from Unger *et al.*, 1999. Reprinted from AAAS)[43]. **(d)** Crystal structure of human Cx26 gap junction channel at 3.5 Å, determined by X-ray crystallography. (Figure and legend modified from Maeda *et al.*, 2009. Reprinted from Macmillan Publishers Ltd: Nature)[44]

1.2.3 Innexin gap junction channel

Innexins (Inxs) form invertebrate GJCs, which share similar membrane topology to Cxs but no sequence homology (**Figure 1.1**, **1.11**). There are 8 Inxs in *Drosophila melanogaster* and 25 Inxs in *Caenorhabditis elegans (C. elegans)*[7,38,154-156]. Inxs are important for synaptic transmission and morphogenesis in *Drosophila*[157,158], and embryonic development and eating function in *C. elegans*[159,160].

Early structural studies of Inx and Cx GJCs revealed small structural differences in gap width, channel size and spacing, and oligomeric number[11]. Specifically, Inx GJCs have a wider gap and larger channel size and spacing in comparison with Cx GJCs (**Figure 1.11**).

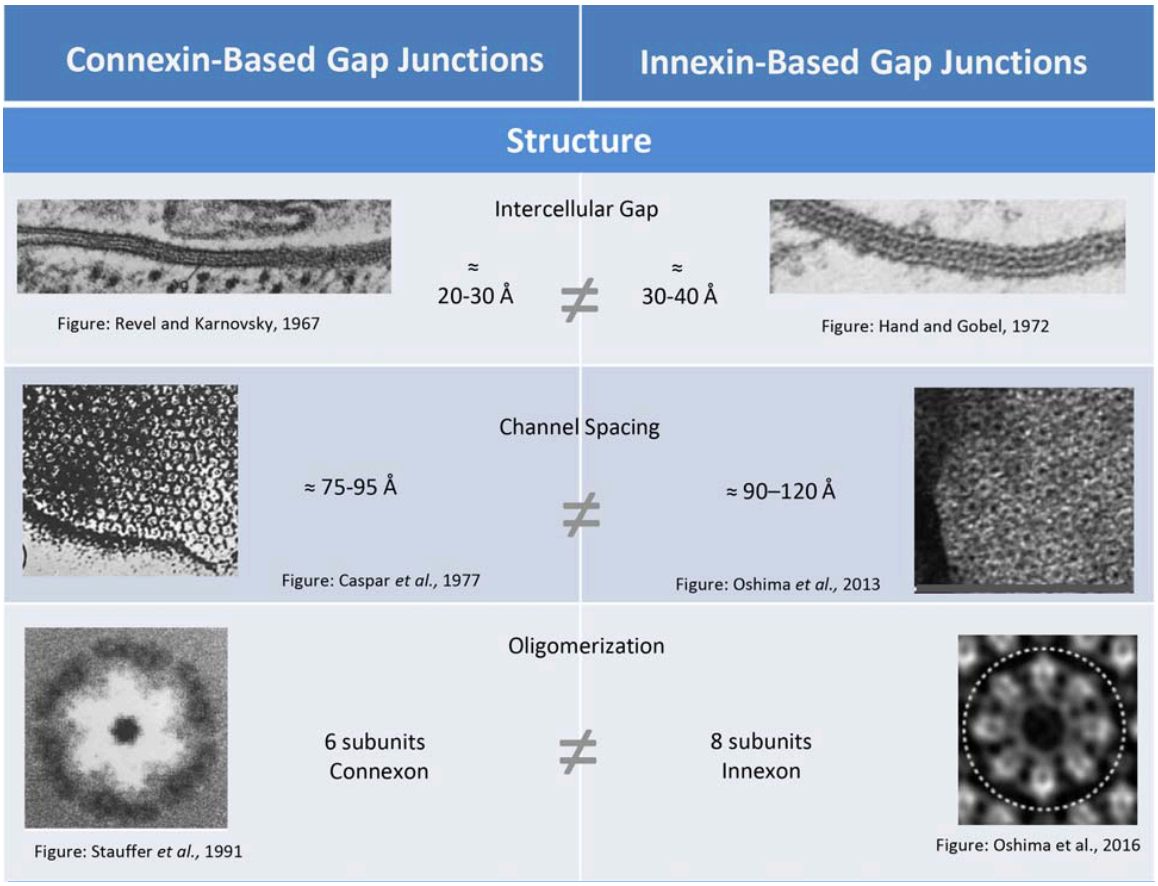

Figure 1.11. Comparison of gap junctions composed of connexins and innexins focusing on structure. Intercellular Gap: The gap between cells is slightly larger in invertebrate preparations. Left, section of mouse heart gap junction treated *en bloc* with lanthanum and stained with uranyl acetate. Intercellular gap ≈ 18 Å. Right, section of a gap junction between muscle cells of Hydra treated *en bloc* with lanthanum and stained with lead citrate. Intercellular gap ≈ 30 Å. Channel Spacing: Channels are spaced farther apart in invertebrate preparations. Left, electron micrograph of an isolated gap junction plaque from mouse liver. Center of connexons are marked. Right, electron micrograph of gap junction plaque from *Sf9* cells expressing *C. elegans* INX-6 negatively stained with uranyl acetate. Oligomerization: Connexin-based channels are hexameric while innexin-based channels are octameric. Left, six-fold rotationally filtered image of a connexon purified from rat liver. Right, projection map of a *C. elegans* INX-6 deletion mutant expressed in *Sf9* cells, solubilized, purified and negatively stained. (Figure and legend modified from Skerrett and Williams, 2017. Reprint from Developmental Neurobiology Published by Wiley Periodicals, Inc)[11]

As noted above, Cx HCs are hexameric and GJCs are dodecameric, which have been confirmed by several Cx structures[43-45]; however, the electron crystallographic structure of *C. elegans*, N-terminally truncated INX-6 (INX-6 ΔN) at 10 Å resolution revealed that two octameric Inx HCs form a hexadecameric GJC[46] (**Figure 1.11, 1.12a**). High-resolution structures of the wild-type INX-6 (INX-6 WT) HC and GJC were recently determined at 3.3 Å and 3.6 Å, respectively, by single-particle cryoEM[47] (**Figure 1.12b**). The oligomeric state of the cryoEM structure is consistent with previous electron crystallographic structures, with eight subunits in each HC.

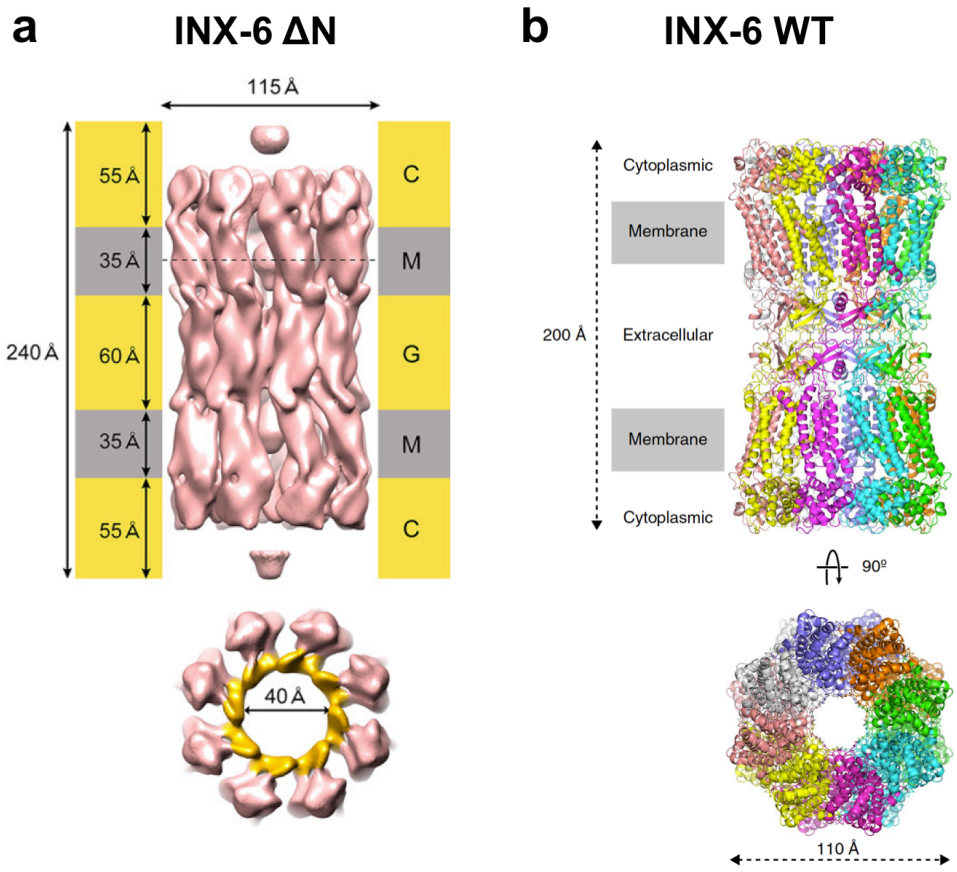

Figure 1.12. Structures of innexin gap junction channels. (a) Structure of a single INX-6ΔN gap junction channel in which a negative temperature factor of B = −500 Å^2 and eight-fold non-crystallographic rotational symmetry are used. Top, surface view structure of an INX-6ΔN gap junction channel (salmon pink) with measured widths

corresponding to transmembrane and hydrophilic regions, and channel diameter. For membrane boundary layer representation, the transmembrane regions are colored in gray and indicated by an “M”, and the extra-membrane domains are in yellow, with extracellular gap regions indicated by a “G” and cytoplasmic domains indicated by a “C″. Bottom, 30 Å-thick slabs of the INX-6ΔN structure viewed perpendicular to the membrane. The pore entrance is restricted by the cytoplasmic crown with a 40 Å diameter. (Figure and legend modified from Oshima *et al.*, 2016. Reprint from Elsevier Ltd: J Mol Biol)[46] **(b)** INX-6 gap junction structure. Ribbon model of INX-6 gap junction channel in side view (top) and top view (bottom). (Figure and legend modified from Oshima *et al.*, 2016. Reprint from Macmillan Publishers Ltd: Nature Communications)[47]

Notably, unlike Cxs with disordered cytoplasmic domains, the cytoplasmic domains of INX-6 are primarily composed of α-helices, which form a continuous roof in an octameric HC and are termed as the ‘cytoplasmic dome’ by the authors[47] (**Figure 1.12b**, **1.13**).

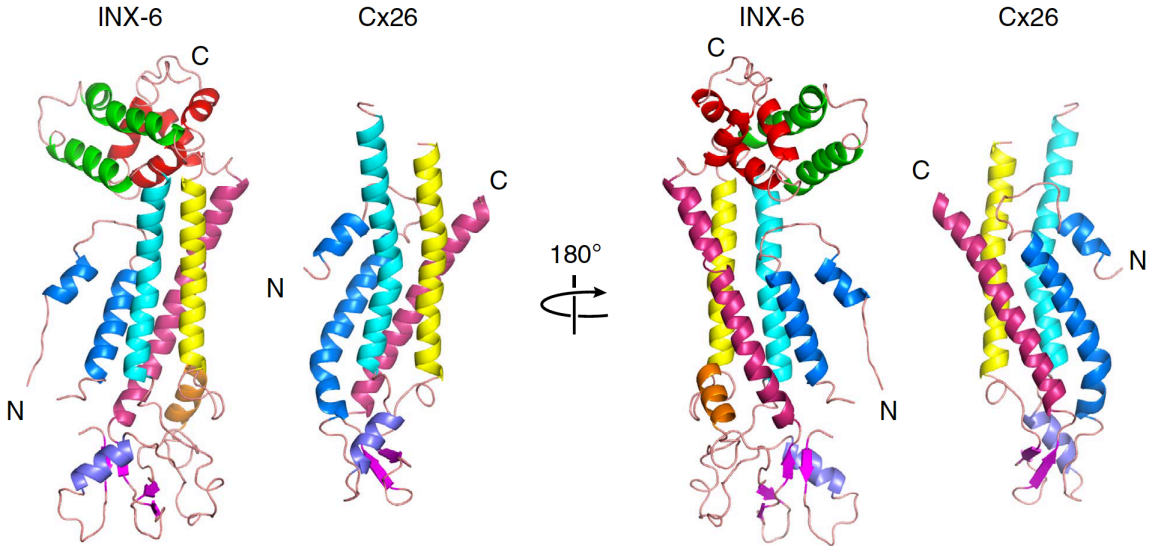

Figure 1.13. Comparison of INX-6 and Cx26 monomers. The monomeric structures of INX-6 and Cx26 (pdb code: 2zw3) are presented side by side. Each transmembrane helix is coloured as follows: TM1 in blue, TM2 in cyan, TM3 in yellow and TM4 in pink. β-sheets are coloured magenta. The N- and C- termini are indicated by ‘N’ and ‘C’, respectively. (Figure and legend modified from Oshima *et al.*, 2016. Reprint from Macmillan Publishers Ltd: Nature Communications)[47]

1.2.4 LRRC8 volume regulated anion channel

The LRRC8 protein family comprises the volume-regulated anion channel (VRAC), which is a ubiquitously expressed mammalian anion channel and regulates cell volume homeostasis in response to osmotic swelling[135,136,161]. In addition to volume regulation, VRACs are also involved in other physiological processes such as apoptosis, cell proliferation and release of excitatory amino acids, and are implicated in various human diseases such as stroke, diabetes and cancer[162-165]. LRRC8A (SWELL1), a member of the LRRC8 family (LRRC8 A-E), has been identified as an essential component of VRACs[135,136]. The LRRC8A monomer is composed of two domains: the N-terminal transmembrane pore domain (PD) and the C-terminal leucine-rich repeat domain (LRRD)[166].

Very recently, the structure of the mouse LRRC8A (SWELL1) was determined by a combination of cryoEM and X-ray crystallography, in which the PD was determined at 3.66 Å resolution by single-particle cryoEM and the LRRD was determined at 1.8 Å resolution by X-ray crystallography[139] (**Figure 1.14**). Like the Cx HC, the LRRC8A membrane channel is also hexameric (**Figure 1.14b**).

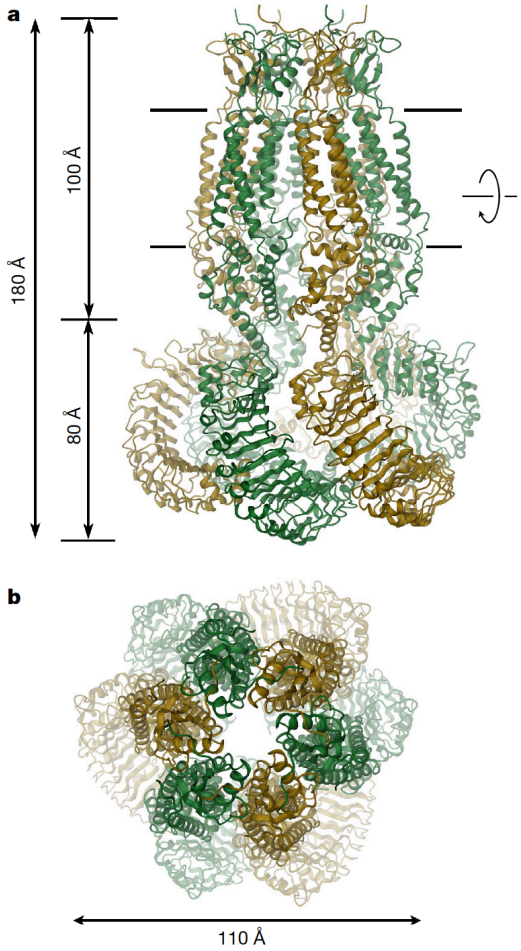

Figure 1.14. The structure of LRRC8A. (a) Ribbon representation of the hexameric LRRC8A structure viewed from within the membrane. Membrane boundaries and molecular dimensions are indicated. (**b)** LRRC8A hexamer viewed from the extracellular side. (Figure and legend modified from Deneka *et al.*, 2018. Reprint from Macmillan Publishers Limited: Nature)[139]

In addition, the folding in LRRC8A (PD) resembles Cx and Inx structures, especially in the TM helices and the extracellular domain[139] (**Figure 1.15a**). The different channel properties with respect to substrate size and ionic selectivity (large-pore, non-selective GJCs versus small anion-selective VRACs) may be explained by the different pore structures (large pore diameter in GJCs versus constricted extracellular region in LRRC8A)[139] (**Figure 1.15b**).

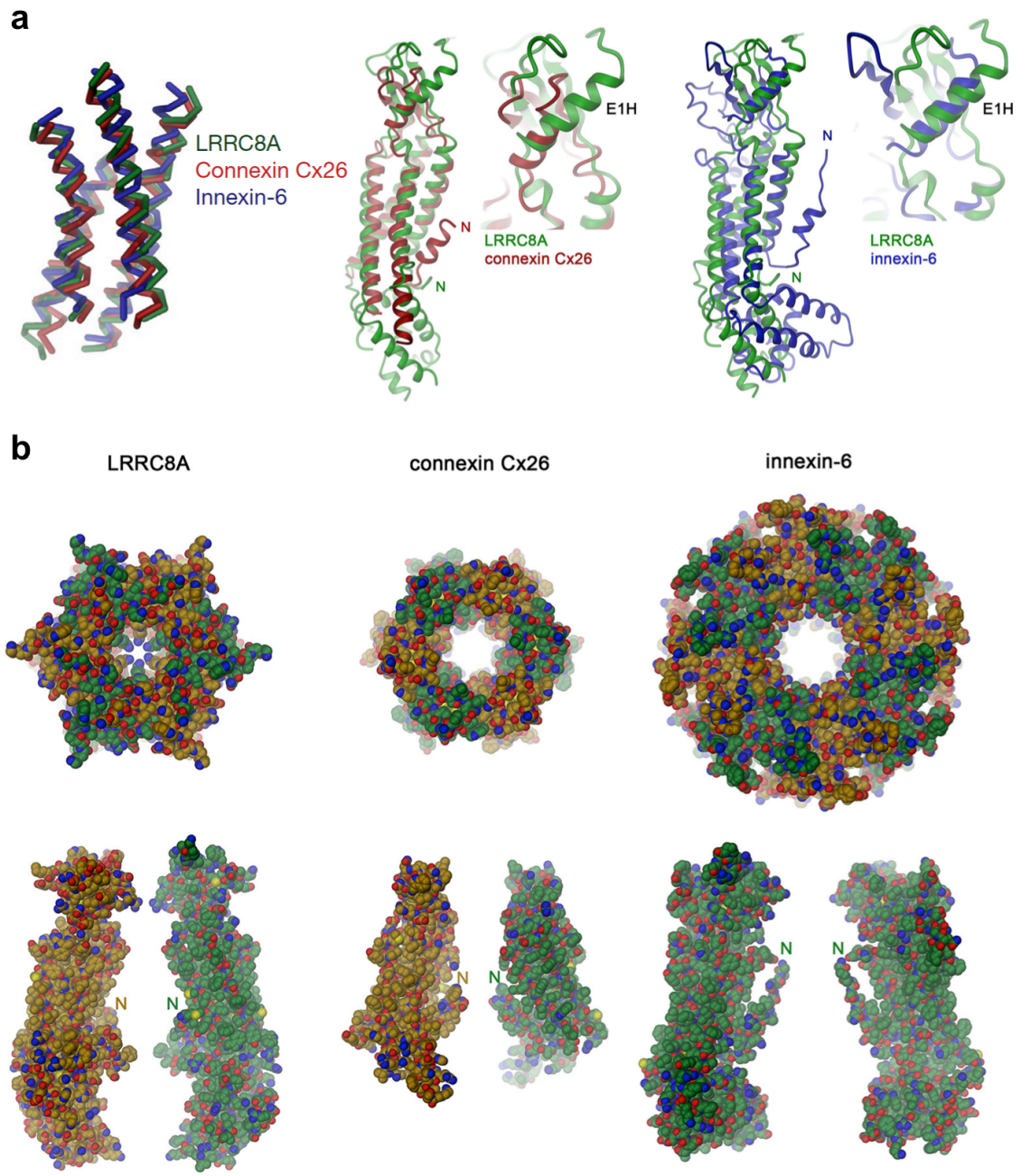

Figure 1.15. Comparison of LRRC8A with gap junction proteins. (a) Left, superposition of the four transmembrane helices (as Cα-representation) of LRRC8A with the equivalent regions of connexin Cx26 (PDB: 2ZW3) and innexin-6 (PDB: 5H1Q). Middle, superposition of subunits of LRRC8A (green) and connexin Cx26 (PDB: 2ZW3, red) and expanded view of the ESD. Right, superposition of subunits of LRRC8A (green) and innexin-6 (PDB: 5H1Q, blue) and expanded view of the ESD. **(b)** Pore domains of LRRC8A with modelled N-terminal residues, connexin Cx26 (PDB: 2ZW3), and innexin-6 (PDB: 5H1Q), viewed from the extracellular side (top), and two opposing subunits of the respective channels shown from within the membrane with N termini indicated (bottom). The proteins are shown as space-filling models. (Figure and legend modified from Deneka *et al.*, 2018. Reprint from Macmillan Publishers Limited: Nature)[139]

1.2.5 Pannexins, innexins, and LRRC8 proteins: sequence and structure

LRRC8 proteins share the same membrane topology with Panxs, in which four transmembrane (TM) helices are connected by two extracellular loops (EL) and one cytoplasmic loop (CL), with cytoplasmic amino (NT) and carboxyl termini (CT). Both Panxs and LRRC8 proteins show four conserved cysteine residues and one N-linked glycosylation site in the ELs, and multiple phosphorylation sites in the cytoplasmic regions (CL and CT)[134] (**Figure 1.16**).

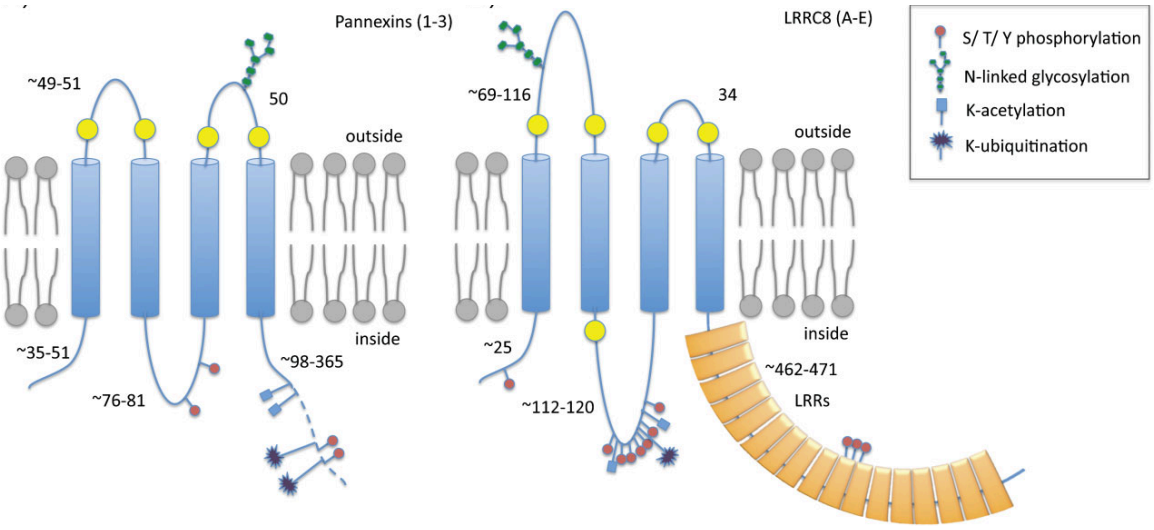

Figure 1.16. Proposed topology and post-translational modifications of pannexins and LRRC8 proteins. Conserved cysteines are indicated with yellow circles. Post-translational modifications (see legend) of the different paralogues are summarized in the picture (not all paralogues are necessarily subjected to the same modifications). The 17 LRRs of LRRC8 proteins are shown as orange boxes. (Figure and legend modified from Abascal and Zardoya, 2012. Reprint from WILEY Periodicals, Inc: Bioessays)[134]

Intriguingly, in addition to similar membrane topology, LRRC8 proteins share a common ancestor with Panxs at the origin of chordates. Panxs are more evolutionarily related to LRRC8 proteins than Inxs[134] (**Figure 1.17**).

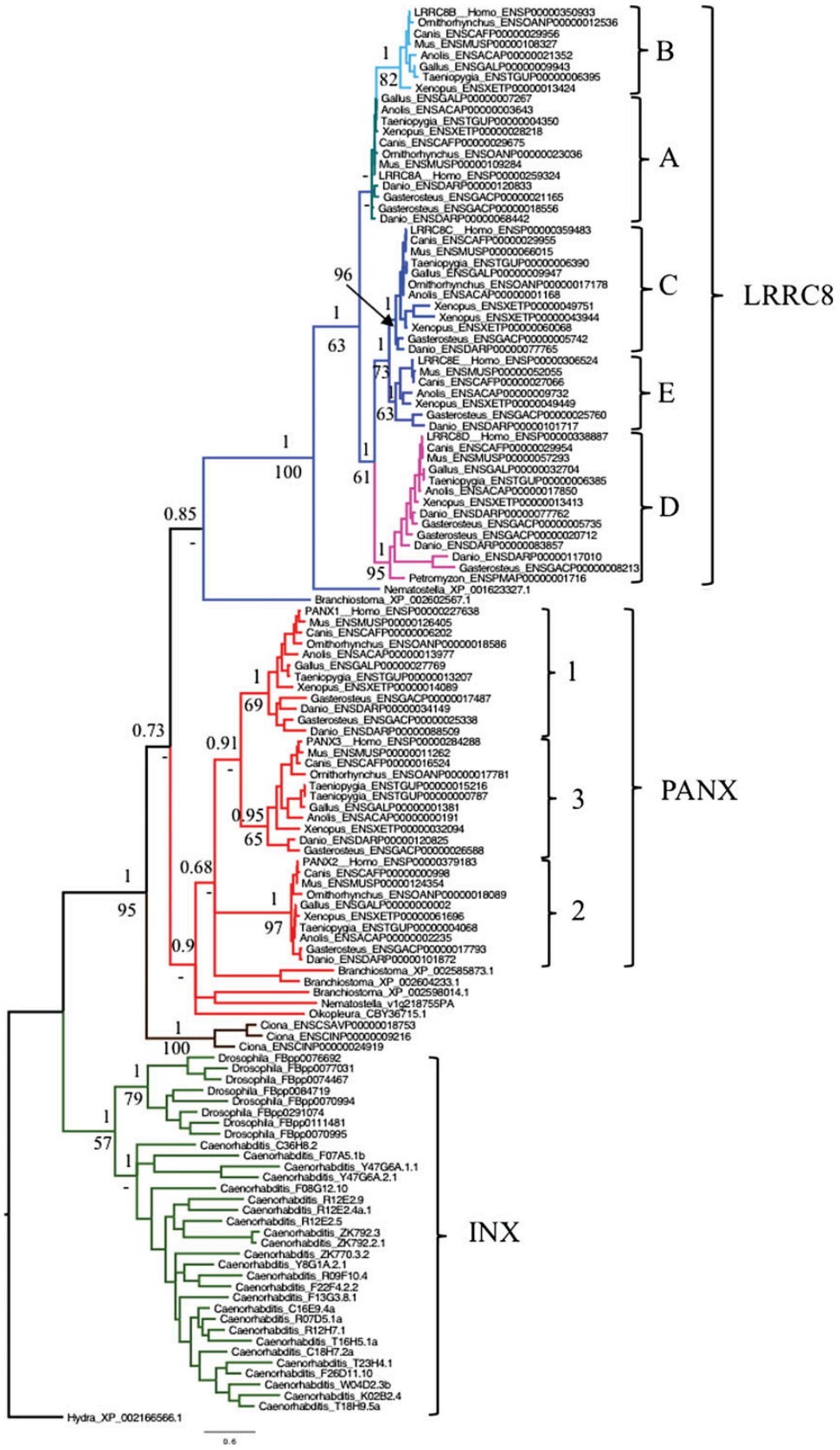
LRRC8B__Homo_ENSP00000350933
Ornithorhynchus_ENSOANP00000012536
Canis_ENSCAFP00000029956
Mus_ENSMUSP00000108327
Anolis_ENSACAP00000021352
Gallus_ENSGALP00000029943
Taeniopygia_ENSTGUP00000006395
Xenopus_ENSXETP00000013424
B
Gallus_ENSGALP00000007267
Anolis_ENSACAP00000003643
Taeniopygia_ENSTGUP00000004350
Xenopus_ENSXETP00000028218
Canis_ENSCAFP00000029675
Ornithorhynchus_ENSOANP00000023036
Mus_ENSMUSP00000109284
LRRC8A__Homo_ENSP00000259324
Danio_ENSDARP00000120833
Gasterosteus_ENSGACP00000021165
Gasterosteus_ENSGACP00000018556
Danio_ENSDARP00000068442
A
LRRC8C__Homo_ENSP00000359483
Canis_ENSCAFP00000029955
Mus_ENSMUSP00000066015
Taeniopygia_ENSTGUP00000006390
Gallus_ENSGALP00000009947
Ornithorhynchus_ENSOANP00000017178
Anolis_ENSACAP00000001168
Xenopus_ENSXETP00000049751
Xenopus_ENSXETP00000043944
Xenopus_ENSXETP00000060068
Gasterosteus_ENSGACP00000005742
Danio_ENSDARP00000077765
C
LRRC8E__Homo_ENSP00000306524
Mus_ENSMUSP00000052055
Canis_ENSCAFP00000027066
Anolis_ENSACAP00000009732
Xenopus_ENSXETP00000049449
Gasterosteus_ENSGACP00000025760
Danio_ENSDARP00000101717
E
LRRC8D__Homo_ENSP00000338887
Canis_ENSCAFP00000029954
Mus_ENSMUSP00000057293
Gallus_ENSGALP00000032704
Taeniopygia_ENSTGUP00000006385
Anolis_ENSACAP00000017850
Xenopus_ENSXETP00000013413
Danio_ENSDARP00000077762
Gasterosteus_ENSGACP00000005735
Gasterosteus_ENSGACP00000020712
Danio_ENSDARP00000083857
Danio_ENSDARP00000117010
Gasterosteus_ENSGACP00000008213
D
LRRC8
Petromyzon_ENSPMAP00000001716
Nematostella_XP_001623327.1
Branchiostoma_XP_002602567.1
PANX1__Homo_ENSP00000227638
Mus_ENSMUSP00000126405
Canis_ENSCAFP00000006202
Ornithorhynchus_ENSOANP00000018586
Anolis_ENSACAP00000013977
Gallus_ENSGALP00000027769
Taeniopygia_ENSTGUP00000013207
Xenopus_ENSXETP00000014089
Gasterosteus_ENSGACP00000017487
Danio_ENSDARP00000034149
Gasterosteus_ENSGACP00000025338
Danio_ENSDARP00000088509
1
PANX3__Homo_ENSP00000284288
Mus_ENSMUSP00000011262
Canis_ENSCAFP00000016524
Ornithorhynchus_ENSOANP00000017781
Taeniopygia_ENSTGUP00000015216
Taeniopygia_ENSTGUP00000000787
Gallus_ENSGALP00000001381
Anolis_ENSACAP00000000191
Xenopus_ENSXETP00000032094
Danio_ENSDARP00000120825
Gasterosteus_ENSGACP00000026588
3
PANX
PANX2__Homo_ENSP00000379183
Canis_ENSCAFP00000000998
Mus_ENSMUSP00000124354
Ornithorhynchus_ENSOANP00000018089
Gallus_ENSGALP00000000002
Xenopus_ENSXETP00000061696
Taeniopygia_ENSTGUP00000004068
Anolis_ENSACAP00000002235
Gasterosteus_ENSGACP00000017793
Danio_ENSDARP00000101872
2
Branchiostoma_XP_002585873.1
Branchiostoma_XP_002604233.1
Branchiostoma_XP_002598014.1
Nematostella_v1g218755PA
Okopleura_CBY36715.1
Ciona_ENSCSAVP00000018753
Ciona_ENSCINP00000009216
Ciona_ENSCINP00000024919
Drosophila_FBpp0076692
Drosophila_FBpp0077031
Drosophila_FBpp0074467
Drosophila_FBpp0084719
Drosophila_FBpp0070994
Drosophila_FBpp0291074
Drosophila_FBpp0111481
Drosophila_FBpp0070995
Caenorhabditis_C36H8.2
Caenorhabditis_F07A5.1b
Caenorhabditis_Y47G6A.1.1
Caenorhabditis_Y47G6A.2.1
Caenorhabditis_F08G12.10
Caenorhabditis_R12E2.9
Caenorhabditis_R12E2.4a.1
Caenorhabditis_R12E2.5
Caenorhabditis_ZK792.3
Caenorhabditis_ZK792.2.1
Caenorhabditis_ZK770.3.2
Caenorhabditis_Y8G1A.2.1
Caenorhabditis_R09F10.4
Caenorhabditis_F22F4.2.2
Caenorhabditis_F13G3.8.1
Caenorhabditis_C16E9.4a
Caenorhabditis_R07D5.1a
Caenorhabditis_R12H7.1
Caenorhabditis_T16H5.1a
Caenorhabditis_C18H7.2a
Caenorhabditis_T23H4.1
Caenorhabditis_F26D11.10
Caenorhabditis_W04D2.3b
Caenorhabditis_K02B2.4
Caenorhabditis_T18H9.5a
INX
Hydra_XP_002166566.1
0.6

Figure 1.17. ML phylogeny of LRRC8 proteins, and non-chordate innexins and chordate pannexins. A cnidarian (*Hydra*) innexin was used as the outgroup. Bayesian posterior probabilities and ML bootstrap support values are shown above and below nodes, respectively. Dash indicates bootstrap and Bayesian posterior probability below 50% and 0.5, respectively. (Figure and legend modified from Abascal and Zardoya, 2012. Reprint from WILEY Periodicals, Inc: Bioessays)[134]

Sequence alignment of Panxs and LRRC8 proteins reveals several well-conserved structural regions such as four TM helices, residues preceding the TM2 helix and several charged residues in the CL[134] (**Figure 1.18**). Notably, Panxs and LRRC8 share more conserved regions than Panxs and Inxs (**Figure 1.18**, **1.19**), consistent with the phylogeny of Panxs, Inxs and LRRC8 proteins[37,134].

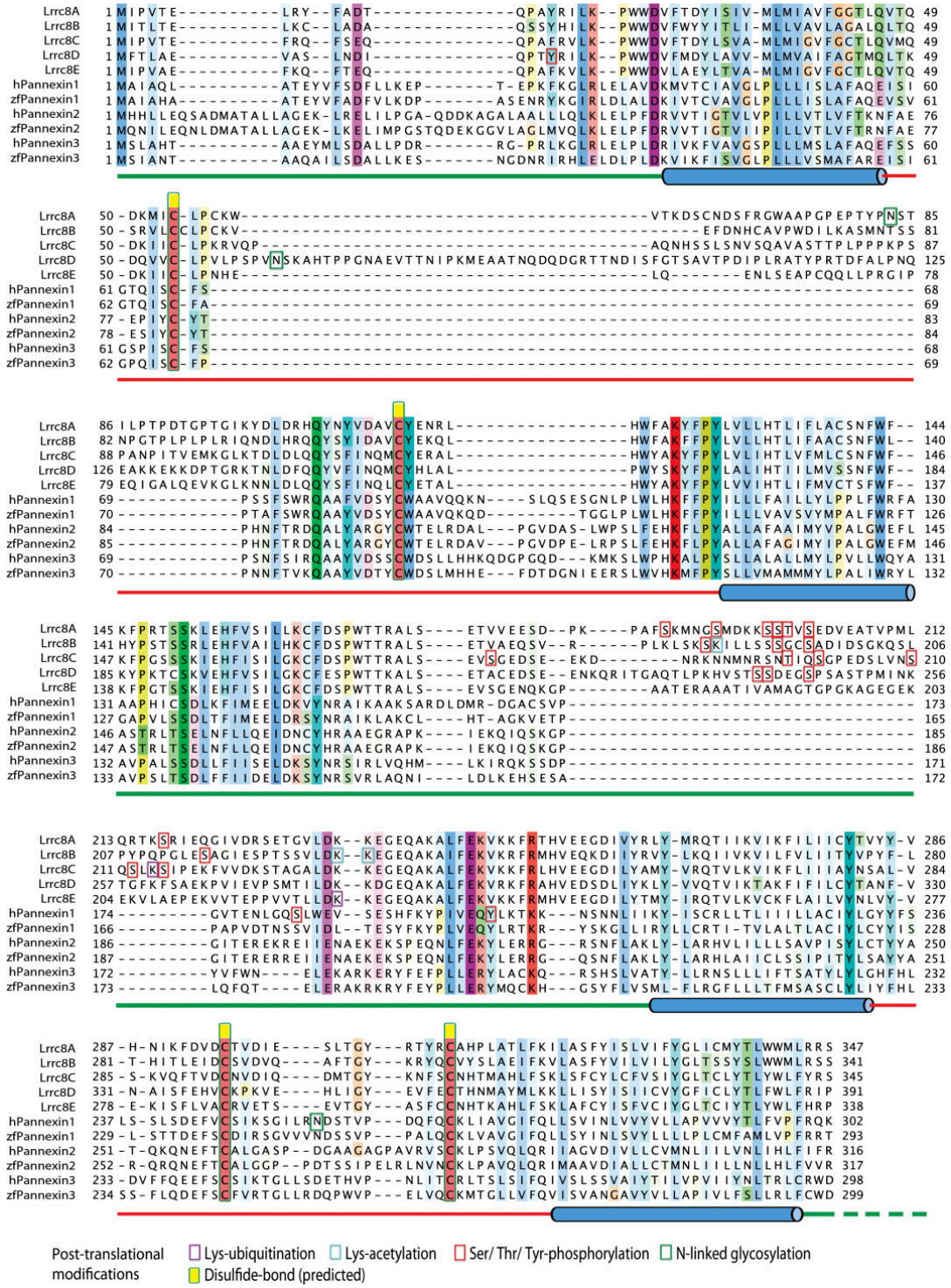

Figure 1.18. Alignment of pannexins and LRRC8 proteins. Residues are coloured according to their physicochemical properties and to the degree of conservation with JalView. The presence of TM helices (blue cylinders) and intracellular (green) and extracellular (red) regions is shown at the bottom. Post-translational modifications are highlighted, as indicated in the legend. (Figure and legend modified from Abascal and Zardoya, 2012. Reprint from WILEY Periodicals, Inc: Bioessays)[134]

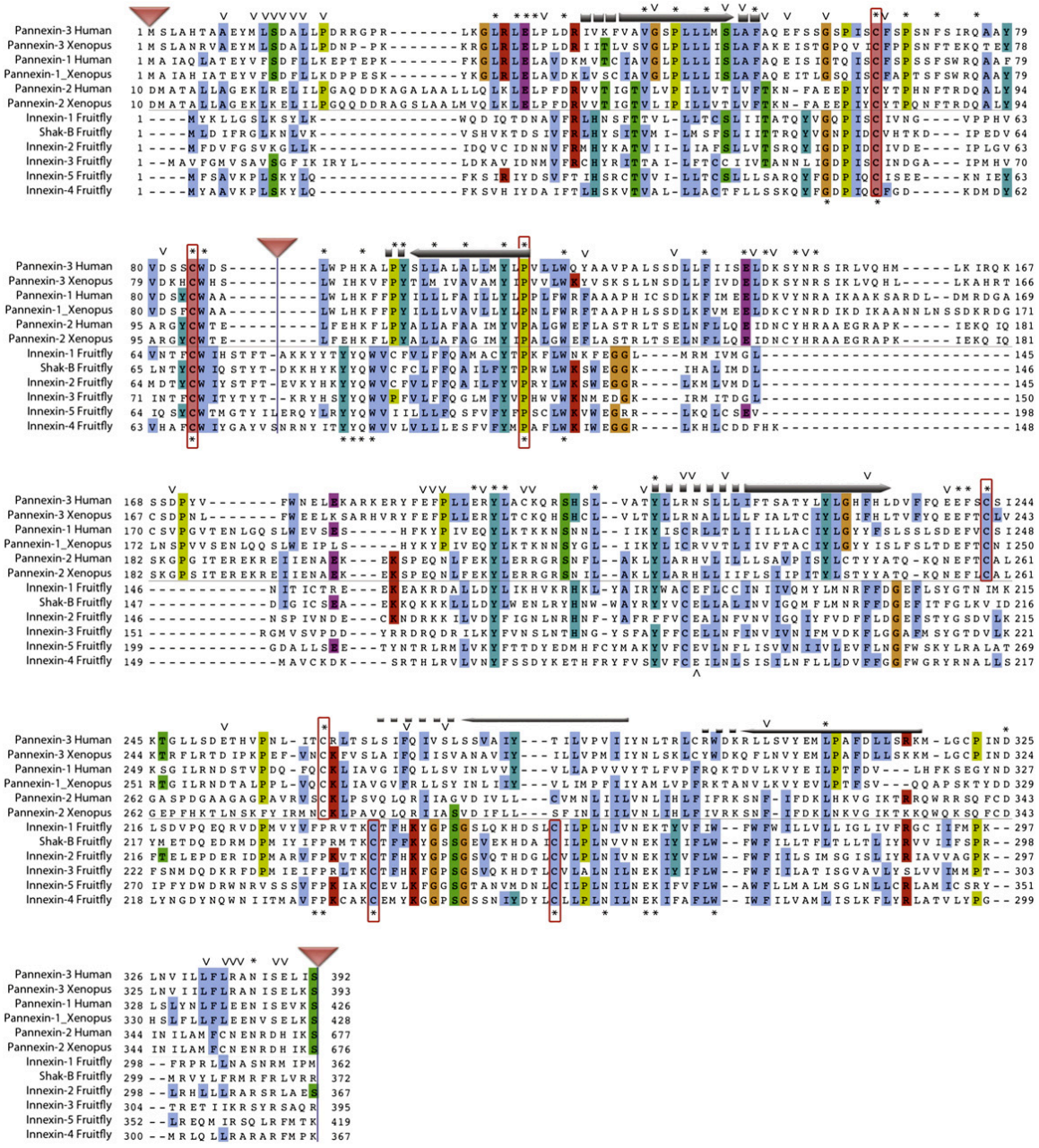

Figure 1.19. Alignment of pannexins and innexins. Human and frog pannexins were aligned to six selected fruit fly innexin paralogs and visualized using JalView. Gray boxes on top of the alignment represent transmembrane helix predictions. Dotted boxes indicate those predictions that did not align well, particularly in the case of the fourth helix. Inverted red triangles indicate points at which the alignment was trimmed, including N- and C terminal regions and the first extracellular loop. Arrows correspond to sites that are conserved in each pannexin subfamily but are variable between them (they were calculated from a larger alignment of pannexins). Asterisks at the top of the alignment indicate sites conserved in a larger alignment of pannexins. Asterisks at the bottom indicate sites highly conserved in an alignment of many innexins. Conserved cysteine and proline residues are shown within red boxes. (Figure and legend modified from Abascal and Zardoya, 2013. Reprint from Elsevier B.V.: Biochim Biophys Acta)[37]

By considering the sequence alignment of Panxs and LRRC8 proteins[134] (**Figure 1.18**), and the structure of LRRC8A (PD)[139] (**Figure 1.20**), it reveals that the α-helical regions are well conserved, including four TM helices (corresponding to TM1-TM4 in the structure), region just before TM2 (corresponding to E1H in the structure)[134], and regions just after TM2 and just before TM3 in the CL (corresponding to CLH1 and CLH2, respectively, in the structure). Interestingly, locations of these two α-helices in the CL of LRRC8A are similar to that of Panx1 revealed by circular dichroism (CD) spectroscopy[39] (**Figure 1.4**). Two large sequence variable insertions (in TM1-2 and TM2-3 loops) in the sequence alignment may correspond to the loop between E1β and E1H, and the loop between CLH1 and CLH2 in the structure, which are acting as the target for post-translational modifications such as glycosylation and phosphorylation[134] (**Figure 1.16**). In addition to the sequence and structural similarities, LRRC8 proteins also share other significant properties with Panxs including expression in nervous and immune systems, subcellular localization, activation by hypotonicity, inhibition by carbenoxolone, and permeation of large molecules such as ATP[106,134-136,167-169].

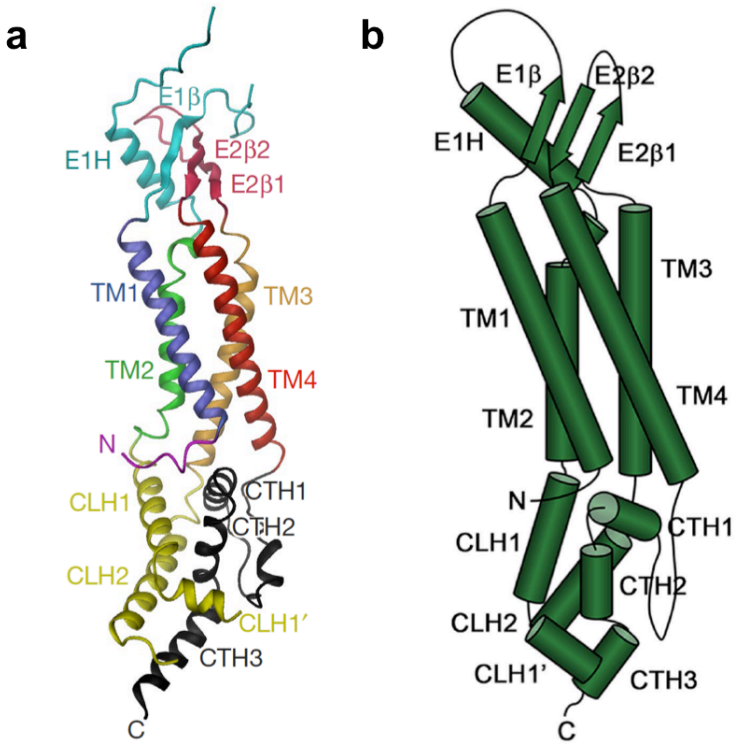

Figure 1.20. The structure of LRRC8A pore domain. Ribbon representation **(a)** and solid-cylinder representation **(b)** of the LRRC8A pore domain monomer structure, with secondary structure elements indicated. (Figure and legend modified from Deneka *et al*., 2018. Reprint from Macmillan Publishers Limited: Nature)[139]

Chapter 2

Structure-Function Analysis of Caspase Cleavage Mediated Activation of Pannexin 1 Channels

2.1 Introduction

Pannexin 1 (Panx1) forms an oligomeric membrane protein channel, which shares a common membrane topology with connexins, the vertebrate gap junction channels, and innexins, the invertebrate gap junction channels, as well as recently identified CALHM1 and LRRC8 (SWELL) protein channels[12,13,134,138]. Each Panx1 subunit contains four transmembrane domains that are connected by two extracellular loops, one cytoplasmic loop, and cytoplasmic amino and carboxyl termini. Panx1 channels can be activated by various stimuli, including mechanical stress[24,49], membrane depolarization[19,49,60], elevated extracellular potassium[58,61-65], increased intracellular calcium[34,66], receptor-mediated signaling pathways[34,55,68,69,71,72,75], and caspase cleavage of the distal C-terminus[50,77-79]. Upon activation, Panx1 channels allow permeation of molecules such as nucleotides (ATP and UTP) and fluorescent dyes (To-Pro and Lucifer Yellow) across the plasma membrane[28,49,50]. Panx1 is ubiquitously expressed in human tissues[13] and thus plays an important role as an ATP release channel[21,105] in diverse physiological and pathological processes, including blood pressure regulation[24,68,69], apoptotic cell clearance[50,119], inflammation[55,120], neurological

disorders[56,63,72,126,127], cardiac fibrosis[130] and cancer aggressiveness and metastasis[131,132].

The C-terminal domain of pannexin is most variable, and may play an essential role in channel regulation[37]. Several biochemical and physiological studies have investigated the function of the C-terminus and discovered a unique activation mechanism induced by caspase cleavage. Wang *et al.* characterized the pore lining residues using the substituted cysteine accessibility method (SCAM). They concluded that portions of the N-terminal region line the boundary of the channel pore, and the distal C-terminus lines the inner region of the pore[40]. Chekeni *et al.* identified a caspase cleavage site ($_{376}$DVVD$_{379}$) in the C-terminus. Panx1 channels are activated by caspase cleavage of the C-terminal tails at this site, which result in the release of nucleotides such as ATP and UTP serving as 'find-me' signals that attract phagocytes for clearance of dying cells during apoptosis of T lymphocytes[50]. This mechanism was subsequently confirmed in a mouse model[77]. Sandilos *et al*. used purified and activated caspase-3 to show that caspase cleavage-mediated activation could occur independent of apoptosis. They also showed that the purified Panx1 C-terminal tail (CT) can inhibit caspase cleavage induced channel activity, and its removal from the channel pore is essential for activation[78]. More recently, caspase cleavage-mediated activation of Panx1 at the same C-terminal cleavage site by caspase-11 was observed during lipopolysaccharide-induced pyroptosis[79]. Taken together, it is proposed that the CT functions as a pore-blocking plug to maintain Panx1 channel in an inactive

state and caspase cleavage allows the CT to dissociate from the pore and irreversibly activate the channel. Despite clear demonstration of this proteolytic cleavage-mediated activation mechanism, the associated changes in channel conformation and pore structure remain unknown.

Here, we used electron microscopy (EM) to show that caspase cleavage of the CT yields a capacious central pore. The fully activated conformation of Panx1 channel displays an outwardly rectifying unitary conductance (<100 pS maximum) that accounts for voltage dependence of Panx1 current.

2.2 Results and discussion

2.2.1 Purified Panx1 was efficiently cleaved in vitro by caspase-3

Panx1 channels are activated by caspase cleavage of the C-terminal autoinhibitory regions, resulting in ionic currents and permeation of molecules such as ATP[50,78]. To explore the caspase cleavage-mediated activation mechanism, we directly compared the structures of full-length and caspase-cleaved Panx1 channels using electron microscopy (EM). A thermally stable, homogenous and monodisperse protein sample is a prerequisite for EM-based

structural analysis. Thus, we first tested whether purified Panx1 solubilized in detergent could be cleaved *in vitro* by caspase, and then optimized the protein sample to meet such a criterion.

Initially, full-length human Panx1 was expressed in *Sf9* insect cells and extracted using the detergent Lauryl Maltose Neopentyl Glycol (LMNG). The His-tagged, detergent-solubilized Panx1 was purified by immobilized metal affinity chromatography (IMAC). Caspase cleavage was performed by incubation of purified Panx1 with caspase-3. Coomassie blue stained SDS-PAGE, Western immunoblot analysis with anti C-terminal histidine antibodies and matrix-assisted laser desorption ionization mass spectrometry (MALDI-MS) analysis of intact protein samples confirmed the efficient cleavage by caspase-3 at the C-terminal cleavage site ($_{376}$DVVD$_{379}$) (**Figure 2.1a**,**b**). The stability of full-length and caspase-cleaved Panx1 was characterized using a fluorescence-based thermal stability assay (FTSA). The quantum yield increases upon temperature-induced protein unfolding when cysteine residues embedded within the protein interior become accessible for binding to a fluorophore. In the detergent LMNG, however, neither full-length nor caspase-cleaved Panx1 was thermally stable since they started to unfold at ~30 ^{o}C (**Figure 2.1c**). Size exclusion chromatography (SEC) showed multiple UV 280 nm absorbance peaks for both full-length and caspase-cleaved Panx1, indicating that neither species was homogenous, with aggregated and dissociated protein subunits (**Figure 2.1d**). Negative-stain electron microscopy (EM) of full-length Panx1 showed aggregated particles,

whereas caspase-cleaved Panx1 contained much smaller particles than the expected oligomeric channel, presumably due to dissociation of the oligomers (**Figure 2.1e**). Although Panx1 was efficiently cleaved by caspase-3 in LMNG, neither full-length nor caspase-cleaved Panx1 was thermally stable or homogenous, indicating that these protein samples were not suitable for structural analysis by EM.

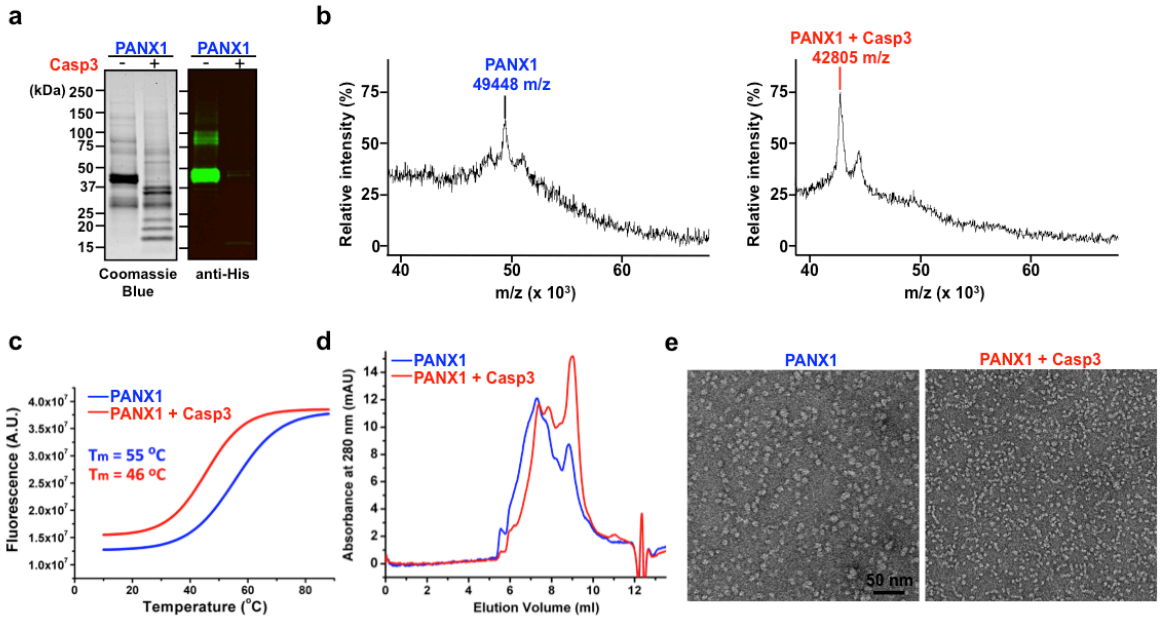

Figure 2.1. Panx1 purified in the detergent LMNG was cleaved *in vitro* by caspase-3 (Casp3). (a) Coomassie Blue stained SDS-PAGE showed full-length (~48 kDa) and Casp3-cleaved (~42 kDa) Panx1. Western immunoblot probed with anti-histidine antibodies showed diminished signal for Casp3-cleaved Panx1 due to removal of the C-terminal histidine tag. **(b)** MALDI-MS showed mass-to-charge (m/z) ratio of full-length (49.448 kDa) and Casp3-cleaved (42.805 kDa) Panx1. **(c)** Fluorescent thermal stability assay (FTSA) showed neither full-length (blue) nor Casp3-cleaved (red) Panx1 in the detergent LMNG was thermally stable. **(d)** Size-exclusion chromatography (SEC) showed neither full-length (blue) nor Casp3-cleaved (red) Panx1 was homogenous. **(e)** Negatively-stained electron micrographs of full-length and Casp3-cleaved Panx1 (scale bar = 50 nm).

In order to improve the stability and homogeneity of Panx1, we performed a differential filtration assay (DFA) to screen optimal detergents for solubilization and purification. This assay is designed to assess the stability of a membrane protein by screening 94 detergents and testing for filtration through supports with high (300 kDa) and low (100 kDa) molecular weight cut-offs (MWCO). In the optimal detergent, the protein will display minimal aggregation or degradation[170]. We obtained a small subset of detergents that do not disrupt Panx1 oligomers or cause aggregation (**Figure 2.2**, **Table 2.1**).

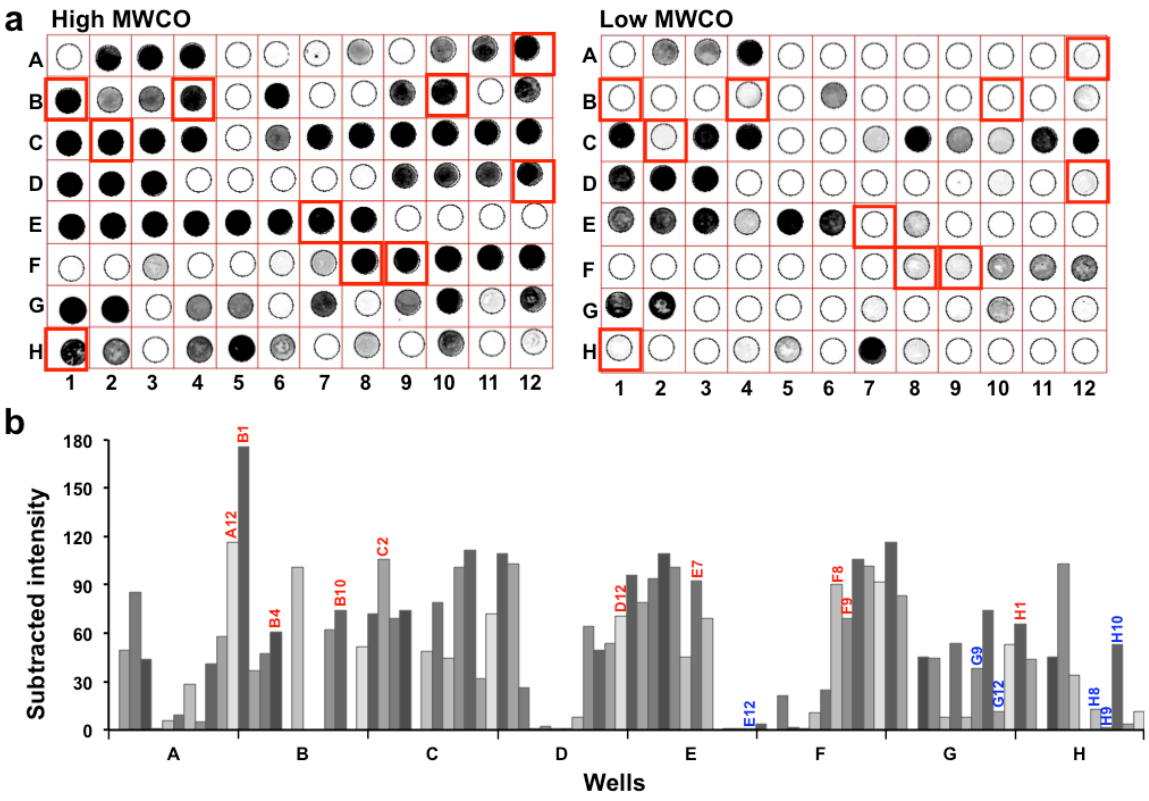

Figure 2.2. Detergent screen by differential filtration assay (DFA). (a) Dot-immunoblot showed detergent-solubilized Panx1 with minimal aggregation and degradation was able to pass through a nitrocellulose membrane with high molecular weight cutoff (MWCO) of 300 kDa but not low MWCO of 100 kDa. Screened detergents are indicated with red boxes. **(b)** Densitometry of dot-immunoblot difference between high and low MWCO shown in (a). Detergents used before performing DFA (blue), and screened from DFA (red) are listed in Table 2.1.

Well	Abbreviation	Detergent Name	CMC (mM)	Working Conc. (mM)	Vendor	Purification Test
A12	CF-6	CYCLOFOS-6	2.68	8.04	Anatrace	+
B1	CF-7	CYCLOFOS-7	0.62	6.2	Anatrace	+
B4	FC-12	FOS-CHOLINE-12	1.5	4.5	Anatrace	-
B10	6-DHPC	1,2-Dihexanoyl-sn-glycero-3-phosphocholine	15	30	Avanti	-
C2	FOSFEN-9	FOSFEN-9	1.35	4.05	Anatrace	-
D12	C8E6	Hexaethylene glycol monooctyl ether	10	25	Anatrace	-
E7	CHAP	Big CHAP	2.9	8.7	Anatrace	+
E12	OG*	n-Octyl-β-D Glucopyranoside	18	36	Anatrace	+
F8	C-HEGA-10	C-Hega-10	35	70	Anatrace	-
F9	C-HEGA-11	C-Hega-11	11.5	23	Anatrace	-
G9	UDM*	n-Undecyl-β-D-maltopyranoside	0.59	5.9	Anatrace	+
G12	DDM*	n-Dodecyl-β-D-maltopyranoside	0.17	8.5	Anatrace	+
H1	TDM	n-Tridecyl-β-D-maltopyranoside	0.03	1.5	Anatrace	+
H8	MNG-8*	Octyl Glucose Neopentyl Glycol	1.02	3.06	Anatrace	+
H9	MNG-10*	Decyl Maltose Neopentyl Glycol	0.036	3.6	Anatrace	+
H10	MNG-12*	Lauryl Maltose Neopentyl Glycol	0.01	1	Anatrace	+

* Detergents used for solubilization and purification before DFA screen.

Table 2.1. Detergents screened from DFA for Panx1 solubilization and purification. Well coordinates as shown in Figure 2.2.

We further tested the detergents screened from DFA by IMAC and SEC purification of full-length Panx1, and selected the detergent n-tridecyl-β-D-maltopyranoside (TDM) as a good candidate for the caspase cleavage experiment. We purified full-length human Panx1 that was expressed in the plasma membrane of *Sf9* insect cells (**Figure 2.3a**) in TDM using the same methods as described above for LMNG. Similar to LMNG, purified Panx1 in TDM was efficiently cleaved *in vitro* by caspase-3 (**Figure 2.3b**). In order to obtain more homogenous Panx1 samples, we performed two rounds of SEC after IMAC purification and caspase cleavage. The second round of SEC showed a single UV280 nm absorbance peak for both full-length and caspase-cleaved Panx1, indicating that both species are oligomeric without dissociated subunits (**Figure**

2.3c). Notably, full-length Panx1 showed significantly increased thermal stability with a melting temperature (T_m) of 61 ^oC, and the unfolding started at ~50 ^oC. However, caspase-cleaved Panx1 showed reduced thermal stability with T_m of 39 ^oC, and the unfolding started at ~25 ^oC (**Figure 2.3d**). Negative-stain EM of full-length and caspase-cleaved Panx1 in TDM demonstrated monodisperse particles with less aggregation or dissociation compared to LMNG (**Figure 2.3e**).

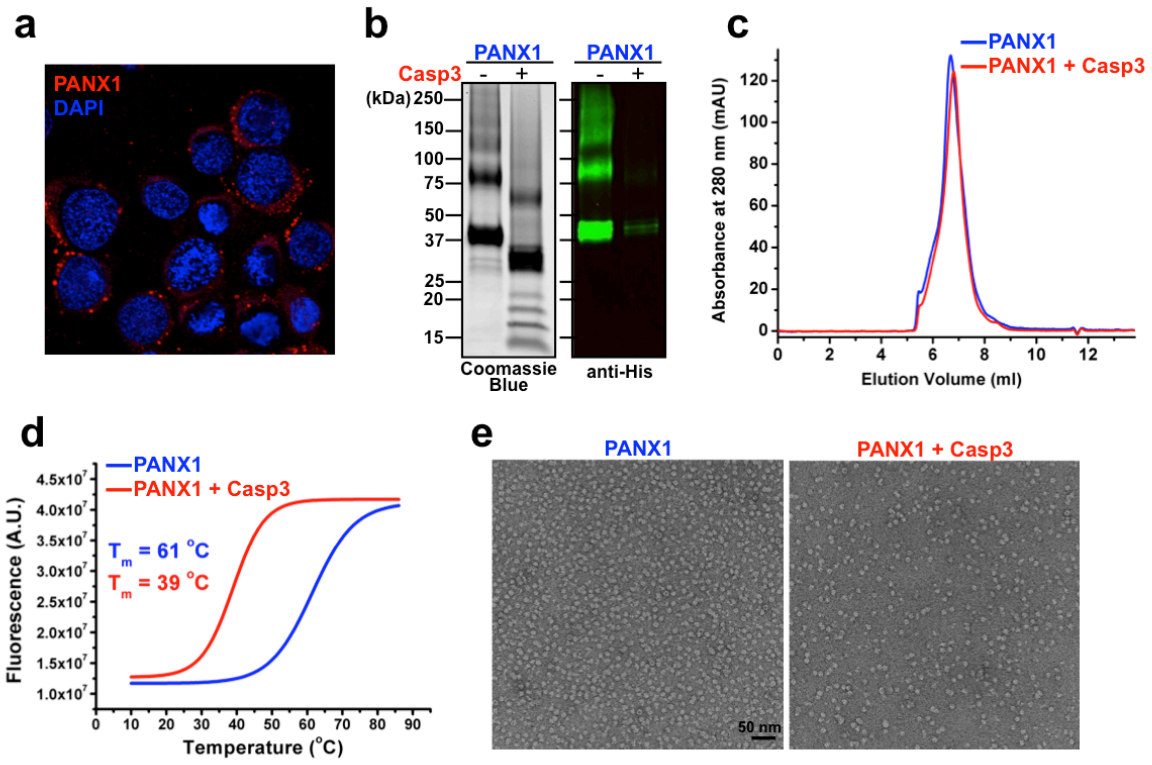

Figure 2.3. Panx1 purified in the detergent TDM was cleaved *in vitro* by caspase-3 (Casp3). (a) Immunofluorescence microscopy showed localization of full-length human Panx1 (red) in the plasma membranes of *Sf9* insect cells. **(b)** Coomassie Blue stained SDS-PAGE showed full-length (~48 kDa) and Casp3-cleaved (~42 kDa) Panx1. Western immunoblot probed with anti-histidine antibodies showed diminished signal for Casp3-cleaved Panx1 due to removal of the C-terminal histidine tag. **(c)** SEC showed both full-length (blue) and Casp3-cleaved (red) Panx1 were homogenous. **(d)** FTSA showed full-length Panx1 (blue) was thermally stable, whereas Casp3-cleaved Panx1 (red) was not stable. **(e)** Negative-stain EM of full-length and Casp3-cleaved Panx1 (scale bar = 50 nm). (Membrane localization assay in (a) was performed by Dr. Susan Leonhardt and Dr. Brad Bennett, University of Virginia)

Although full-length Panx1 was much more thermally stable in TDM compared to LMNG, it became unstable upon removal of the C-terminal tails as revealed by FTSA (**Figure 2.1c**, **2.3d**). In order to improve the stability of caspase-cleaved Panx1, IMAC purified full-length Panx1 in TDM was exchanged to amphipols, which are amphiphilic polymers designed to solubilize membrane proteins in an 'amphipol belt' that resembles the lipid bilayer, thereby improving protein stability compared to detergent[171,172]. C-terminal tail cleavage was performed by addition of caspase-3 during amphipol exchange. Commassie blue stained SDS-PAGE and Western immunoblot analysis with anti-His antibodies showed that the efficiency of cleavage by caspase-3 in amphipols was similar to that in TDM (**Figure 2.4a**, **2.3b**). Both full-length and caspase-cleaved Panx1 formed homogenous oligomers as shown by SEC (**Figure 2.4b**). Surprisingly, caspase-cleaved Panx1 demonstrated significantly improved thermal stability (T_m = 62 °C, **Figure 2.4c**) in amphipols compared to TDM (T_m = 39 °C, **Figure 2.3d**). Thus, both full-length and caspase-cleaved Panx1 formed thermally stable and homogenous oligomers in amphipols, which are amenable for structural analysis by EM.

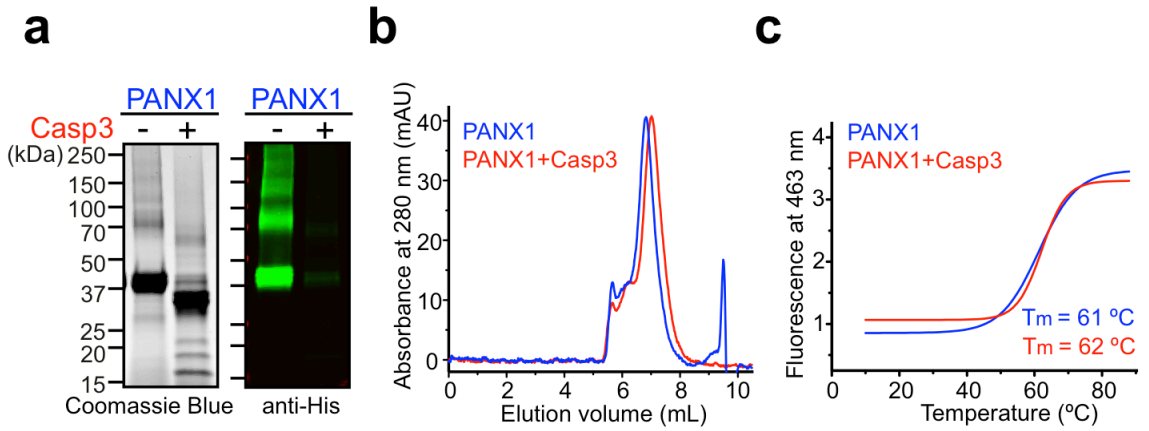

Figure 2.4. Panx1 exchanged into amphipols was cleaved *in vitro* by caspase-3 (Casp3)[48]. (a) Coomassie Blue stained SDS-PAGE showed full-length (~48 kDa) and Casp3-cleaved (~42 kDa) Panx1. Western immunoblot probed with anti-histidine antibodies showed diminished signal for Casp3-cleaved Panx1 due to removal of the C-terminal histidine tag. **(b)** SEC showed both full-length (blue) and Casp3-cleaved (red) Panx1 were homogenous. **(c)** FTSA showed both full-length (blue) and Casp3-cleaved (red) Panx1 were thermally stable.

2.2.2 Panx1 pore revealed by caspase cleavage-mediated activation

We performed negative-stain EM and single-particle image analysis of full-length and caspase-cleaved Panx1 in amphipols, as well as single-channel recording in mammalian cells, to discern how caspase cleavage of the C-terminus changes the channel structure and activity.

Electron micrographs of negatively stained full-length and caspase-cleaved Panx1 in amphipols were subjected to image processing using EMAN2 software[173] to obtain two-dimensional (2D) class averages, with or without imposing six-fold symmetry[58] (**Figure 2.5**). In three independent determinations

using different sets of micrographs from full-length and caspase-cleaved channels, class averages displayed a ring-shaped appearance, and there appeared to be two different *en face* orientations (**Figure 2.5**). In one orientation, there was a small but obvious area of reduced density at the center of the structure, presumably the channel pore (**Figure 2.5**); this orientation likely reflects a view from the extracellular face, since it was similar for both full-length and caspase-cleaved Panx1, even after cleavage of the cytoplasmic C-terminal tail. In the other orientation, however, there was a major difference between full-length and caspase-cleaved channels: a strikingly pronounced area of reduced central density was visible only in caspase-cleaved Panx1 (**Figure 2.5b**). This more prominent 'pore' region was not seen in any of the class averages obtained from the full-length Panx1, despite systematically varying the numbers of classes used for averaging from 8 to 100 in three independent analyses. The larger 'pore' that appeared after caspase-3 treatment suggests that this orientation represents a view from the cytoplasmic side of the channel, where the caspase cleavage site is located[50], and supports evidence that cleavage activates Panx1 by removing a pore-associated C-terminal autoinhibitory region[78]. Notably, the 'pore' structure observed after caspase cleavage is more pronounced than reported for channels exposed to high potassium[58], especially from the presumed cytoplasmic orientation.

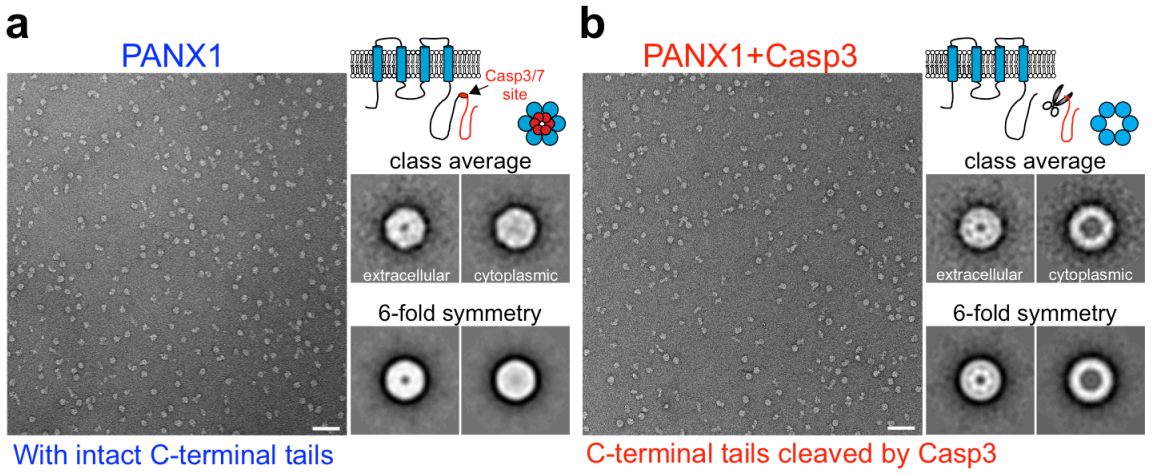

Figure 2.5. C-terminal cleavage by caspase-3 results in a distinctive Panx1 pore structure[48]. Electron micrograph and 2D class averages of negatively stained **(a)** full-length Panx1 (from 125 or 282 of 5,970 particles for the putative extracellular or cytoplasmic view, respectively) or **(b)** caspase-cleaved Panx1 (from 79 or 56 of 6,892 particles); six fold symmetry was imposed on the indicated images[58]. Schematics show the caspase cleavage site and expected cytoplasmic views of Panx1 hexameric channels, before and after cleavage. Scale bar, 50 nm.

Inside-out patch recordings were used to characterize the single-channel properties of caspase-cleaved Panx1 channels in mammalian cells. The characteristic Panx1 channel activity was not observed immediately after excising inside-out membrane patches from HEK293T cells, consistent with earlier reports that full-length human Panx1 channels are basally silent[50,78]. Nonetheless, channel activity that was sensitive to carbenoxolone (CBX), a known Panx1 channel inhibitor, could be induced by exposing these previously silent patches to activated caspase-3 (**Figure 2.6a**). Regarding the steady-state properties of the fully 'open' channels, there were several remarkable observations. First, caspase-cleaved channels displayed an outwardly rectifying current-voltage (*I-V*) relationship, with a maximal unitary conductance of 96.2±2.0

pS at positive membrane potentials and 12.2±0.2 pS at negative potentials (**Figure 2.6b,c**). In addition, we did not observe openings to sub-conductance states. These results are different from the previously reported high-conductance channels (~500 pS) that were recorded from *Xenopus* oocytes in high extracellular K^+, with a linear single-channel *I-V* relationship and multiple sub-conductance states[49]. Second, the channel activity (open probability, P_O) was similar over a broad range of membrane potentials (-80 mV to +80 mV) (**Figure 2.6d**), indicating that gating of caspase-cleaved Panx1 is independent of voltage, although Panx1 channels are often considered voltage-dependent.

We obtained the same results from wild-type, untagged Panx1, confirming that these channel properties were not affected by the C-terminal epitope tag present initially on the full-length Panx1 construct (**Figure 2.7a**), likely reflecting the fact that the tag is removed by caspase cleavage. Moreover, similar channel properties were observed in cell-attached recordings from HEK293T cells expressing C-terminally truncated Panx1, despite slightly smaller unitary conductance at positive membrane potentials (~75 pS) (**Figure 2.7b-d**).

On the basis of EM and single-channel recording analyses, we conclude that Panx1 channels are activated by caspase cleavage, independent of voltage, resulting in a prominent 'pore' structure and an outwardly rectifying unitary conductance (<100 pS) at depolarized potentials.

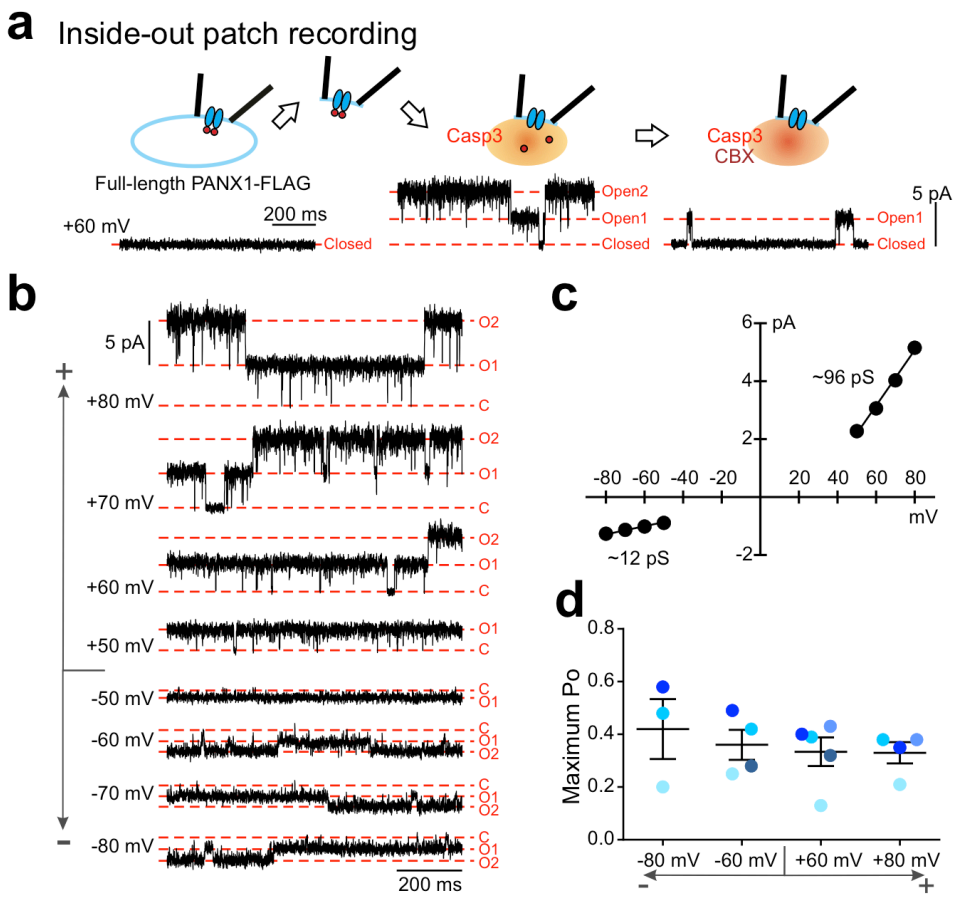

Figure 2.6. C-terminal cleavage by caspase-3 results in maximum unitary conductance of ~96 pS[48]. **(a)** Inside-out recordings from HEK293T cells expressing full-length PANX1-FLAG following membrane excision, and after exposure to activated caspase-3 (Casp3) and carbenoxolone (CBX, 50 μM). **(b)** Steady-state activity of caspase-activated, full-length PANX1-FLAG in an inside-out patch held at different potentials. C, closed state; O1 and O2, open-state amplitude for one and two channels. **(c)** Averaged single-channel current amplitudes at different patch potentials (± s.e.m., smaller than symbol size) reveal an outward-rectifying unitary conductance: 96.2±2.0 pS from +50 to +80mV (n=5) and 12.2±0.2 pS from -80 to -50mV (n=4). **(d)** Open probability of cleavage-activated PANX1-FLAG is independent of membrane voltage. Data from each patch is represented by a different colour. (Experiments performed by Dr. Yu-Hsin Chiu, Dr. Douglas Bayliss Laboratory, University of Virginia)

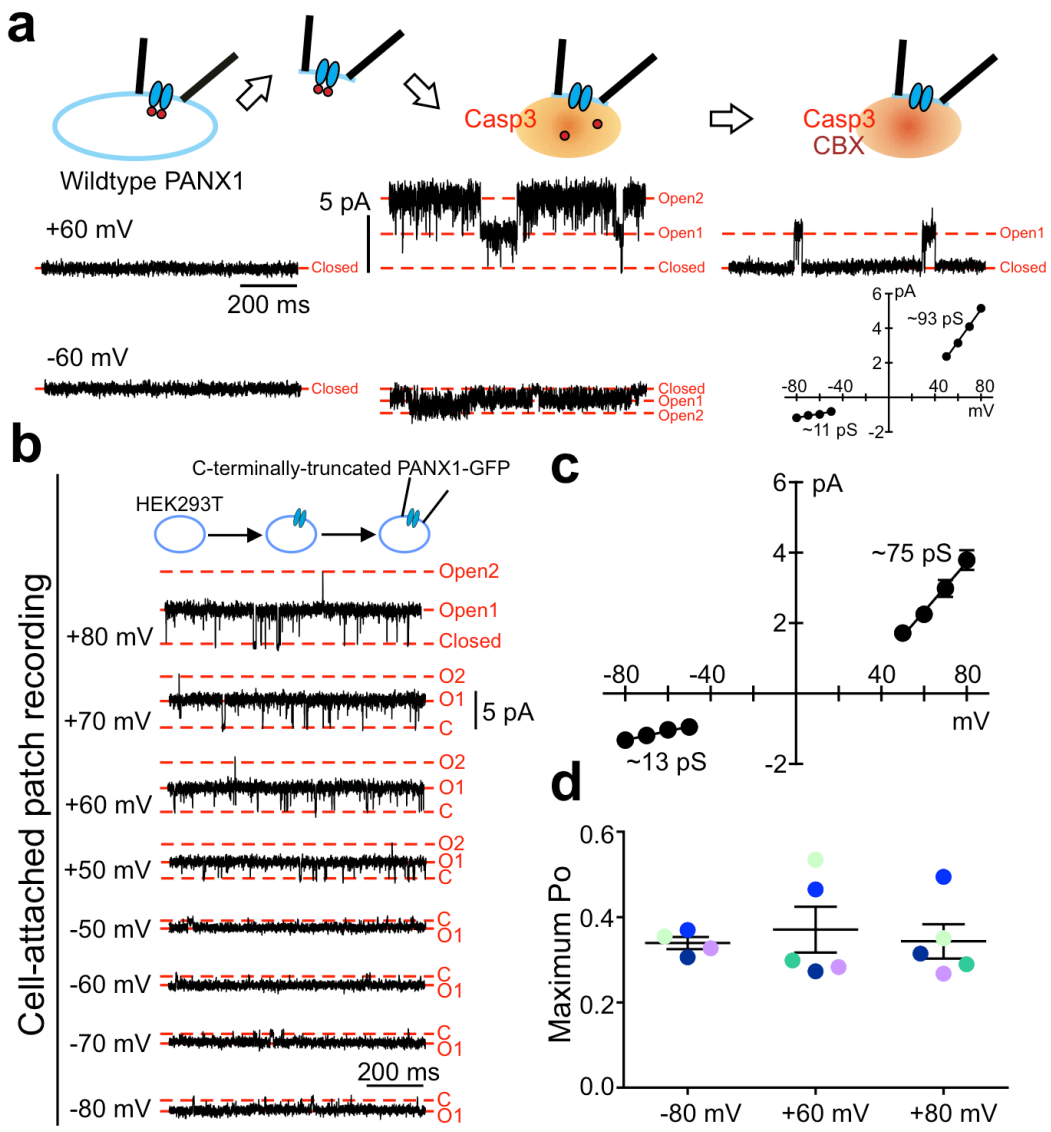

Figure 2.7. Single-channel properties of C-terminally truncated Panx1[48]. (a) Inside-out patch recording performed in HEK293T cells expressing wild-type, untagged PANX1. Examples of PANX1 single-channel activity recorded at +60 mV (upper) or -60 mV (lower), before (left) and after (middle) caspase-3 (Casp3) exposure, and after carbenoxolone (CBX, 50 μM) inhibition. Current-voltage (I-V) relationship (lower right) demonstrates that Casp3-cleaved wild-type PANX1 has unitary conductance of 93.0 ± 4.8 pS (at +50~+80 mV, n=3) and 11.4 ± 1.2 pS (at -80~-50 mV, n=3). **(b)** Examples of PANX1 single-channel activity obtained by cell-attached recording from HEK293T cells expressing C-terminally-truncated PANX1, with a GFP tag. C, closed state. O, open state. **(c)** I-V relationship obtained from cell-attached recordings demonstrates that C-terminally-truncated PANX1 has unitary conductance of 74.7 ± 3.6 pS (at +50~+80 mV, n=8) and 12.8 ± 1.2 pS (at -80~-50 mV, n=3). **(d)** Maximum Po of C-terminally-truncated PANX1 is similar across different patch potentials (-80, +60, and +80 mV). Data obtained from the same patch is labeled in the same color. (Experiments performed by Dr. Yu-Hsin Chiu, Dr. Douglas Bayliss Laboratory, University of Virginia)

2.2.3 Concluding remarks

Caspase cleavage of the C-terminal autoinhibitory regions of Panx1 irreversibly activates the channels, allowing permeation of molecules such as ATP across the plasma membrane[50,78]. To gain more insight into this unique caspase cleavage mediated-activation mechanism, we used EM and electrophysiology to investigate Panx1 channel structure and function associated with C-terminal cleavage induced channel activation.

The C-terminus is the most variable region in pannexin paralogs[37], suggesting that it may play an important role in channel regulation. SCAM analysis revealed that the distal C-terminus of Panx1 lines the inner region of the channel pore[40]. It was also showed that the C-terminal tails of Panx1 can inhibit cleavage-medicated channel activity, and its dissociation from the pore is required for activation[78]. In our EM analysis, we interpret the striking decrease in density of the central pore of Panx1 after removal of the C-terminal tails from full-length channel by caspase cleavage as physical displacement of the C-terminal tails from the channel pore. This interpretation supports the hypothesis that the C-terminus acts as a pore-blocking plug to maintain Panx1 channel in an inactive state and caspase cleavage allows the C-terminal tails to dissociate from the pore and activate the channel.

It is commonly considered that Panx1 is a voltage-dependent channel with large unitary conductance[49]. However, our observations of the voltage-

independent and comparatively small-conductance channel suggest reappraisal of the existing views on Panx1 channel property. In regard to voltage dependence, there does not appear to be any voltage sensitive gating mechanism since the channel open probability is not affected by the membrane potential. Regarding single channel conductance, fully activated Panx1 channels induced by caspase cleavage showed a unitary conductance of <100 pS, which is much smaller than that reported for Panx1 expressed in *Xenopus* oocytes under high extracellular K^+ (~500 pS)[49]. Similar small conductance of Panx1 channels have also been observed from mammalian cells expressing mouse Panx1[51,52].

.

2.3 Experimental methods

2.3.1 Cloning and expression of human Panx1

Full-length, wild-type, human Panx1 (NM_015368, Isoform 1, 426 a.a.) modified with a triple glycine (Gly-Gly-Gly) linker and a hexahistidine affinity tag at the carboxyl terminus was subcloned into the pFastBac1 vector (Invitrogen) for baculovirus expression in *Spodoptera frugiperda* (*Sf9*) insect cells using the Bac-to-Bac expression system (Invitrogen). Recombinant Panx1 baculovirus was used to infect *Sf9* cells at 27 ^{o}C with a density of 2 × 10^{6} ml^{-1} and multiplicity of infection (MOI) of 3. Cells were collected 48 h after infection by low-speed centrifugation at 2,000 x g. The cell pellet was washed with phosphate-buffered saline (PBS), pelleted by centrifugation at 2,000 x g, and then frozen and stored at -80 ^{o}C for later purification.

2.3.2 Purification of full-length and caspase-cleaved Panx1

To isolate membrane-localized Panx1, *Sf9* cell pellets were resuspended in low salt buffer A (50 mM HEPES, pH 7.5, 50 mM NaCl, 0.5 mM EDTA and protease inhibitor cocktails (Roche)) and lysed by Dounce homogenization (~30 strokes). Nucleic acids were digested by adding $MgCl_2$ to 2.5 mM and Benzonase (EMD Millipore) to ~12.5 units per 1 ml lysate, with gentle stirring at 4 ^{o}C for 20 min. Membranes were collected by ultracentrifugation at 100,000 x g and washed with stepwise Dounce homogenization in low salt buffer A and high

salt buffer B (50 mM HEPES, pH 7.5, 1 M NaCl, 0.5 mM EDTA and protease inhibitor cocktails) with ultracentrifugation at 100,000 x g between steps. Final Dounce homogenization was performed in buffer C (50 mM HEPES, pH 7.5 and 500 mM NaCl), followed by ultracentrifugation at 100,000 x g.

The membrane pellet was solubilized at 4 ^{o}C with 1% (w/v) n-tridecyl-β-D-maltopyranoside (TDM; Anatrace) in buffer D (50 mM HEPES, pH 7.5, 300 mM NaCl, 10 mM imidazole, 2.5% glycerol and protease inhibitor cocktails). Insoluble material was removed by ultracentrifugation at 100,000 x g, and the supernatant was incubated with ~1.0 ml of cobalt-charged TALON metal affinity resins (Clontech) at 4 °C for 1 h. The resin was packed in an Econo-column (Bio-Rad, 1.0 x 10 cm) and washed with 10 mM imidazole, and 25 mM imidazole (20 column volumes/wash), and eluted with 250 mM imidazole in buffer C containing 0.02% TDM. Imidazole was removed using a G-25 buffer exchange column (GE Healthcare), and the eluted Panx1 proteins were concentrated to 1-2 mg ml^{-1} using an Amicon ultracel-100 centrifugal filter unit (EMD Millipore). For generating C-terminally cleaved Panx1 proteins, purified full-length Panx1 was incubated overnight at 4 °C with recombinant, human caspase-3 (BD Biosciences) at a ratio of 1:500 (w/w). To improve contrast of negatively stained Panx1 particles, full-length and caspase-cleaved Panx1 were mixed with amphipol (A8-35, Anatrace) at a ratio of 1:3 (w/w) by gentle agitation for 4 h at 4 °C. TDM detergent was then removed by overnight incubation with Bio-Beads SM-2 (Bio-Rad) at 4 ^{o}C, and the Bio-Beads were subsequently removed using a

disposable polyprep column (Bio-Rad).

Aggregated materials were removed by ultracentrifugation at 150,000 x g, for further purification by size-exclusion chromatography (SEC) on a 7.8 x 300 mm SRT-C 300 column (Sepax Technologies) interfaced to an AKTA Purifier10 HPLC system (GE Healthcare), in buffer C (50 mM HEPES, pH 7.5 and 500 mM NaCl).

2.3.3 SDS-PAGE and Western immunoblot analysis

Panx1 purity was assessed by SDS-PAGE and Western immunoblot. For SDS-PAGE, 4-20% pre-cast acrylamide gradient Tris-glycine gel (Bio-Rad) was used. Gels were stained by Simply Blue (SimpleBlue Safe Stain, Novex). For Western immunoblot, SDS-PAGE gels were immediately transferred to nitrocellulose blotting membrane (GE Healthcare). Proteins on the nitrocellulose membrane were probed with the primary polyclonal anti-pentaHis antibodies (Qiagen). Donkey anti-mouse immunoglobulin G antisera coupled to IRDye 800 (LI-COR) was used to label the primary antibodies. Bands were imaged using an infrared imaging system (LI-COR Odyssey Imaging System).

2.3.4 Membrane localization assay

Sf9 insect cells were plated onto poly-L-lysine-coated coverslips within a well of 24-well Linbro tissue culture dishes, and infected at various M.O.I. with recombinant baculovirus encoding full-length human Panx1. The coverslips with adherent, infected cells were harvested 48 h post infection and fixed with paraformaldehyde. Immunolabeling was performed by the use of primary polyclonal antibodies directed against the Panx1 EL2 (aa247-265)[36] and a secondary antibody conjugated to the fluorescent dye Alexa-594. Coverslips were mounted onto slides and sealed with polish. Fluorescence images were recorded with a Zeiss LSM150 confocal microscope (housed in Dr. Brant Isakson's Laboratory, University of Virginia) and analyzed using IPLab software.

2.3.5 Fluorescent thermal stability assay (FTSA)

Thermal stability of Panx1 was characterized using a cysteine-reactive, coumarin-based fluorophore, CPM (N-(4-(7-diethylamino-4-methyl-3-coumarinyl) phenyl) maleimide[174]. The quantum yield increases upon temperature-induced protein unfolding when CPM binds to cysteine residues within the core of a protein. The CPM fluorescent dye (Invitrogen) in dimethylformamide was solubilized in the corresponding SEC buffers (Panx1 in amphipol A8-35: 50 mM HEPES, pH 7.5, 500 mM NaCl; Panx1 in TDM: 50 mM HEPES, pH 7.5, 500 mM NaCl, 0.01% TDM) to 13.3 µM and incubated with buffer on ice for 15 min. 10 µg

of Panx1 protein was then added to the buffer containing CPM fluorescent dye and incubated on ice for another 15 min. A temperature scan from 10-90 ^{o}C was performed using a FluoroMax-3 spectrofluorometer (Horiba Jobin-Yvon). The fluorescence-temperature profile was analyzed using non-linear regression of a Boltzmann sigmoidal equation (Origin 7.5 software, OriginLab), in which the melting temperature (T_m) was calculated from the inflection point of the resulting melting curve[174].

2.3.6 Differential filtration assay (DFA)

Dr. Michael Wiener's laboratory at the University of Virginia has developed a differential filtration assay (DFA)[170] for assessing the stability of a membrane protein by screening the protein across a panel of 94 detergents and subsequently testing for filtration through supports with high and low molecular weight cut-offs (MWCO). Panx1 was initially solubilized and purified in the detergent n-decyl-β-D-maltopyranoside (DM), and then bound to Talon Co^{+}-affinity resin (Clontech) followed by aliquots into 96 wells of a 0.2 micron filter plate, and washed with DM-containing buffer to remove unbound protein. Immobilized Panx1 protein was washed with buffer containing the new detergents (94 detergents for screening plus 2 controls of water and DM), and eluted with buffer at 250 mM imidazole containing the respective new detergents. The elution was applied to and passed through via centrifugation high (300 kDa) and low (100 kDa) MWCO filter plates to assess stability and relative size

information. Panx1 solubilized in a ‘good’ detergent (one that does not disrupt the proper oligomer or cause aggregation) should be able to be eluted through the high MWCO filter plate but not the low MWCO filter plate. The elutions from the plates were spotted onto nitrocellulose filters using a dot-blot apparatus. Eluted, filtered protein was imaged by immunodetection of the C-terminal 6xHis tag using the LI-COR Odyssey scanner to quantify the amount of protein within each dot. For full-length Panx1, the most promising detergents that did not disrupt the oligomers or cause aggregation would be ones that gave rise to strongly intense dots on the high MWCO plate and no signal from the same dots on the low MWCO plate. No or very faint signal at the same dot position on both plates would suggest that the respective detergent may cause aggregation, whereas observable signal at the same dot position on both plates would suggest that the respective detergent may disrupt the proper oligomers.

2.3.7 Matrix-assisted laser desorption/ionization mass spectrometry (MALDI-MS)

Human full-length and caspase-cleaved Panx1 at ~20 μM in SEC buffer (50 mM HEPES pH 7.5, 500 mM NaCl, 0.01% LMNG) were analyzed using a Matrix-assisted laser desorption/ionization mass spectrometry (MALDI-MS) in the Biomolecular Analysis Facility Core at the University of Virginia. The Panx1 sample was first mixed with an aromatic carboxylic acid matrix, spotted on a plate, and then loaded into the mass spectrometer.

2.3.8 Negative-stain electron microscopy

An aliquot (3.5 µl) of purified Panx1 (full-length or caspase-cleaved) at 0.01-0.02 mg ml^{-1} were applied to a glow-discharged, carbon-coated, 300-mesh, copper grid (Electron Microscopy Sciences), and stained with 2% uranyl acetate as described[175]. Low-dose EM was performed using a Tecnai F20 electron microscope (FEI), operating at 120 kV. Images were recorded at a nominal magnification of ×62,000 and a defocus of -0.75 µm ~ -0.9 µm using a 4K×4K charge-coupled device (CCD) camera (UltraScan 4000, Gatan), corresponding to a pixel size of 1.82 Å on the specimen.

2.3.9 Single-particle image analysis

The EMAN2 software suite[173] was used for single-particle image analysis of negatively stained Panx1 particles. A total of ~6,000 full-length or caspase-cleaved Panx1 particles from ~150 micrographs were semi-automatically selected and extracted within boxes of 196 pixels × 196 pixels using the 'Swarm' tool in the e2boxer.py program of EMAN2. The contrast transfer function (CTF) was estimated and corrected by the e2ctf.py program of EMAN2. Particle images were normalized and then high-pass (100 Å) and low-pass (10 Å) filtered and centered. The e2refine2d.py program was used to perform 2D classification by iterative, multivariate statistical analysis (MSA). Six-fold symmetry was applied to the 2D class averages using the e2proc2d.py program.

2.3.10 Electrophysiology *(From Dr. Yu-Hsin Chiu, University of Virginia)*

All voltage-clamp recordings were carried out at room temperature; when recording from transiently transfected HEK293T cells, a pan-caspase inhibitor, Q-VD-OPh (Q-VD, 20 uM), was used during and after transfection to prevent inadvertent C-terminal cleavage of Panx1 by endogenously activated caspases. Micropipettes were pulled from thin-walled borosilicate glass capillaries (Harvard Apparatus) by using P-97 or P-87 puller (Sutter Instrument), and coated with Sylgard 184 silicone elastomer (Dow Corning Corporation).

Inside-out and cell-attached patch recordings were obtained using micropipettes with resistance of 7-10 MΩ and an Axopatch 200B amplifier controlled by pCLAMP10 software (Molecular Devices). Data were filtered to 5 kHz using an 8-pole low-pass Bessel filter (LPF-8, Warner Instruments) and digitized at a sampling rate of 20 kHz using a Digidata 1322A digitizer (Molecular Devices). Bath solution was composed of 140 mM NaCl, 3 mM KCl, 2 mM $MgCl_2$, 2 mM $CaCl_2$, 10 mM HEPES and 10 mM glucose (pH 7.3). Pipettes were filled with the bath solution as described, and ≥10 GΩ seals were obtained in the bath solution. Patches were held at 0 mV before stepping to + 50 to + 80mV and - 80 to - 50 mV (Δ10 mV, > 5 s) for steady-state channel recordings; we did not observe a change in conductance or activity over time at test potentials. For inside-out patch recording, immediately after excising membrane patches, the bath solution was exchanged for an inside-out solution composed of 150 mM CsCl, 5 mM EGTA, 10 mM HEPES and 1 mM $MgCl_2$ (pH 7.3), and only those

patches that were silent initially after excision were used (that is, those with no endogenous channel activity). Purified caspase-3 was applied locally near the patch to a final concentration of 1-2 μg ml $^{-1}$. Single-channel activity was analysed using pCLAMP10; channel data were filtered to 2 kHz using a 8-pole low-pass Bessel filter for analyses of open probability and open time distribution, and filtered to 1 kHz for presentation except otherwise mentioned.

Chapter 3

CryoEM Structural Analysis of Pannexin1 Channels

3.1 Introduction

Pannexins (Panxs) were discovered in 2000 on the basis of their limited sequence homology to innexins (Inxs), the invertebrate gap junction channels (GJCs), and comprise a novel protein family in the mammalian genome[12]. Despite lack of sequence similarity to connexins (Cxs), the vertebrate GJCs, Panxs share a common tetra-spanning membrane topology with Cxs and Inxs, as well as recently identified calcium homeostasis modulator 1 (CALHM1) and leucine-rich repeat-containing 8 (LRRC8) protein channels[13,16,134,138]. Each protein subunit contains four transmembrane (TM) domains that are connected by two extracellular loops (EL) and one cytoplasmic loop (CL), and cytoplasmic amino (NT) and carboxyl (CT) termini. Cxs and Inxs can assemble as single membrane hemichannels (HCs) and can also dock two HCs from adjacent cells end to end to form intercellular GJCs. In contrast, Panxs only form single membrane channels that transport molecules between the cytosolic and extracellular space[21-23].

Panx1, one of the three mammalian Panx family members (Panx1-3), is a ubiquitously expressed, oligomeric plasma membrane channel[13]. Panx1

channels can be activated by various stimuli including mechanical stress[24,49], membrane depolarization[19,49,60], increased extracellular potassium[58,61-65], increased intracellular calcium[34,66], receptor-mediated signaling pathways[34,55,68,69,71,72,75], and caspase cleavage of the distal C-terminus[50,77-79]. Upon activation, Panx1 channels allow permeation of molecules such as nucleotides (ATP and UTP) and fluorescent dyes (cationic To-Pro and anionic Lucifer Yellow) across the plasma membrane[28,49,50]. Panx1-dependent ATP release plays an important role in diverse physiological and pathological processes, including blood pressure regulation[24,68,69], apoptotic cell clearance[50,119], inflammation[55,120], neurological disorders[56,63,72,126,127], cardiac fibrosis[130] and cancer aggressiveness and metastasis[131,132].

Despite extensive knowledge about the physiology of Panx1 channels, there is much to learn about their structure and molecular basis for channel regulation. Structures of Cx and Inx GJCs have been studied for years, in which high-resolution structures of Cx26[44,45] and INX-6[47] have been determined by X-ray crystallography and single-particle electron cryomicroscopy (cryoEM), respectively. Very recently, the high-resolution structure of LRRC8A (SWELL1), a volume-regulated anion channel (VRAC), which shares the same tetra-spanning membrane topology and a common ancestor with Panx1[134], has been determined by a combination of X-ray crystallography and single-particle cryoEM[139]. Nonetheless, knowledge of the three-dimensional (3D) structure of Panx1 channels is very limited since neither high-resolution images nor

purification of Panx1 channels have been reported. Extensive structural studies on Cx GJCs have led to a common view that a dodecameric Cx GJC is formed by docking of two hexameric HCs[43-45,150,151]. Since Panxs are considered to be analogous to Cxs, in which they share a common tetra-spanning membrane topology and form similar large-pore channel[13,19,24,30,32], it was assumed that Panx1 subunits form a hexameric channel. Previous stoichiometric studies of Panx1, using electron microscopy (EM), chemical cross-linking and single-molecule photobleaching, also suggested that Panx1 was a hexamer[30,41,48]. Despite the estimation from low-resolution EM images, however, there is no direct structural evidence demonstrating the oligomeric state of Panx1 channels.

Here, we performed single-particle cryoEM analysis of the C-terminally truncated frog Panx1 channel reconstituted in lipid nanodiscs, and derived a 3D reconstruction at 7 Å resolution, allowing us to accurately determine the oligomeric state of Panx1 channel, putatively assign the transmembrane helices, and provide insights into the similarities and differences in the structures between Panx1 and other tetra-spanning membrane channels such as Cxs, Inxs and LRRC8A (SWELL1) channels.

3.2 Results and discussion

3.2.1 Optimize Panx1 protein samples for single-particle cryoEM analysis

The very initial Panx1 protein sample we tried for single-particle cryoEM analysis was the caspase-cleaved Panx1 as mentioned in Chapter 2. Full-length, His-tagged, human Panx1 was expressed in *Sf9* insect cells, extracted and purified in the detergent n-tridecyl-β-D-maltopyranoside (TDM), following C-terminal cleavage by caspase-3 to remove the potentially disordered region, and amphipol exchange to increase the contrast of frozen-hydrated Panx1 particles. Caspase-cleaved Panx1 in amphipols was then subjected to purification by size exclusion chromatography (SEC) for cryoEM sample preparation. It was showed that caspase-cleaved Panx1 in amphipols forms thermally stable, homogenous and monodisperse oligomers (**Figure 2.4**, **2.5**). About 1500 electron micrographs of frozen-hydrated, caspase-cleaved Panx1 were recorded on a Falcon II direct detector of a Titan Krios electron microscope at the University of Virginia Molecular Electron Microscopy Core (UVA-MEMC) (**Figure 3.1a**). Although individual particles were readily visualized on the cryomicrograph (**Figure 3.1a,b**), two-dimensional (2D) class averages derived from image processing using the RELION software package[176] did not reveal secondary structural features such as α-helices (**Figure 3.1c**), which is a critical step to determine whether a high-resolution structure can be obtained. Several factors may account for this. Major obstacles for achieving a high-resolution structure by single-particle cryoEM are the compositional and conformational heterogeneity of the protein sample[177]. In

addition to sample heterogeneity, the ice thickness is also crucial. Moreover, use of a Falcon II direct detector may have limited our ability to record high-resolution images of Panx1. Rosenthal and Henderson have shown that it is significantly more difficult to determine particle orientations for 3D reconstructions when the macromolecular complex has a molecular weights less than ~600 kDa [178]. In fact, a caspase-cleaved Panx1 oligomer is predicted to have a mass of 250-300 kDa. Since determination of the particle Euler angles is primarily determined by the low-resolution frequencies in an image (0-0.4 Nyquist frequency), it is crucial for small molecular weight particles to use a detector with a higher detective quantum efficiency (DQE) in the low-resolution range. The Gatan K2 Summit camera has a DQE that is about 50% higher than that of the Falcon II camera in the low-resolution frequency domain, which allows us to determine more accurate particle orientations.

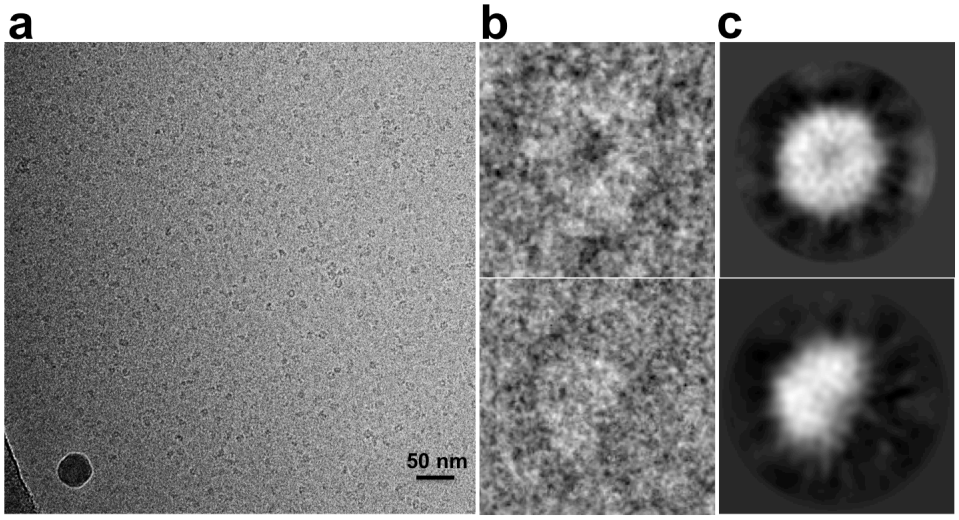

Figure 3.1. Single-particle cryoEM analysis of caspase-cleaved human Panx1 channels. (a) Representative electron micrograph of frozen-hydrated, caspase-cleaved human Panx1 particles in amphipols. Individual particles are readily visualized at a defocus of -2.5 µm. **(b)** Selected particles with top (top) and putative side (bottom) views and **(c)** corresponding class averages from 1,357 particles for the top view (top) and 1,889 particles for the putative side view (bottom), respectively.

In an attempt to reduce sample heterogeneity, we examined numerous expression and purification conditions, including Panx1 constructs (e.g. species, mutations, fusion proteins, protease cleavage sites and affinity tags), expression systems (e.g. insect and mammalian cells), and purification methods (e.g. detergents, buffers, proteases, inhibitors, chemical cross-linking and deglycosylation) (**Table 3.1**). We first performed cross-linking of full-length human Panx1 using glutaraldehyde (**Supplementary Figure A1.1**), or treatment with inhibitors such as carbenoxolone, spironolactone or trovafloxacin (**Supplementary Figure A1.2**). Although cross-linked Panx1 showed reduced compositional heterogeneity by SEC, there was no apparent improvement in 2D class averages of negatively stained Panx1 particles (**Supplementary Figure A1.1**). Of note, unlike Cx and Inx GJCs that are composed of two HCs, Panx1 single membrane channels are more difficult to be recognized from the background noise due to their fewer features in side views. To deal with this problem, we generated Panx1 fusion proteins with either T4 lysozyme (T4L, 19 kDa), or enhanced green fluorescent protein (EGFP, 27 kDa) (**Table 3.1**). T4L is classically used as a fusion protein in structural studies of G protein-coupled receptors (GPCRs)[179-181]. The fluorescence from EGFP is appealing as a sensor to detect expression, homogeneity and the oligomeric state by fluorescent size-exclusion chromatography (FSEC)[182]. Moreover, the fusion proteins also add mass to aid particle-picking in the micrographs and determination of orientation angles for 3D reconstruction. We expressed Panx1 fusion proteins in *Sf9* insect cells, extracted and purified these proteins using the detergent TDM, which were

then exchanged into amphipols for examination by single-particle negative-stain EM. Class averages (top view) of the negatively-stained Panx1 fusion proteins showed increasing channel diameters with increasing molecular weight of each protein (hPanx1 ~135 Å; hPanx1-T4L ~155 Å; hPanx1-EGFP ~160 Å); however, none of them displayed improved structural features such as delineation of individual protein subunits (**Supplementary Figure A1.3**). Accordingly, class averages of these frozen-hydrated Panx1 fusion proteins did not reveal any α-helical structure (**Supplementary Figure A1.3**). Thus, these fusion proteins were not suitable for single-particle cryoEM analysis.

Constructs	Expression Systems	Purification		
		Detergents	Treatments	SEC columns
Human PANX1(FL)-6xHis	**Insect (sf9)**	TDM-Amphipols	Caspase-3 TEV protease Thrombin protease (Protease)	SRTC 300
Human PANX1(FL)-TEV@Casp3-6xHis				
Human PANX1(FL)-T4L-6xHis				
Human PANX1(FL)-Flag-TVMV-eGFP-6xHis				Superdex 200
Human PANX1(N255Q)-6xHis	Mammalian (HEK 293S)	**DDM/CHS-Amphipols**		
Mouse PANX1(FL)-6xHis				
Mouse PANX1(FL)-T4L-6xHis			Carbenoxolone Spironolactone Trovafloxacin (Inhibitor)	**Superose 6**
Human PANX1(FL)-TEV-Strep				
Human PANX1(1-381)-TEV-Strep				
Human PANX1(1-359)-TEV-Strep		**DDM/CHS-Nanodiscs**		
Human PANX1(1-355)-TEV-Strep				
Human PANX1(1-323)-TEV-Strep				
Human PANX1(FL)-Thrombin-eGFP-Strep			Glutaraldehyde (X-link)	
Human PANX1(1-381)-Thrombin-eGFP-Strep				
Human PANX1(1-355)-Thrombin-eGFP-Strep				
Human PANX1(FL)-Thrombin-Strep			PNGase F (Deglycosylation)	
Human PANX1(1-381)-Thrombin-Strep				
Human PANX1(1-355)-Thrombin-Strep				
Frog PANX1(FL)-Thrombin-eGFP-Strep				
Frog PANX1(1-357)-Thrombin-eGFP-Strep			**Ca^{2+} (Stabilization)**	
Frog PANX1(FL)-Thrombin-Strep				
Frog PANX1(1-357)-Thrombin-Strep				

Table 3.1. Screened conditions for optimization of Panx1 samples. Bold, optimal conditions used for single-particle cryoEM analysis.

Meanwhile, we found that the detergent TDM self aggregated if the buffer containing TDM was maintained at 4 ^{o}C for more than 1 hour, which could affect the stability of Panx1 proteins solubilized in detergent micelles. It has been shown that maltopyranoside/cholesteryl hemisuccinate (DDM/CHS) can significantly improve the SEC performance of membrane proteins[183]. The detergent TDM was therefore exchanged to DDM/CHS for solubilization and purification.

We also found that Panx1 easily aggregated when imidazole was removed during purification, probably due to the C-terminal His tags. As mentioned in Chapter 1, the C-terminus of Panx1 is most variable[37] and potentially disordered. Therefore, on the basis of secondary structure prediction and protein sequence analysis, we generated several C-terminally truncated human Panx1 constructs, with (or without) EGFP, and a Strep tag replacing the original His tag at the C-terminal truncation end. In addition, we also introduced a protease cleavage site (TEV or Thrombin) preceding the (EGFP-) Strep tag, which enabled removal of the tags during purification if their presence increased heterogeneity (**Table 3.1**). Interestingly, we observed that the SEC performance of the C-terminally truncated Panx1 with a Thrombin protease site was better than the construct with a TEV protease site. Dr. Toshi Kawate's laboratory screened several Panx1 species using FSEC, and discovered that the performance of frog Panx1 was mostly stable and homogenous. Thus, we also generated a C-terminally truncated frog Panx1 (frPanx1 (1-357)) construct, with a

thrombin cleavage site and a Strep tag at the C-terminal truncation end. We picked Lys357 as the truncation site because regions after this residue are least conserved from sequence alignment of human, mouse, and frog Panx1 (**Figure 3.2**). Consequently, the C-terminally truncated frog Panx1 at reside 357, with a Thrombin cleavage site and Strep tag, was used for subsequent single-particle cryoEM analysis. Unless otherwise stated, this construct is referred to Panx1 in the following discussion.

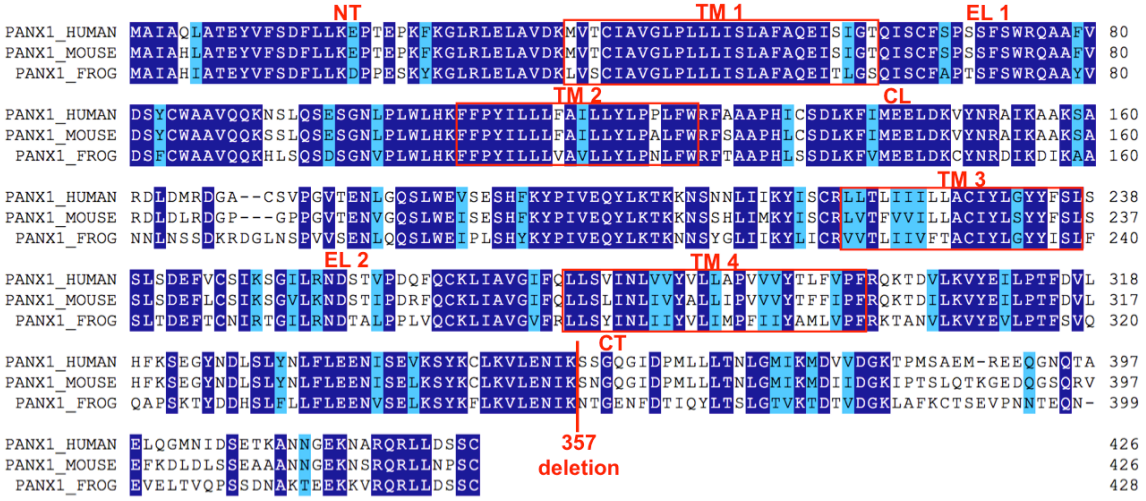

Figure 3.2. Sequence alignment of human, mouse and frog Panx1. Selected Panx1 isoforms aligned with their amino acid sequence by ClustalW[184]. Identical residues and similar residues are coloured dark blue and light blue, respectively, using the Multiple Align Show web-based program. Truncation site at Lys357 is indicated. TM1-TM4, transmembrane helices; EL1 and EL2, extracellular loops; CL, cytoplasmic loop; NT and CT, amino and carboxyl termini. Note the lack of sequence conservation beyond residue 357.

3.2.2 Panx1 forms stable and homogeneous oligomers in detergent micelles

Strep-tagged, C-terminally truncated frog Panx1 (frPanx1 (1-357)) was expressed in *Sf9* insect cells, extracted in the detergent DDM/CHS and purified using strep-tactin affinity chromatography. Coomassie blue stained SDS-PAGE and Western immunoblot analysis with anti-Strep antibodies showed that the Panx1 monomer band migrated at ~37 kDa, which is smaller than the calculated value (43 kDa) from amino sequence (**Figure 3.3a**). This might be due to the charge distribution and/ or globular shape of Panx1 protein. It has been shown that rat Panx1 expressed in HEK293T cells can be N-glycosylated at Asn254, resulting in three protein bands that represent the non-glycosylated core protein (lower band), the high mannose-type glycoprotein (intermediate band), and the fully processed mature-type glycoprotein (upper band), respectively[30]. However, we observed only two Panx1 protein bands by SDS-PAGE (**Figure 3.3a,d**). As in previous studies[30], the top band of Panx1 was sensitive to PNGaseF (**Figure 3.3d**), indicating that Panx1 is glycosylated in insect cells by a different mechanism compared to mammalian cells. This glycosylation was also confirmed by MALDI-MS of Panx1 proteins with or without treatment of PNGaseF, in which the molecular weight of deglycosylated Panx1 (42.878 kDa) agrees with the calculated value (43.015 kDa) from amino sequence, while the larger molecular weight of the native Panx1 (44.403 kDa) could be due to glycosylation in insect cells (**Figure 3.3e**).

It was proposed that Panx1 subunits form a hexamer by examination of DSP cross-linked rat Panx1[30]. Here, we used glutaradehyde to cross-link Panx1 in the detergent DDM/CHS, and observed a protein band at ~250 kDa (**Figure 3.3a**). However, it is difficult to determine an accurate oligomeric number just by the estimated molecular weight due to the low resolution of this gel system and possibly altered charged distribution and globular shape of the protein after cross-linking. We then performed size exclusion chromatography with multi-angle light scattering (SEC-MALS) analysis of Panx1 purified in the detergent DDM (**Figure 3.3f**), which enables us to investigate the stoichiometry of Panx1 by simultaneously measuring the protein and detergent components in a protein-detergent complex using a combination of SEC and light scattering with ultraviolet (UV) and refractive index (RI) detectors[185]. SEC-MALS yielded an averaged molar mass of Panx1 at 320.1 kDa, which is between the calculated heptamer (43.015 kDa x 7 = 301.105 kDa) and octamer (43.015 kDa x 8 = 344.120 kDa) from the amino sequence (**Figure 3.3f**). Due to the 5% systematic error of SEC-MALS (~16 kDa), it is difficult to determine whether Panx1 forms a heptamer or octamer. Nevertheless, we conclude that frog Panx1 does not assemble as a hexamer.

Analytical SEC of non cross-linked Panx1 showed a single UV 280 nm absorbance peak with minimal aggregation and same elution volume as cross-linked Panx1, indicating that Panx1 monomers form a stable oligomer (**Figure 3.3b**). The thermal stability of Panx1 was assessed by a fluorescence-based

thermal stability assay (FTSA), in which the quantum yield increases upon temperature-induced protein unfolding when cysteine residues embedded within the protein interior become accessible for binding to a fluorophore[174]. It was showed that Panx1 started to unfold around 50 ^{o}C, and the estimated melting temperature (T_m) was 57 ^{o}C, suggesting that Panx1 is thermally stable in the detergent DDM/CHS (**Figure 3.3c**). Thus, glycosylated, C-terminally truncated frog Panx1 forms stable and homogenous oligomers (possibly heptamer or octamer) in detergent micelles, which are suitable for single-particle cryoEM.

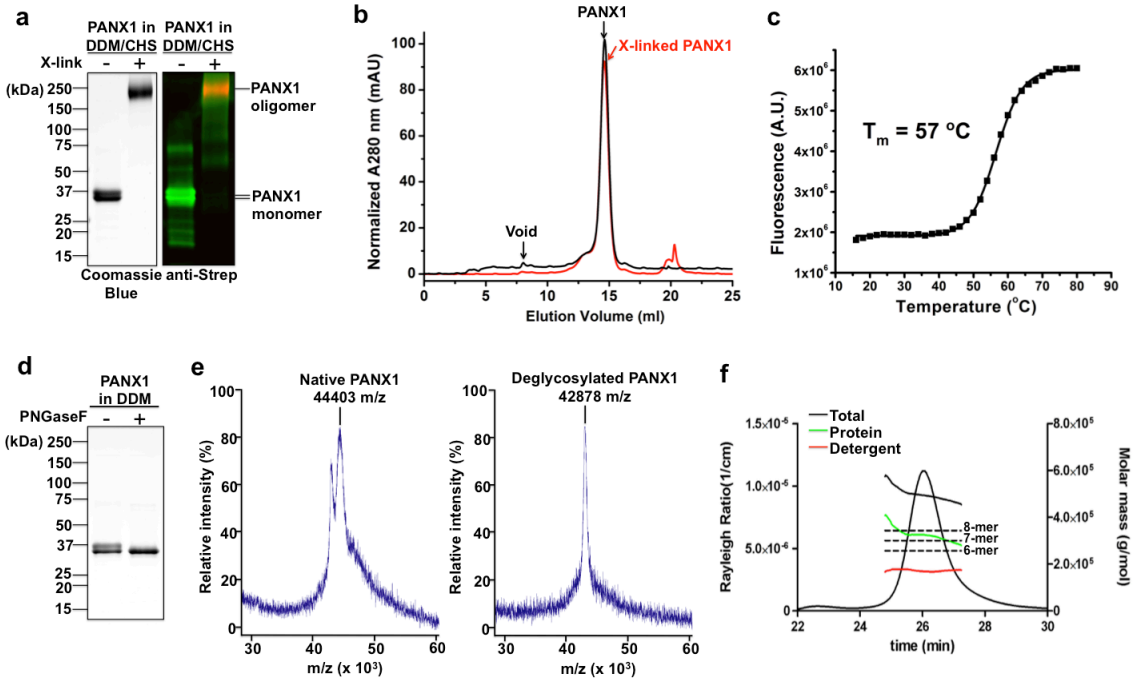

Figure 3.3. Panx1 forms stable and homogeneous oligomers in detergent micelles. **(a)** Coomassie Blue stained SDS-PAGE and Western immunoblot probed with anti-Strep antibodies showed monomeric Panx1, and oligomeric Panx1 cross-linked by 0.1% glutaradehyde. **(b)** SEC showed both native (black) and cross-linked (red) Panx1 were homogenous, with minimal aggregation (void) and same elution volume. **(c)** FTSA showed native Panx1 was thermally stable, with melting temperature (T_m) of 57 ^{o}C. **(d)** Coomassie Blue stained SDS-PAGE showed Panx1 was deglycosylated with treatment of PNGaseF. **(e)** MALDI-MS showed mass-to-charge (m/z) ratio of native (44.403 kDa) and deglycosylated (42.878 kDa) Panx1 by PNGaseF. **(f)** SEC-MALS showed oligomeric number of Panx1 was seven or eight. Note: (a-c) Panx1 purified in DDM/CHS; (d-f) Panx1 purified in DDM. (SEC-MALS experiment was performed by Dr. Bill McIntire, University of Virginia)

3.2.3 Panx1 subunits form a heptameric channel

Since detergent-solubilized, frozen-hydrated Panx1 on cryomicrographs demonstrated low contrast due to high background noise contributed by free detergent micelles, purified Panx1 in the detergent DDM/CHS was exchanged to amphipols as described in Chapter 2[171,172,186,187]. Two glycosylated Panx1 protein bands at ~37 kDa were observed by Coomassie blue stained SDS-PAGE and Western immunoblot analysis using anti-Strep antibodies, which are similar to the purified Panx1 in the detergent DDM/CHS (**Figure 3.4a**). Further purification by SEC to remove extraneous amphipols showed that C-terminally truncated frog Panx1 was much more homogenous, with almost no aggregation indicated by the minimal void peak (**Figure 3.4b**), in comparison to the C-terminally cleaved human Panx1 (**Figure 2.4b**). The Panx1 protein peak fractions were combined and subjected to negative-stain EM analysis. Electron micrographs of negatively-stained Panx1 in amphipols showed homogeneous and monodisperse particles (**Figure 3.4c**). EMAN2 software[173] was used to generate 2D class averages. Two representative class averages (with no symmetry enforced) showed a doughnut-like appearance with a central pore (**Figure 3.4d**), similar to caspase-cleaved human Panx1 channels (**Figure 2.5b**). Surprisingly, the class averages showed that seven subunits form the channel, clarifying the uncertain results of chemical cross-linking, SEC and SEC-MALS (**Figure 3.3 a**,**b**,**f**). Over the last ~15 years, Panx1 has been considered as a hexameric channel by analogy to Cx GJCs[13,19,24,30,32], and previous studies estimated by EM, chemical cross-linking and single-molecule photobleaching[30,41,48]. Our compelling EM analysis shows

for the first time that Panx1 subunits form a heptameric channel. Although all reported structures of Cx HCs are hexameric[43-45,151], the recent cryoEM structure of the octameric Inx-6 HC[47] indicates that the oligomeric state of gap junction protein families may vary.

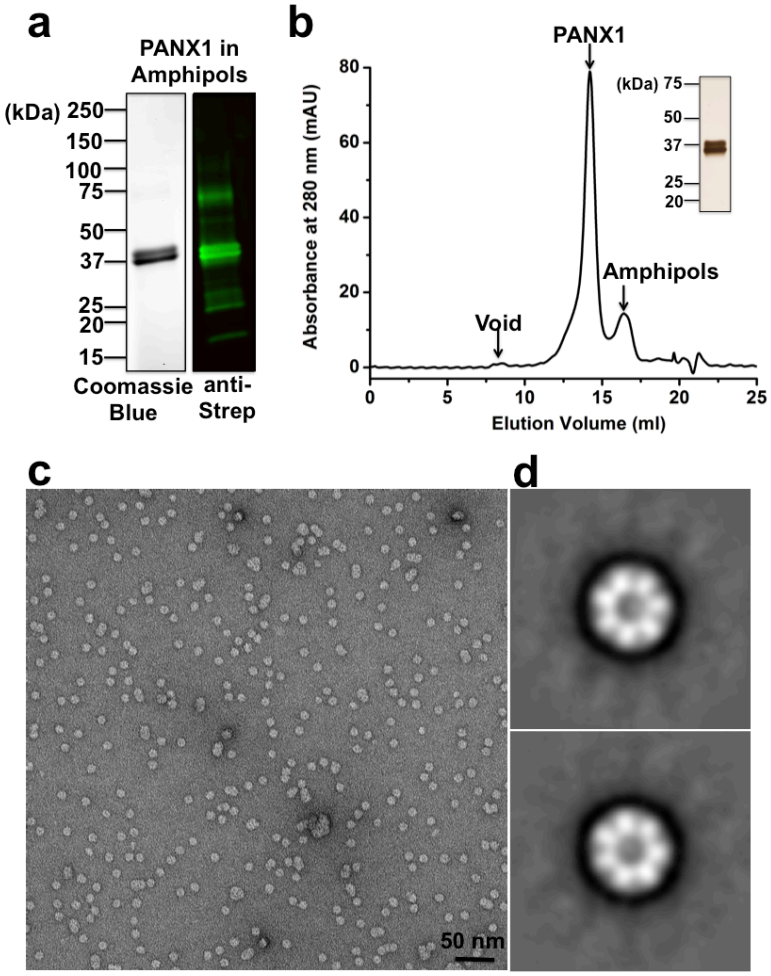

Figure 3.4. Characterization of Panx1 in amphipols revealed a heptameric channel. **(a)** Coomassie Blue stained SDS-PAGE and Western immunoblot probed with anti-Strep antibodies showed monomeric Panx1 in amphipols. **(b)** SEC showed Panx1 was homogenous, with minimal aggregation (Void peak) in amphipols. Panx1 protein, amphipol and void peaks are indicated. Inset, silver stained SDS-PAGE of SEC fractions collected from Panx1 protein peak. **(c)** Electron micrograph of negatively stained Panx1 in amphipols. Scale bar, 50 nm. **(d)** Representative 2D class averages of negatively stained Panx1 particles from (c), with 1649 (top) or 1903 (bottom) particles. The particle box dimension is 357 Å.

3.2.4 Calcium strikingly improved the stability and homogeneity of Panx1

We found that the stability and homogeneity of Panx1 were strikingly improved by inclusion of calcium during purification. Panx1 expressed in *Sf9* insect cells was extracted and purified in the detergent DDM/CHS with 3 mM $CaCl_2$ added to the buffer, and then exchanged to amphipols following SEC purification and single-particle negative-stain EM analysis. In the presence of Ca^{2+}, Panx1 was much more homogenous, in contrast to an obvious 'shoulder peak' (indication of sample heterogeneity) observed by SEC of Panx1 without Ca^{2+} (**Figure 3.5a,b**). Negative-stain EM showed that Panx1 plus Ca^{2+} particles were more monodisperse, with less aggregation (**Figure 3.5c,e**). Intriguingly, seven subunits were only resolved from class averages of negatively-stained Panx1 in the presence of Ca^{2+} (**Figure 3.5d,f**).

The mechanism for calcium stabilization of Panx1 channels is unclear. The Ca^{2+} -binding site of Cx26 has been identified from Ca^{2+}-bound X-ray crystal structure, in which the Ca^{2+} is coordinated by Glu47 and Gly45 in one subunit, and Glu45 in the adjacent subunit[45]. It has also been shown that Panx1 can be activated by increased intracellular calcium[34], or form Ca^{2+}-permeable channels in the ER[188]. Nonetheless, determination of the Ca^{2+}-binding site awaits a high-resolution structure.

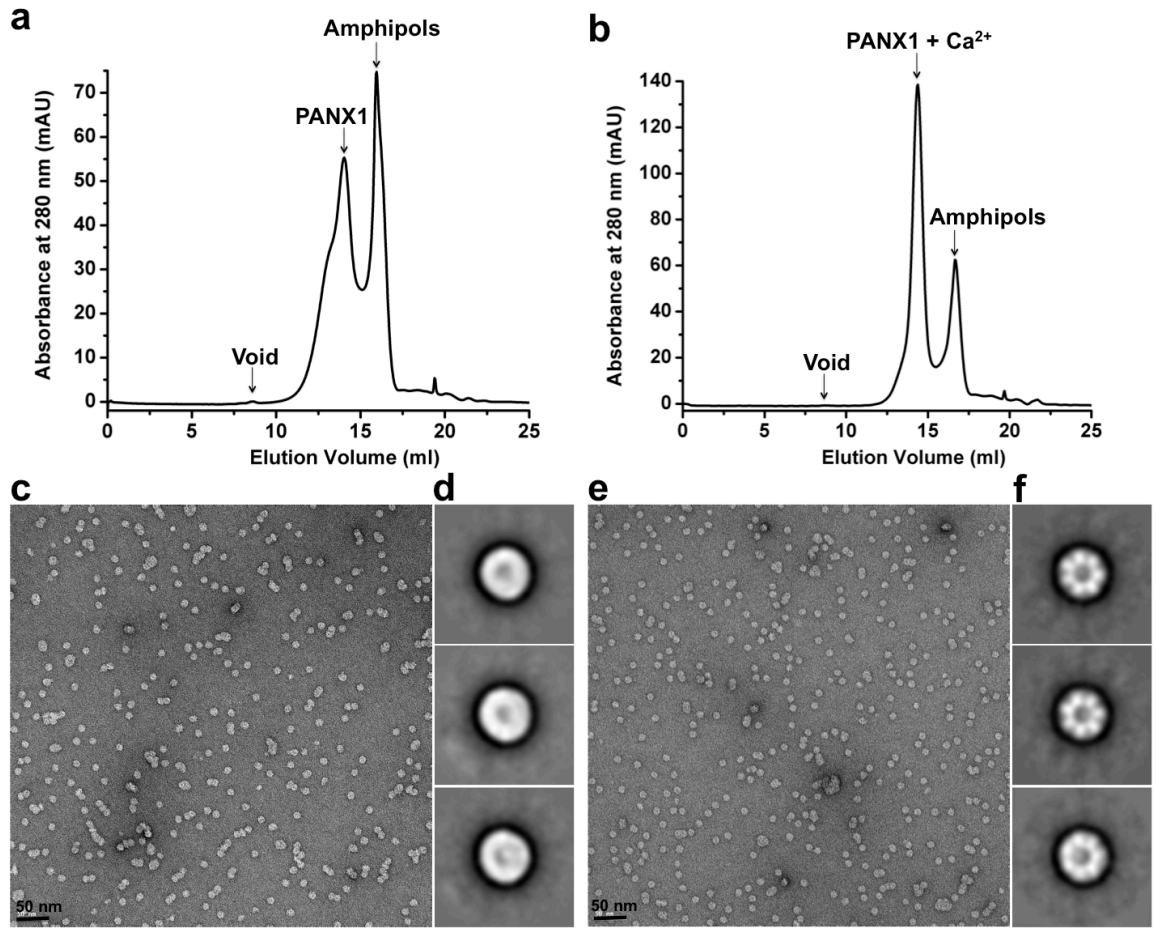

Figure 3.5. Calcium strikingly improved performance of Panx1 particles, characterized by SEC and single-particle negative-stain EM. (a-b) SEC showed Panx1 in the presence of Ca^{2+} (b) was more homogenous than Panx1 in the absence of Ca^{2+} (a). Note the left-sided 'shoulder' in the Panx1 peak in the absence of Ca^{2+} indicates heterogeneity (a). Panx1 protein, amphipol and void peaks are indicated. **(c,e)** Electron micrographs of negatively stained Panx1 without Ca^{2+} (c) and with Ca^{2+} (e). Scale bar, 50 nm. **(d,f)** Representative 2D class averages of negatively stained Panx1 without Ca^{2+} (d) and with Ca^{2+} (f). The particle box dimension is 357 Å.

3.2.5 Preferred orientation of Panx1 particles in amphipols precluded 3D reconstruction by single-particle cryoEM

In addition to optimizing the construct and purification conditions of Panx1, we also optimized the freezing conditions, including EM grid type, temperature, humidity, blotting force and blotting time, in order to obtain an ideal ice thickness for cryoEM data acquisition. Moreover, since the K2 direct detector determines more accurate particle orientations for relatively small molecular weight proteins compared to the Falcon II detector, we first collected ~1000 cryomicrographs of Panx1 in amphipols, at the National Center for Macromolecular Imaging (NCMI) at Baylor College of Medicine, using a JEOL3200 electron microscope equipped with a Gatan K2 direct detector. Individual particles were readily observed on the cryomicrographs, with good distribution and contrast, indicating that the ice thickness was optimal (**Figure 3.6a**). 2D class averages of the top view showed that Panx1 forms a ring-shaped heptamer, which displayed circular densities consistent with end-on views of α-helices (**Figure 3.6b**); however, the side view class average did not reveal any secondary structural features (**Figure 3.6b**), indicating a top-view preferred orientation for Panx1 in amphipols, which precluded determination of a 3D reconstruction.

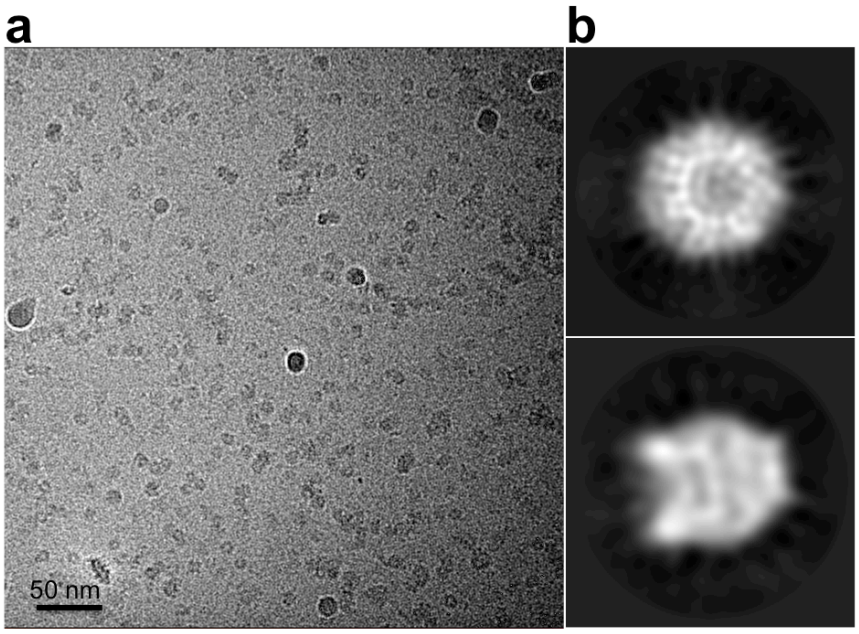

Figure 3.6. Single-particle cryoEM of Panx1 channels in amphipols showed preferred orientations. (a) Representative electron micrograph of frozen-hydrated Panx1 in amphipols. **(b)** Class averages from 3,318 particles for the top view (top) and 1,762 particles for the side view (bottom), respectively.

3.2.6 Lipid nanodisc-embedded Panx1 channels showed different particle orientations

To solve the problem of top-view, preferred orientation in amphipols, we reconstituted Panx1 into lipid nanodiscs assembled from soybean polar lipids and the Membrane Scaffold Protein 2N2 (MSP2N2). Since the diameters of hexameric Cx26[44] and octameric Inx-6[47] channels are 92 Å and 110 Å, respectively, the diameter of heptameric Panx1 is mostly likely between 90 Å and

110 Å. We selected MSP2N2 because it forms nanodiscs of 150-165 Å in diameter, which should be sufficient to accommodate Panx1 without imposing spatial constraint. Specifically, the Strep-tagged, C-terminally truncated frog Panx1 was expressed in *Sf9* insect cells, extracted and purified in the detergent DDM/CHS, and then reconstituted into lipid nanodiscs at a molar ratio of 1 : 1.25 : 125 (Panx1 : MSP2N2 : lipids), following SEC purification for single-particle negative-stain EM and cryoEM analyses. Glutaradehyde cross-linked Panx1 was also successfully reconstituted into lipid nanodiscs. Two glycosylated Panx1 protein bands at ~37 kDa were observed by both Coomassie blue stained SDS-PAGE and Western blot analysis using anti-Strep antibodies, which are similar to the results in DDM/CHS and amphipols (**Figure 3.7a**). Interestingly, the MSP2N2 protein band was obviously visible in cross-linked Panx1 nanodisc because Panx1 and MSP2N2 have a similar molecular mass (~43 kDa) (**Figure 3.7a,b**). Panx1 in lipid nanodiscs is stable and homogenous as revealed by SEC (**Figure 3.7b**). Negative-stain EM showed monodisperse Panx1 particles with different orientations, including characteristic side views (**Figure 3.7c**). Top view 2D class averages of Panx1-nanodisc particles revealed the heptameric arrangement of the channels. Side view 2D class averages showed a band-like density contributed by the lipid bilayer and scaffold protein (**Figure 3.7d**). 2D class averages of cross-linked Panx1-nanodisc particles also showed different orientations, with slightly improved definition of the extracellular and cytoplasmic protein densities (**Figure 3.7e**). Note that the forthcoming single-particle cryoEM analysis focused on Panx1 in lipid nanodiscs without cross-linking.

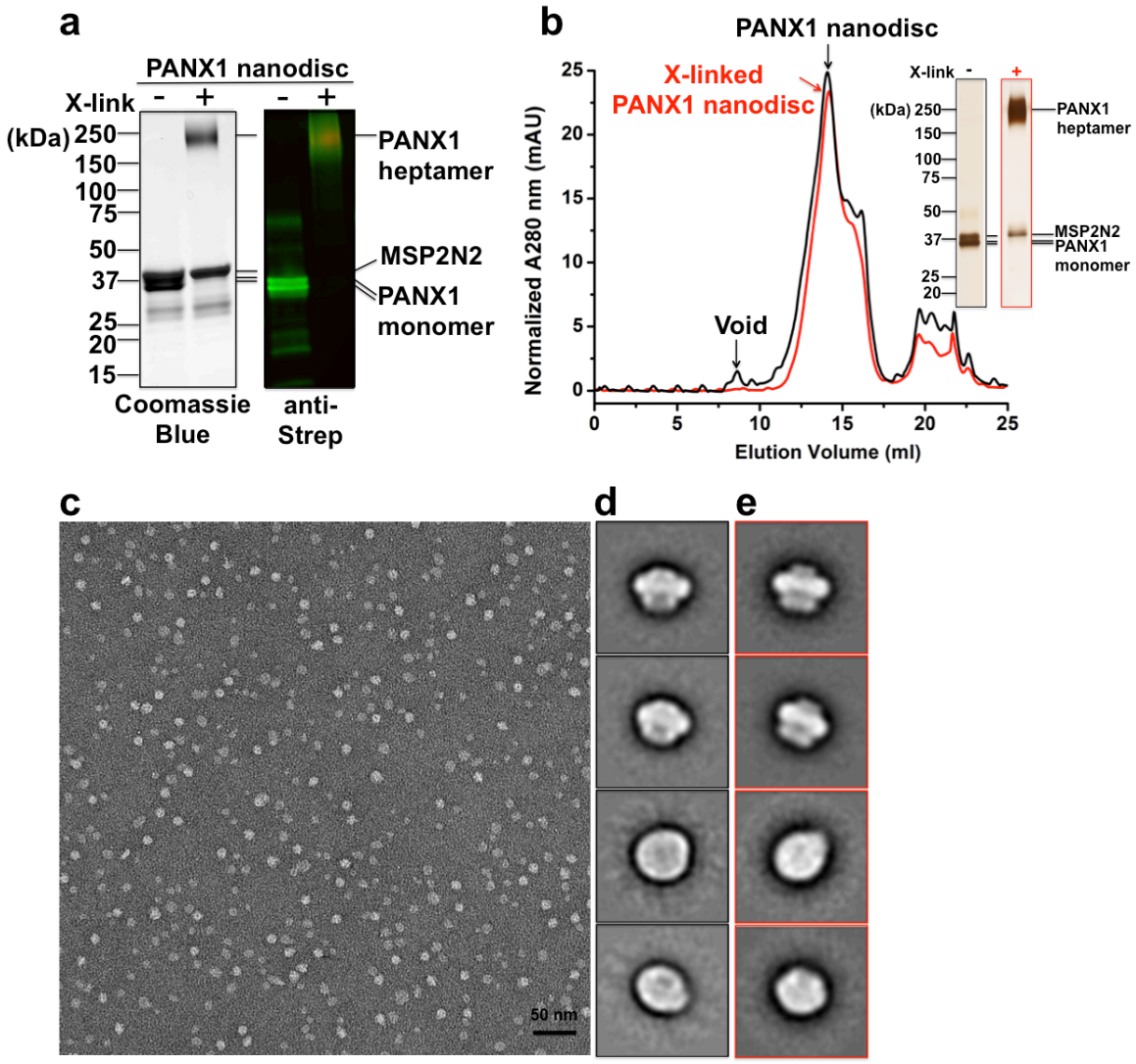

Figure 3.7. Characterization of Panx1 reconstituted in lipid nanodiscs revealed different particle orientations. (a) Coomassie Blue stained SDS-PAGE and Western immunoblot probed with anti-Strep antibodies showed monomeric and cross-linked Panx1 in lipid nanodiscs. **(b)** SEC showed both native (black) and cross-linked (red) Panx1 in lipid nanodiscs were homogenous, with minimal aggregation (void peak) and same elution volume. Panx1-nanodisc and void peaks are indicated. Inset, silver stained SDS-PAGE of SEC fractions collected from lipid nanodisc embedded- Panx1, or cross-linked Panx1 peaks. **(c)** Electron micrograph of negatively-stained Panx1 in lipid nanodiscs. Scale bar, 50 nm. **(d)** Representative 2D class averages of negatively-stained Panx1 in lipid nanodiscs, with 826, 957, 920, and 440 particles (from top to bottom). **(e)** Representative 2D class averages of negatively-stained, cross-linked Panx1 in lipid nanodiscs, with 806, 517, 324, and 476 particles (from top to bottom).

Negative-stain EM data collection and processing	Panx1 in amphipols	Panx1 in nanodiscs	X-linked Panx1 in nanodiscs
Electron microscope	Tecnai F20	Tecnai F20	Tecnai F20
Electron detector	Gatan CCD (4k x 4k)	Gatan CCD (4k x 4k)	Gatan CCD (4k x 4k)
Voltage (kV)	120	120	120
Magnification	62,000	62,000	62,000
Defocus range (μm)	-0.75	-0.75	-0.75
Pixel size (Å)	1.82	1.82	1.82
Total electron dose ($e^-/Å^2$)	15	15	15
Exposure time (s)	1	1	1
Number of images	55	108	110
Number of particles	11,275	14,144	8,135
Number of classes	8	16	12
Box size (pix)	196 x 196	196 x 196	196 x 196

Table 3.2. Summary of data collection and statistics by single-particle negative-stain EM analysis.

3.2.7 Progress on single-particle cryoEM of Panx1 in lipid nanodiscs

Negative-stain EM of Panx1 reconstituted into lipid nanodiscs displayed characteristic channel features and different particle orientations (**Figure 3.7c-e, 3.8a**), indicating that the sample is suitable for 3D reconstruction by single-particle cryoEM. We first collected ~2500 electron micrographs of frozen-

hydrated Panx1-nanodisc samples at the National Center for Macromolecular Imaging (NCMI) using their JEOL3200FSC electron microscope equipped with a Gatan K2 Summit direct electron detector and energy filter (**Figure 3.8b**). A second data set was collected at the Electron Bio-Imaging Centre (eBIC) using their Titan Krios electron microscope equipped with a Gatan K2 Summit direct electron detector, energy filter and Volta phase plate (**Figure 3.8c**). Both data sets displayed circular densities in top view class averages consistent with end-on views of α-helices (**Figure 3.8 b,c**). Importantly, by using the phase plate, the top view class averages derived from the eBIC data showed improved definition of α-helical secondary structure in the heptameric oligomers compared to the NCMI data; however, the side view class averages of the eBIC data did not reveal any secondary structural details, presumably due to increased background resulting from increased ice thickness (**Figure 3.8 b,c**). Thus, in order to achieve 2D class averages clearly showing α-helical secondary structure in both top and side views, we continued to optimize the ice thickness. We used an automated Vitrobot rather than a manual plunge-freezing device to have better control over ice thickness. We also performed an initial screen of the grids using our FEI Tecnai F20 electron microscope equipped with a 4K x 4K CCD camera or Titan Krios electron microscope equipped with a Falcon II direct detector at UVA-MEMC, to select grids with ideal ice thickness for cryoEM data collection. The freezing conditions that yielded optimally thin ice for cryoEM data collection were using C-flat 1.2/1.3 grids with an 8 sec blotting time at 4 °C and 100% humidity. A third data set of ~3500 cryomicrographs was then collected at the National Cryo-

Electron Microscopy Facility at the National Cancer Institute (NCI-NCEF) using their Titan Krios electron microscope equipped with a Gatan K2 Summit direct electron detector, energy filter and Volta phase plate. The NCEF data set was significantly improved, and α-helical density was visualized in both top and side view class averages (**Figure 3.8d**). Thus, 3D reconstruction was pursued using this data set.

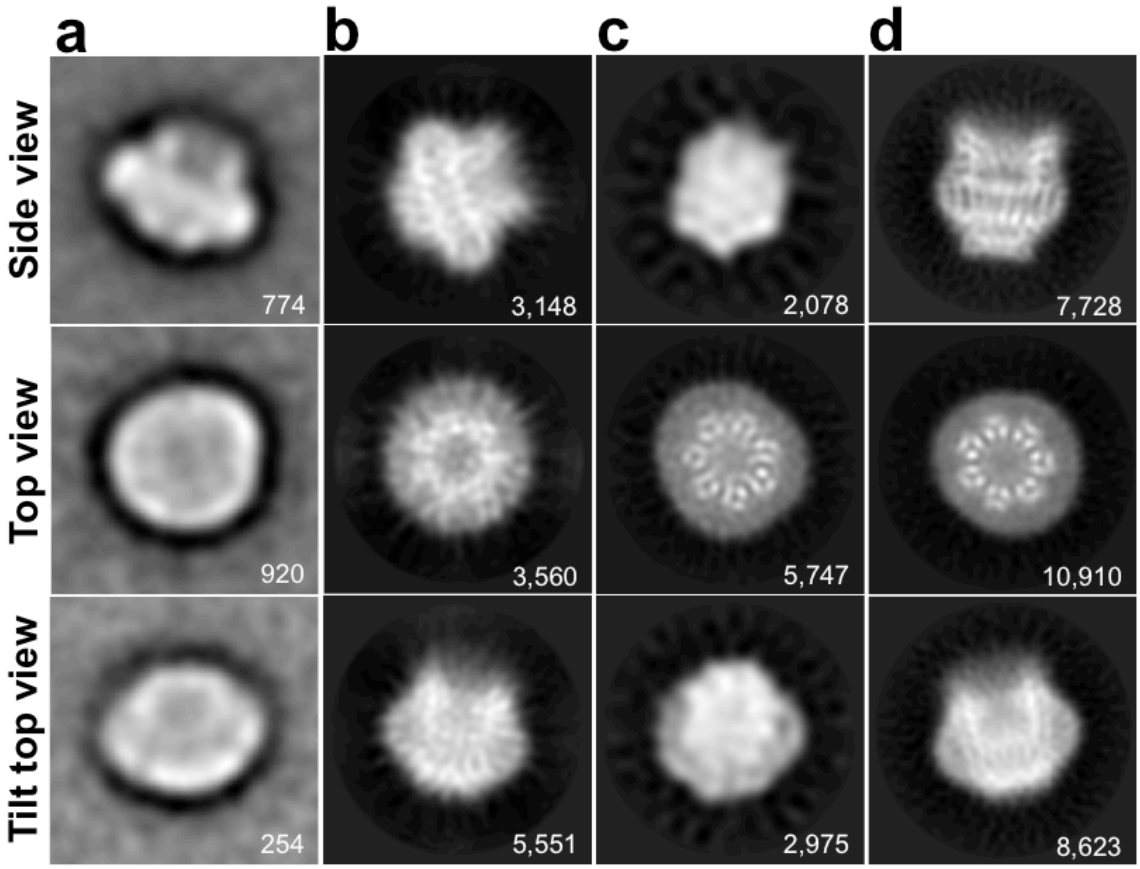

Figure 3.8. 2D class averages derived from negatively-stained and frozen-hydrated Panx1 channels in lipid nanodiscs. (a) Negative-stain EM data collected at UVA-MEMC using Tecnai F20 electron microscope equipped with a 4K x 4K CCD camera. **(b)** CryoEM data collected at NCMI using JEOL3200FSC electron microscope equipped with a Gatan K2 detector (without a phase plate). **(c)** CryoEM data collected at eBIC using Titan Krios electron microscope equipped with a Gatan K2 detector and a phase plate. **(d)** CryoEM data collected at NCEF using Titan Krios electron microscope equipped with a Gatan K2 detector and a phase plate. The number of particles used to derive the class averages is indicated.

3.2.8 Single-particle cryoEM analysis of Panx1 in lipid nanodiscs

C-terminally truncated frog Panx1 (frPanx1 (1-357)) reconstituted into lipid nanodiscs was imaged in vitreous ice using the NCEF Titan Krios equipped with a Gatan K2 Summit direct electron detector, energy filter and a Volta phase plate (VPP) at low defocus (-0.5 μm). Panx1 particles were homogenous, monodisperse and readily discernible for particle picking due to the high contrast provided by VPP (**Figure 3.9a**). An initial particle data set of 687,949 particles was subjected to reference-free 2D classification, which revealed averages with secondary structure features and sufficient distribution in particle orientations to enable 3D reconstruction (**Figure 3.9b**). A subset of 319,685 particles derived from 2D class averages was subjected to 3D classification, in which two of the ten 3D classes showed α-helical structures in the transmembrane regions. Class 6 displayed a larger diameter nanodisc compared with class 8 (**Figure 3.9c**). We note that the large and small nanodiscs were also observed for the MsbA-nanodisc complex[189]. The Panx1 small-nanodisc class contained particles of both top and side views, which were used for further 3D refinement (**Figure 3.9d**). A 3D map was reconstructed from 38,724 particles within the small-nanodisc class, in which C7 symmetry was imposed for 3D auto-refinement. On the basis of the gold-standard Fourier Shell Correlation (FSC) criteria, the overall resolution was 7.0 Å (**Figure 3.9c,f**). Estimation of the local resolution showed a narrow resolution range (6.6 Å to 7.6 Å), in which the transmembrane region has slightly higher resolution than the cytoplasmic and extracellular regions (**Figure 3.9e**). **Table 3.3** summarizes the data collection and image processing statistics.

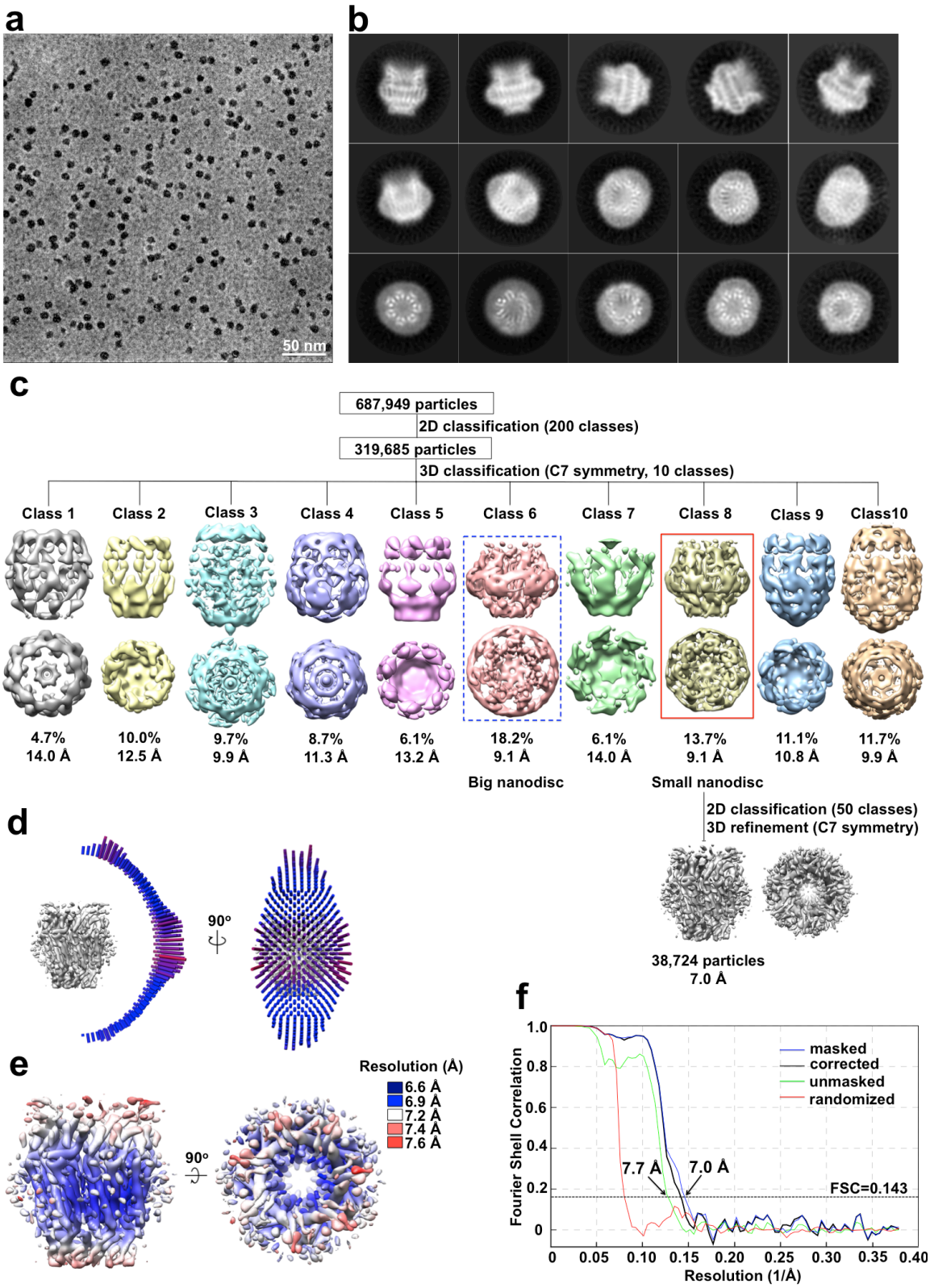
a
50 nm
b
c
687,949 particles
2D classification (200 classes)
319,685 particles
3D classification (C7 symmetry, 10 classes)
Class 1
Class 2
Class 3
Class 4
Class 5
Class 6
Class 7
Class 8
Class 9
Class10
4.7%
14.0 Å
10.0%
12.5 Å
9.7%
9.9 Å
8.7%
11.3 Å
6.1%
13.2 Å
18.2%
9.1 Å
6.1%
14.0 Å
13.7%
9.1 Å
11.1%
10.8 Å
11.7%
9.9 Å
Big nanodisc
Small nanodisc
2D classification (50 classes)
3D refinement (C7 symmetry)
38,724 particles
7.0 Å
d
90°
e
Resolution (Å)
6.6 Å
6.9 Å
7.2 Å
7.4 Å
7.6 Å
90°
f
masked
corrected
unmasked
randomized
Fourier Shell Correlation
1.0
0.8
0.6
0.4
0.2
0
7.7 Å
7.0 Å
FSC=0.143
0
0.05
0.10
0.15
0.20
0.25
0.30
0.35
0.40
Resolution (1/Å)

Figure 3.9. Single-particle cryoEM analysis of Panx1 in lipid nanodiscs. (a) Representative raw electron micrograph of frozen-hydrated Panx1 in lipid nanodiscs. Scale bar, 50 nm. **(b)** 2D class averages of Panx1-nanodisc particles derived from (a). The particle box dimension is 238 Å. **(c)** Image processing workflow. With applying C7 symmetry, two out of ten classes generated from 3D classification revealed α-helical structures in the transmembrane domain, with two sizes of nanodiscs (big nanodisc class in blue box and small nanodisc in red box). Particles assigned to the red-boxed, small-nanodisc class were used for further refinement. The distribution of all particles (%) and the resolution of each class are indicated. **(d)** Angular distribution plot of all particles included in the final C7-symmetrized 3D reconstruction, showing both side and top view orientations. The length and the colour of cylinders correspond to the number of particles with respective Euler angles. **(e)** Final 3D reconstruction was coloured according to local resolution estimation, showing as side and top views. **(f)** Fourier shell correlation (FSC) curves of the final refined masked (blue), unmasked (green), phase-randomized (red) and corrected for mask convolution effects (black) cryoEM density map.

CryoEM data collection and processing	**Frog Panx1 (1-357)**
Electron microscope	Titan Krios
Electron detector	K2 Summit
Voltage (kV)	300
Magnification	105,000
Defocus range (μm)	-0.3 to -1.2
Pixel size (Å)	1.32
Total electron dose ($e^-/Å^2$)	40
Exposure time (s)	10
Number of images	3566
Number of frames per image	40
Phase plate periodicity	25
Initial particle number	687,949
Final particle number	38,724
Symmetry imposed	C7
Map resolution (Å)	7.0
Map sharpening B factor ($Å^2$)	-898

Table 3.3. Summary of data collection and statistics by single-particle cryoEM analysis.

3.2.9 Architecture of the heptameric Panx1 channel at subnanometer resolution

2D class averages showed that heptameric Panx1 channel with circular densities consistent with end-on views of α-helices floating within the nanodisc (top view), and transmembrane helices were clearly visible within a disc-like density contributed by the scaffold protein and lipid bilayer within the nanodisc (side view) (**Figure 3.9b, 3.10a**). The density map of Panx1 was divided into three parts: the cytoplasmic domain, the transmembrane domain and the extracellular domain, in which the transmembrane domain is approximately perpendicular to the membrane; the cytoplasmic domain is wider than the extracellular domain, reminiscent of a truncated funnel (**Figure 3.10b**). The general shape resembles that of the INX-6 hemichannel (HC)[47] and the LRRC8A channel pore domain (PD)[139]. The longitudinal height of Panx1 channel was ~105 Å (**Figure 3.10b**), which is similar to the octameric INX-6 HC[47] and the hexameric LRRC8A (PD)[139], in contrast to the shorter Cx HCs presumably due to their invisible cytoplasmic regions[43,44] (**Table 3.4**). The channel width is biggest at the cytoplasmic side of membrane region, ~105 Å (**Figure 3.10b**), which is smaller than that of the octameric INX-6[47] but larger than the hexameric Cx26[44] (**Table 3.4**), presumably due to different molar mass and number of protein subunits within the channels.

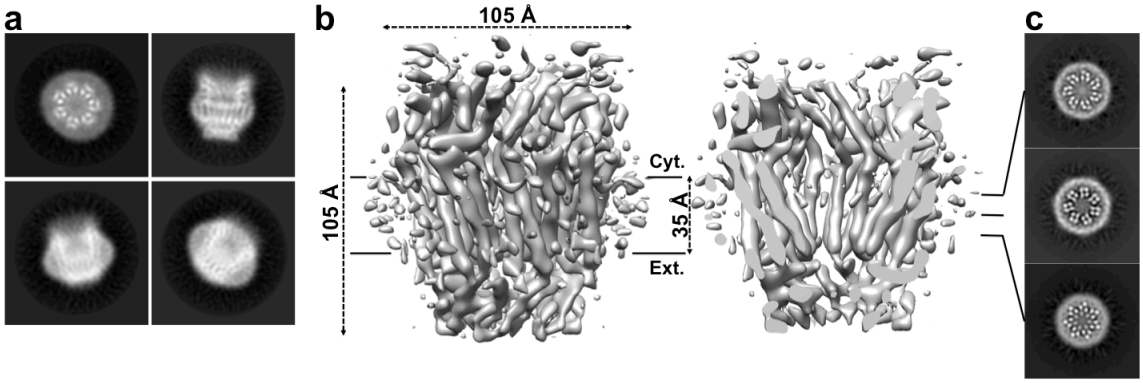

Figure 3.10. CryoEM of Panx1 in lipid nanodiscs. (a) Representative 2D class averages of Panx1 in lipid nanodiscs, with top and side views. Box dimension is 238 Å. **(b)** Surface and cross-sectional views of Panx1 cryoEM density map in side view. Channel height and width were both ~105 Å. Membrane regions defined by nanodisc was ~35 Å. Cyt, cytoplasm; Ext, extracellular space. **(c)** Slices through the 3D reconstruction at locations indicated in b.

Seven Panx1 subunits surround a central pore axis to form the seven-fold symmetric channel (**Figure 3.11a**). Each subunit is comprised of a 4-helix bundle, which were clearly resolved in our cryoEM density map, similar in design to gap junction channels (GJCs)[43] (**Figure 3.10c**). Surprisingly, unlike the poorly visualized and disordered cytoplasmic regions in Cx GJCs[43-45], the well-folded cytoplasmic regions of Panx1 are clearly observed (**Figure 3.10, 3.11**), although the local resolution estimation suggests that the cytoplasmic helices are slightly less-well resolved than the transmembrane helices (**Figure 3.9e**). Such well-defined structural features suggest that Panx1 as visualized here adopts a defined conformation of a membrane channel with well-ordered domain architecture.

In the cytoplasmic domain, the helices probably from the cytoplasmic loop and the C-terminus in seven subunits formed a dome-like pore entrance, with a diameter of ~42 Å (**Figure 3.11b**), which is similar to the cytoplasmic pore diameter of N-terminally truncated INX-6 (INX-6 ΔN)[46], but larger than that of wild-type INX-6 (INX-6 WT)[47] and LRRC8A (PD)[139] (**Table 3.4**), presumably due to the Panx1 truncated C-terminus. In the extracellular domain, a small pore with a diameter of ~12 Å formed the channel entrance (**Figure 3.11b**), which is more like the constricted extracellular side of LRRC8A (PD)[139]. The estimated extracellular pore diameter (~12 Å) is smaller than the effective diffusion diameter of ATP (~14 Å). The limited resolution of 7 Å precludes us from determining whether Panx1 is in a closed or open conformation. However, we expect that side chain densities across the pore diameter would occupy, more consistent with a closed conformation.

Nevertheless, we did observe a well-defined density between adjacent subunits (**Figure 3.11c**), which may be a lipid or CHS molecule that stabilizes the transmembrane domain. A similar unassigned density was also observed in the INX-6 high-resolution map[190].

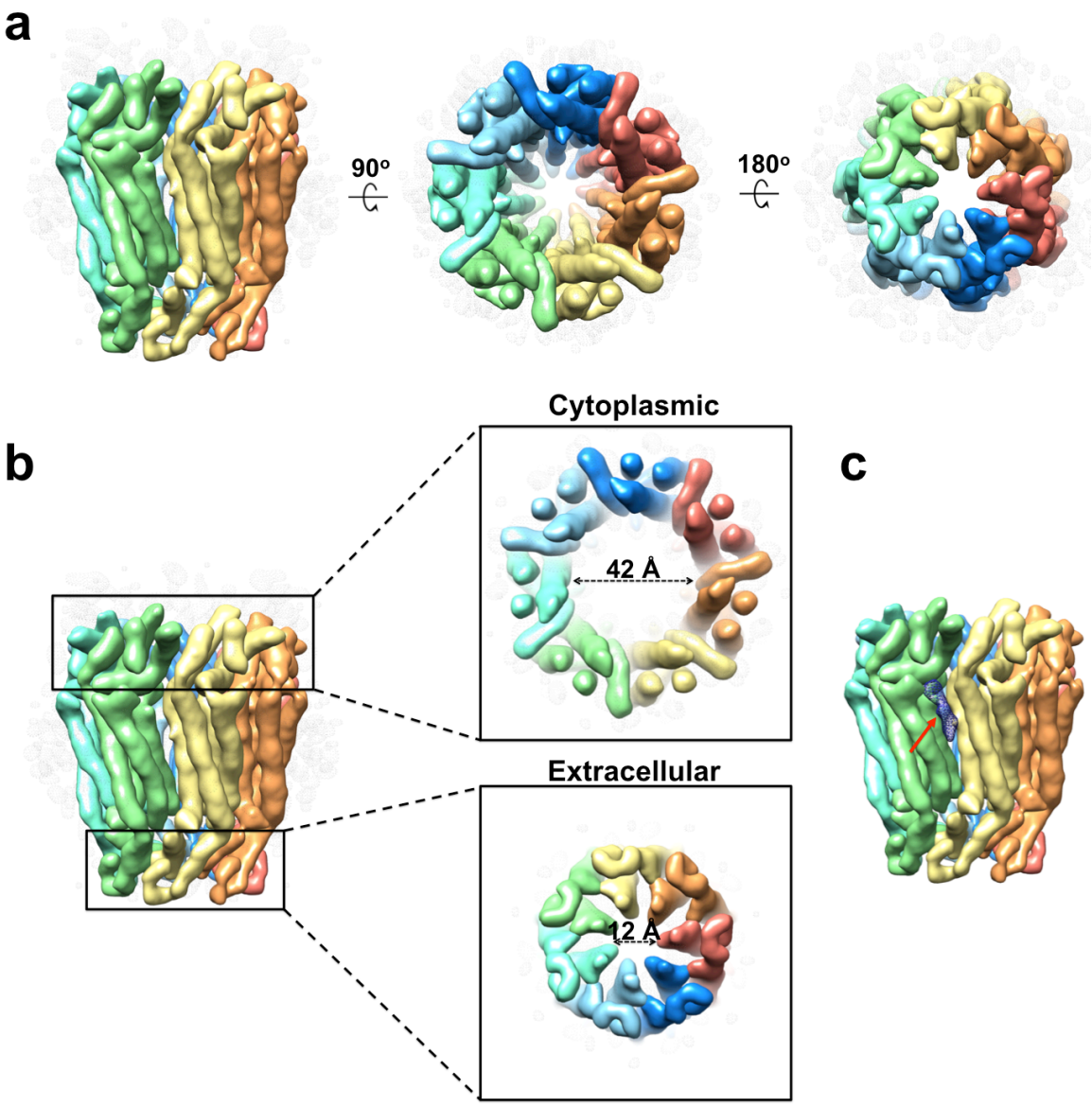

Figure 3.11. Segmented cryoEM density map of Panx1 in lipid nanodiscs. (a) Side and top (middle, from cytoplasmic surface; right, from extracellular surface) views of segmented cryoEM density map of Panx1 in lipid nanodiscs. CryoEM densities of nanodiscs were shown as light grey dot. Seven subunits were coloured. **(b)** Cytoplasmic and extracellular views of segmented cryoEM density map of Panx1, with pore diameters of 42 Å and 12 Å, respectively. **(c)** Side view of segmented cryoEM density map of Panx1, with a putative lipid or CHS density between adjacent subunits, shown as blue mesh and indicated by red arrow.

Structures	Cytoplasmic diameter	(Hemi)channel height	Cytoplasmic pore diameter	Extracellular pore diameter
Cx43(263T) (Unger *et al.*, 1999)	70 Å	75 Å	40 Å	15 Å
Cx26 (Maeda *et al.*, 2009)	92 Å	80 Å	40 Å	14 Å
INX-6ΔN (Oshima *et al.*, 2016)	115 Å	120 Å	40 Å	30 Å
INX-6WT (Oshima *et al.*, 2016)	110 Å	100 Å	30 Å	19 Å
LRRC8A (PD) (Deneka *et al.*, 2018)	110 Å	100 Å	32 Å	6 Å
Panx1	105 Å	105 Å	42 Å	12 Å

Table 3.4. Comparison of channel dimensions and pore diameters of Panx1 with other tetra-spanning membrane channels.

3.2.10 Similar transmembrane helical arrangement of Panx1 with other tetra-spanning membrane channels

Despite low sequence similarity, the 4-helix bundle transmembrane (TM) architecture is conserved between connexin, innexin and LRRC8A channels as revealed by super-position of their membrane-inserted helices[139]. Since sequence alignment showed that the TM domains are well conserved between Panxs and LRRC8 proteins[134], it would be interesting to see whether Panx1 also shares a similar arrangement of TM helices. By side-to-side comparison, heptameric Panx1 displays a similar 4-helix TM bundle subunit design with the hexameric Cx26 (PDB code: 2zw3) and LRRC8A (PDB code: 6g8z) channels, as well as octameric INX-6 (PDB code: 5h1q) channels (**Figure 3.12**). This

conserved 4-helix bundle design allowed us to assign the Panx1 TM helices, in which the innermost pore lining helix is TM1, with TM2, TM3 and TM4 positioned in a counter-clockwise order when viewed from the cytoplasmic side of the membrane (**Figure 3.12**). Nonetheless, comparison of the side views of the TM 4-helix bundles showed that Panx1 mostly closely resembled LRRC8A, presumably due to different lengths of TM helices defined in different protein channels.

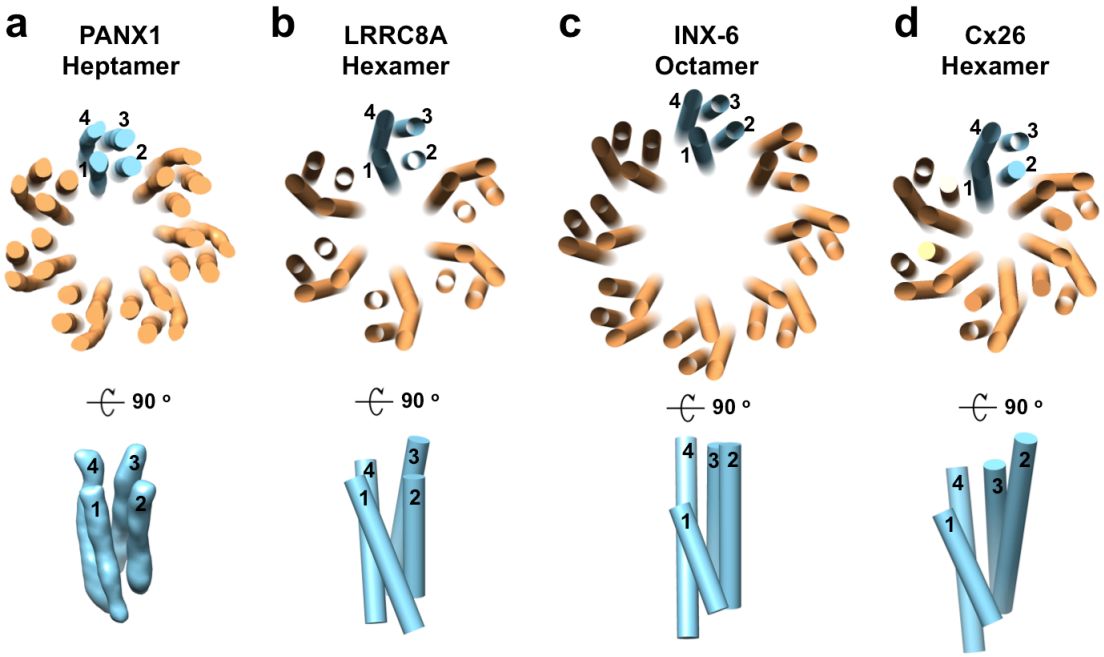

Figure 3.12. Panx1 showed a similar transmembrane helical arrangement with other tetra-spanning membrane channels. Cross-sectional, oligomeric, top view (viewed from cytoplasmic side of membrane) and monomeric, side view of transmembrane (TM) helices from heptameric Panx1 **(a)**, hexameric LRRC8A (PDB code: 6g8z)[139] **(b)**, octameric INX-6 (PDB code: 5h1q)[47] **(c)** and hexameric Cx26 (PDB code: 2zw3)[44] **(d)**. Panx1 TM helices are shown as segment map; other protein TM helices are shown as solid-cylinder representation, prepared by UCSF chimera[191].

3.2.11 Monomeric structure of Panx1 resembles LRRC8A more than INX-6

The monomeric structure of Panx1 showed a seahorse-like architecture, with the cytoplasmic domain representing the head, the 4-helix TM bundle representing the body and the extracellular domain representing the tail, which is in general similar to the monomeric architectures of INX-6[47] and LRRC8A (PD)[139] (**Figure 3.13b**). To investigate the structural similarity and differences in detail, we fitted the atomic ribbon model of LRRC8A (PDB code: 6g8z)[139] or INX-6 (PDB code: 5h1q)[47] into our cryoEM density map of Panx1 using the 'fit-in-map' function of UCSF Chemira[191]. This operation showed that LRRC8A displayed a better fit than INX-6 in all three regions of the Panx1 density map. As expected, the most conserved TM domains[37,134] showed the best fitting for both LRRC8A and INX-6, except for an obvious difference in the amino terminus (NT) and the TM1 helix. The longer TM1 helix with a short extended loop towards the pore of LRRC8A was fitted better into Panx1 density map compared with the shorter TM1 helix with a NT α-helix that projects towards the extracellular direction (**Figure 3.13c**). In the cytoplasmic regions (CL and CT), Panx1 and LRRC8A showed both similarity and differences. The CL helices, which connect TM2 and TM3 helices, are placed up with a wide kinked angle relative to TM2 helix in both Panx1 and LRRC8A, reminiscent of a raised-up seahorse head, in contrast to the relatively sharper kinked angle in INX-6 (**Figure 3.13c**). Nevertheless, the CT domains showed significant differences between Panx1 and LRRC8A or INX-6. The cryoEM density corresponding to the CT helices of Panx1 extend towards the adjacent subunit direction, in contrast to a helix-turn-helix architecture formed

by three or four short CT helices in LRRC8A and INX-6 (**Figure 3.13c**). Structural studies of mouse Panx1 cytoplasmic domains using a combination of structural prediction tools and circular dichroism (CD) spectroscopy of peptides in the CL and CT characterized several helical regions [39], which show similar locations with the cytoplasmic helices in LRRC8A and INX-6 (**Figure 3.13a**). By this similarity to LRRC8A and INX-6, we putatively assigned the corresponding helices in Panx1. Surprisingly, in the extracellular domain, Panx1 cryoEM density corresponding to the short EL1 helix (E1H) and three EL β-sheets (E1β, E2β1, and E2β2) of LRRC8A were also observed. It was showed that the EL1 helices form the most constricted pore entrance of LRRC8A[139]. The EL1 of Panx1 was predicted to interact with channels inhibitor carbenxolone (CBX)[192]. Thus, the putative EL1 α-helix of Panx1 may correspond to E1H of LRRC8A, and be involved in channel gating.

In summary, on the basis of membrane topology, SCAM analysis[40], sequence alignment[37,134], secondary structure information[39], and fitting of LRRC8A structures into the Panx1 cryoEM density map, we putatively assigned the helices of Panx1, which may provide insights into the structure-function relationships of the channels. The innermost pore lining helix is TM1, facing the pore pathway, with TM2, TM3 and TM4 positioned in a counter-clockwise order when viewed from the cytoplasmic side of the membrane. Two CL helices in the cytoplasmic region are connected to TM2 and TM3 with a wide kinked angle,

presumably by conserved proline residue. A putative EL1 helix in the extracellular domain might be involved in Panx1 channel gating.

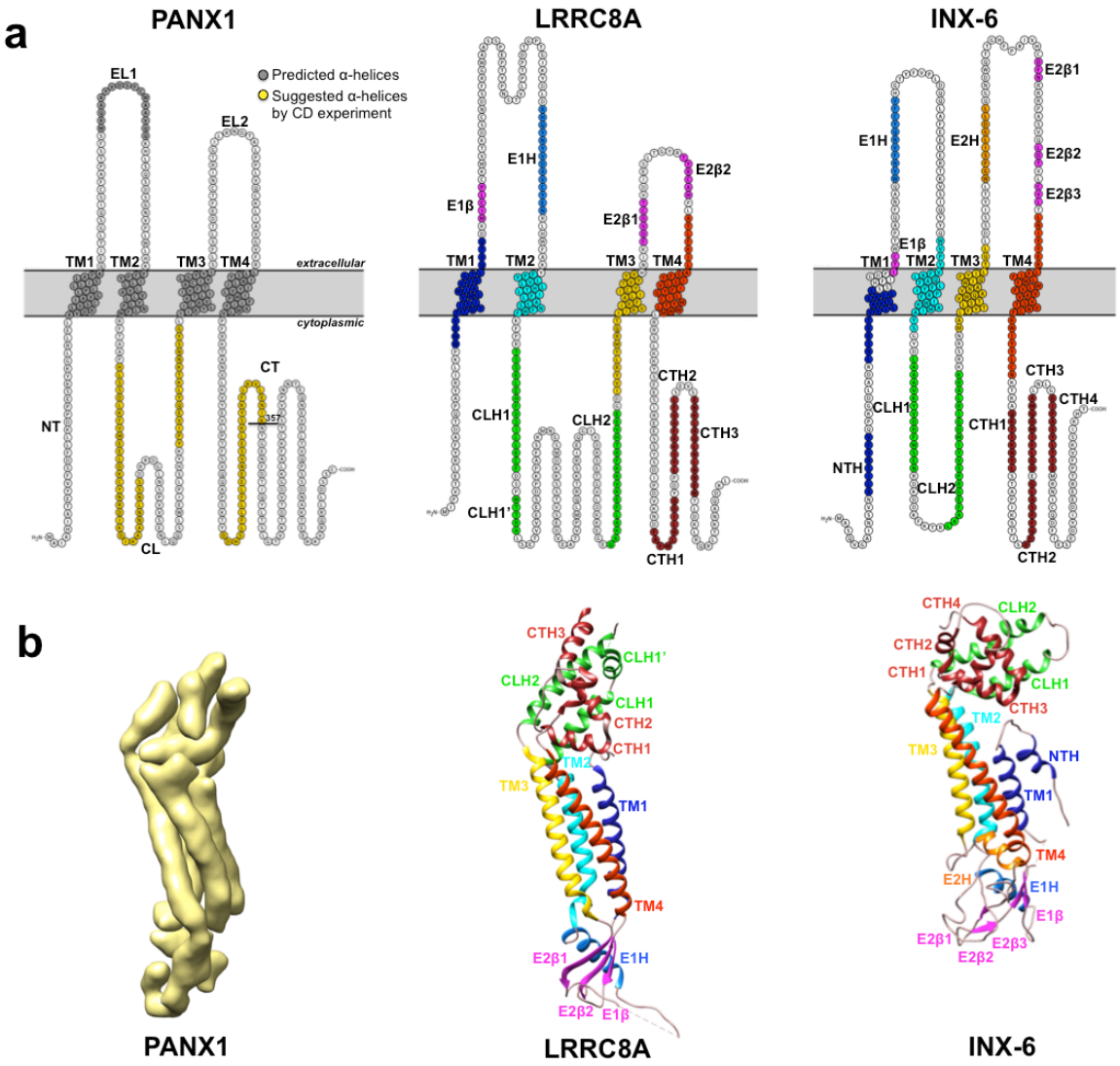

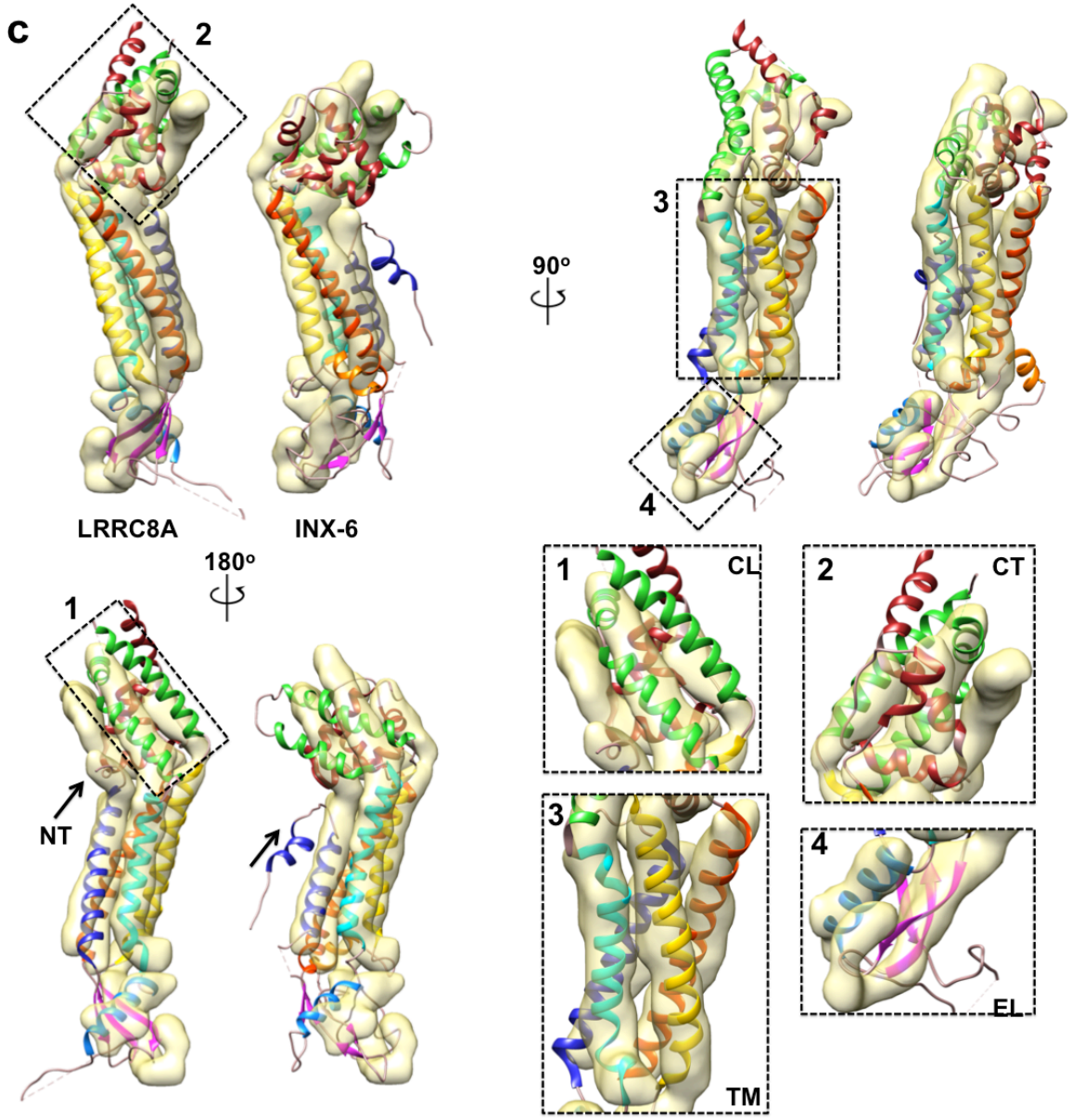

Figure 3.13. Comparison of monomeric structures of Panx1 with LRRC8A and INX-6. (a) Membrane topology of frog Panx1, mouse LRRC8A and *C. elegans* INX-6, with residues coloured by secondary structures. Panx1 was coloured based on secondary structure prediction (gray) and CD spectroscopy analysis[39] (yellow). LRRC8A and INX-6 were coloured based on cryoEM structures of LRRC8A (PDB code: 6g8z)[139] and INX-6 (PDB code: 5h1q)[47], respectively. **(b)** Monomeric structures of Panx1, LRRC8A and INX-6, shown as segment map (Panx1) and ribbon models (LRRC8A and INX-6). Secondary structures were coloured according to (a) for LRRC8A and INX-6. **(c)** Rigid body fit of atomic models of LRRC8A (left) and INX-6 (right) into Panx1 segment map, using 'fit-in-map' function of UCSF Chemira[191]. Corresponding regions for LRRC8A fitted into Panx1 density maps are boxed and showed in an expanded view, with indicated number. TM, transmembrane domain; EL, extracellular loop; CL, cytoplasmic loop; NT and CT, amino and carboxyl termini.

3.2.12 C-terminally truncated Panx1 channel in a closed conformation was activated by α1D adrenoceptor-mediated signaling pathway

Panx1 channels can be activated by G protein-coupled receptor (GPCR) mediated signaling pathways[34,66-68,70], such as phenylephrine binding to α1 adrenergic receptors, which triggers ATP release from activated Panx1 channels to regulate blood pressure[68,69,88]. To test whether our C-terminally truncated frog Panx1 (frPanx1 (1-357)) construct is a functional channel, we co-transfected frPanx1 (1-357) and α1D adrenoceptors (α1DRs) into HEK293 cells and monitored whole-cell currents by patch clamp electrophysiology (**Figure 3.14a**). Whole-cell recordings obtained from co-transfected HEK293 cells showed that unstimulated, C-terminally truncated Panx1 channels were basally silent (**Figure 3.14b**), similar to the earlier reports of basally silent, full-length human Panx1 channels[50,78], indicating that C-terminally truncated Panx1 channel is in a closed conformation, in spite of the CT truncation. We interpret this result to indicate that the gate is mediated by the small extracellular pore. Phenylephrine (PE) induced outwardly rectifying current, which was abolished by carbenoxolone (CBX), a known Panx1 inhibitor (**Figure 3.14b**). These results suggest that the C-terminally truncated Panx1 channels are in a basally closed state, which can be activated by the a1DR mediated signaling pathway. We presume that activated a1DR induces phosphorylation of a cytoplasmic region of Panx1 via a cytoplasmic kinase. Consequently, a transmembrane conformational change must take place to open the extracellular gate. Testing of this hypothesis will require high-resolution structural studies of phosphorylated (open) and

dephosphorylated (closed) Panx1 channels.

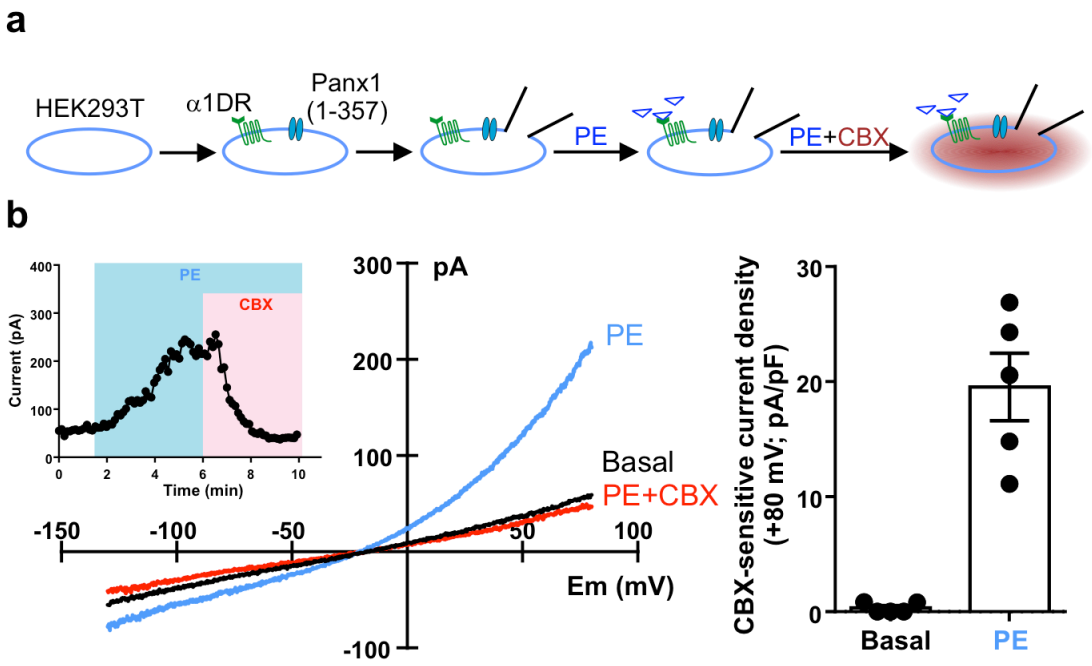

Figure 3.14. C-terminally truncated Panx1 channel in a closed conformation was activated by α1D adrenoceptor-mediated signaling pathway. (a) Schematics show the whole-cell recordings process. **(b)** Whole-cell recordings from HEK293T cells co-expressing a1D adrenoceptors (a1DRs) and frPanx1 (1-357) channels. Panx1 channel activity was induced by phenylephrine (PE, 20 μM), and abolished by carbenoxolone (CBX, 50 μM). (Experiment was performed by Dr. Yu-Hsin Chiu, Dr. Douglas Bayliss Laboratory, University of Virginia)

3.2.13 Concluding remarks

In this study, we reconstructed a 7 Å resolution three-dimensional cryoEM density map of C-terminally truncated frog Panx1 (frPanx1 (1-357)) reconstituted in lipid nanodiscs. Unexpectedly, Panx1 subunits assemble as heptameric channels by surrounding a central seven-fold symmetric pore axis. Our observation of the heptameric Panx1 channels suggests reappraisal of the existing views that Panx1 is a connexin-like hexameric channel. Although connexin hemichannels are considered to be hexameric on the basis of known structures[43-45,151], recently cryoEM structure of INX-6 showed that innexin hemichannels are octameric[47]. Along with our observation of heptameric pannexin channels, it suggests that the variety of oligomeric states in gap junction channels may be related to their different functional roles and evolutionary mechanisms.

The cryoEM density map clearly resolved the TM helices, which fold as a 4-helix bundle in each Panx1 subunit. Despite low sequence homology and different oligomeric states, the 4-helix bundle structure of Panx1 recapitulates a similar subunit design with other oligomeric, tetra-spanning membrane protein channels such as connexins, innexins and LRRC8 protein channels. Surprisingly, unlike the disordered cytoplasmic domains in connexin channels, the cytoplasmic domains of Panx1 are well-defined and form a dome-like structure of the channel, similarly to INX-6[47] and LRRC8A[139] channels. By rigid body fitting of LRRC8A or INX-6 model into the Panx1 cryoEM density map, we found that

Panx1 channel resembles LRRC8A protein channel more than INX-6, which is consistent with the sequence alignment analysis that pannexins are evolutionary closer to LRRC8 proteins than innexins[37,134]. Interestingly, we found that calcium can significantly improve the stability and homogeneity of Panx1 channels; however, the mechanisms such as calcium binding sites are still unclear. We also observed a large cytoplasmic vestibule and a small extracellular pore. Electrophysiological recordings showed that the C-terminally truncated Panx1 channels are in a closed conformation, which can be activated by α1D adrenoceptor-mediated signaling pathway. It has been shown that Panx1 channels can be activated by caspase cleavage of the distal C-terminus for ATP release, which is an irreversible process[50,78]. Thus, without C-terminal autoinhibitory regions, Panx1 channels display a large cytoplasmic pore, and presumably adopt a closed conformation by forming a constricted, small extracellular pore, maintaining the cells alive during protein expression, assembly, transport and insertion in the plasma membrane.

3.3 Experimental methods

3.3.1 Protein expression and purification

Protein expression and purification were performed as previously described[48], with modifications. Specifically, C-terminally truncated (deletion from residue 358 to 428) frog Panx1 (NCBI: NP_001123728, 428 aa) was modified with a thrombin cleavage recognition sequence (LVPRGS) followed by a strep tag II (WSHPQFEK) at the carboxyl terminus. The construct was subcloned into the pFastBac1 vector (Invitrogen) for baculovirus expression in *Spodoptera frugiperda* (*Sf9*) insect cells using the Bac-to-Bac expression system (Invitrogen). Recombinant Panx1 baculovirus was used to infect *Sf9* insect cells grown at 27 °C to a density of 2×10^6 ml^{-1}, at a multiplicity of infection (MOI) of 3. Cells were collected 48 h after infection by low-speed centrifugation at 2,000 x g. To isolate membrane-localized Panx1, *Sf9* cell pellets were resuspended in low salt buffer (50 mM HEPES, pH 7.5, 50 mM NaCl, 0.5 mM EDTA and protease inhibitor cocktails (Roche)) and lysed by Dounce homogenization (~30 strokes). Nucleic acids were digested by adding $MgCl_2$ to 2.5 mM and Benzonase (EMD Millipore) to ~12.5 units per 1 ml lysate, with gentle stirring at 4 ^oC for 20 min. Membranes were collected by ultracentrifugation at 100,000 x g and washed with stepwise Dounce homogenization in low salt buffer and high salt buffer (50 mM HEPES, pH 7.5, 1 M NaCl, 0.5 mM EDTA and protease inhibitor cocktails). Pellets were isolated by ultracentrifugation at 100,000 x g between steps. The final Dounce homogenization was performed in intermediate salt buffer (50 mM HEPES, pH

7.5, 500 mM NaCl), followed by ultracentrifugation at 100,000 x g. The membrane pellet was solubilized at 4 °C for 4 h with 1% (w/v) n-dodecyl-β-D-maltopyranoside (DDM, Anatrace) and 0.2% (w/v) cholesteryl hemisuccinate (CHS, Anatrace) in 50-100 ml of buffer containing 50 mM HEPES, pH 7.5, 300 mM NaCl, 3 mM $CaCl_2$, 2.5% glycerol and protease inhibitor cocktails. Insoluble material was removed by ultracentrifugation at 100,000 x g, and the supernatant was incubated with ~1.0 ml of Strep-Tactin Superflow Plus resin (QIAGEN) overnight at 4 °C. The resin was packed in an Econo-column (Bio-Rad, 1.0 x 10 cm) and washed with high salt buffer (50 mM HEPES, pH 7.5, 1 M NaCl, 3 mM $CaCl_2$ and 0.05% DDM with 0.01% CHS), for 20 column volumes/wash, and eluted with 2.5 mM Desthiobiotin (Sigma) in buffer (50 mM HEPES, pH 7.5, 500 mM NaCl, 3 mM $CaCl_2$ and 0.02% DDM with 0.004% CHS). The eluted protein was concentrated to 2-3 mg ml^{-1} using an Amicon ultracel-100 centrifugal filter unit (EMD Millipore) for amphipol exchange or nanodisc reconstitution. Analytical size-exclusion chromatography (SEC) was performed on a Superpose 6 increase 10/300 GL column (GE Healthcare) interfaced to an AKTA Purifier10 HPLC system (GE Healthcare), equilibrated with buffer (50 mM HEPES, pH 7.5, 500 mM NaCl, 3 mM $CaCl_2$ and 0.02% DDM with 0.004% CHS).

3.3.2 Amphipol exchange and nanodisc reconstitution

For amphipol exchange, purified Panx1 in DDM/CHS was mixed with amphipathic surfactant Amphipol A8-35 (Anatrace) at a ratio of 1:3 (*w/w*) by

gentle agitation for 4 h at 4 °C. The DDM/CHS detergent was then removed by overnight incubation with Bio-Beads SM-2 (15 mg per 1 ml protein/detergent/amphipols mixture, Bio-Rad) at 4 ^{o}C, and the Bio-Beads were subsequently removed using a disposable polyprep column (Bio-Rad).

For nanodisc reconstitution, membrane scaffold protein 2N2 (MSP2N2) was expressed and purified from *Escherichia coli* as previously described[193], with modifications. The purified MSP2N2 was solubilized in buffer (50 mM Tris pH 8.0, 100 mM NaCl, 4 mM β-mercaptoethanol (β-ME), 2 mM EGTA and 10 mM sodium cholate). 2.5 mg soybean polar lipid extract (Avanti) dissolved in chloroform was dried under an argon stream to form a lipid film. Residual chloroform was further removed by vacuum desiccation for 3 h. The lipid film was then rehydrated in buffer (25 mM Tris pH 7.5, 150 mM NaCl, 2% n-octyl-β-D-glucopyranoside (OG) (*w/v*)) by vigorous mixing, resulting in a clear lipid stock at 10 mM concentration. Purified Panx1 (2-3 mg ml^{-1}, 45-70 μM) solubilized in DDM/CHS was mixed with the soybean lipid stock (7.5 mg ml^{-1}, 10 mM) and MSP2N2 (2.4 mg ml^{-1}, 56 μM) at a molar ratio of 1 : 1.25 : 125 (Panx1 monomer : MSP2N2 : soybean lipid) and incubated on ice for 1 h. Bio-beads SM2 (10 mg ml^{-1}, Bio-Rad) were added to initiate the reconstitution by removing detergents from the system, and the mixture was incubated at 4 °C for 1 h with constant rotation. A second aliquot of Bio-beads was then added to increase the concentration to 30 mg ml^{-1}, and the sample was incubated at 4 °C overnight with constant rotation. Bio-beads were subsequently removed using a disposable polyprep column (Bio-Rad).

Panx1 in amphipols or nanodiscs was further purified by size-exclusion chromatography (SEC). Insoluble material was removed by ultracentrifugation at 150,000 x g for 20 min before purification by SEC on a Superpose 6 increase 10/300 GL column (GE Healthcare) equilibrated with buffer (25 mM HEPES, pH 7.5, 150 mM NaCl and 3 mM $CaCl_2$). The peak fractions corresponding to heptameric Panx1 were collected and concentrated to ~0.2 mg ml^{-1} using a 0.5 ml concentrator with 100 kDa cut-off (EMD Millipore), for negative-stain EM and cryoEM analyses. In addition to SEC, Panx1 purity was assessed by SDS–polyacrylamide gel electrophoresis (PAGE) using 4-20% pre-cast acrylamide gradient Tris-glycine gel (Bio-Rad) stained with Simply Blue (SimpleBlue Safe Stain, Novex), and Western immunoblot using anti-Strep antibodies (Qiagen).

3.3.3 Negative-stain EM and image analysis

An aliquot (3.5 µl) of purified Panx1-nanodisc complex (0.01-0.02 mg ml^{-1}) was applied to a glow-discharged, copper grid covered with a thin layer of continuous carbon film (300-mesh, Electron Microscopy Sciences), and stained with 2% (w/v) uranyl acetate[175]. Negatively-stained EM grids were imaged on a Tecnai F20 electron microscope (FEI Company), operating at 120 kV. Images were recorded at a nominal magnification of ×62,000 and a defocus of -0.75 µm using a 4K × 4K charge-coupled device (CCD) camera (UltraScan 4000, Gatan), corresponding to a calibrated pixel size of 1.82 Å on the specimen.

EMAN2 software[173] was used for single-particle image analysis. To improve the signal-to-noise ratio and facilitate particle picking, negatively-stained electron micrographs were high-pass (100 Å) and low-pass (10 Å) Gaussian-filtered. A total of 11,275 Panx1-amphipol particles from 55 micrographs, 14,144 Panx1-nanodisc particles from 108 micrographs, and 8,135 cross-linked Panx1-nanodisc particles from 110 micrographs, were semi-automatically selected using the 'Swarm' tool in the e2boxer.py program of EMAN2, and extracted within boxes of 196 pixels × 196 pixels. The contrast transfer function (CTF) was estimated and corrected by the e2ctf.py program of EMAN2. Particle images were normalized, centered and subjected to 8 cycles of 2D classification using the e2refine2d.py program by iterative, multivariate statistical analysis (MSA). Statistics for negative-stain EM data collection and image processing are summarized in Table 3.2.

3.3.4 CryoEM sample preparation and data acquisition

An aliquot (3 µl) of purified Panx1-nanodisc sample (~0.2 mg ml^{-1} in buffer composed of 25 mM HEPES, pH 7.5, 150 mM NaCl and 3 mM $CaCl_2$) was applied to a glow-discharged (with amylamine) C-flat holey carbon grid (1.2 µm hole size and 1.3 µm hole spacing on 400-mesh copper grid). The grid was blotted with Whatman #1 filter paper for 7.5 s using a Vitrobot Mark IV (FEI) maintaining at 100% humidity and 4 ^{o}C with a blot force of 2, and the grid was plunge-frozen into liquid ethane cooled by liquid nitrogen.

Electron cryomicrographs of frozen-hydrated Panx1-nanodisc samples were collected at the National Cancer Institute's National Cryo-Electron Microscopy Facility (NCI-NCEF) at the Frederick National Laboratory for Cancer Research using a Titan Krios electron microscope (FEI), operated at 300 kV, equipped with a K2 Summit direct electron detector (Gatan), a GIF quantum energy filter (Gatan) with a 20 eV slit and zero-energy-loss mode to remove inelastic scattering, and a Volta phase plate (FEI). A total of 3,566 cryomicrographs were recorded using an automated acquisition program EPU (FEI), in EFTEM nanoprobe mode, using a 70 µm C2 aperture, at a nominal magnification of x105,000, corresponding to a calibrated physical pixel size of 1.32 Å per pixel on the specimen. Images were recorded at a defocus of -0.5 µm in counting mode, in which each image was fractionated into 40 frames with total exposure time of 10 s. At a dose rate of 6.97 e^-/pixel/sec, the total accumulated dose was 40 $e^-/Å^2$.

3.3.5 CryoEM image processing

All image processing was performed using RELION 2.1[176]. Movie frames (3-40) were used for correction of beam-induced motion and dose-weighting using MotionCor2[194], with 5 x 5 patches and the corresponding dose per frame. The contrast transfer function (CTF) parameters and phase shift were estimated using Gctf-v1.18[195]. Low-quality micrographs with considerable drift, high defocus or poor fitting of the CTF were discarded, resulting in a dataset of 2,644 images

for further image processing. 2,199 particles were manually picked and subjected to an initial reference-free 2D classification (10 classes), in which five distinctive 2D class averages were selected and used as templates for automated particle picking in RELION[196]. Auto-picked particles on each micrograph were manually screened to discard wrongly picked ice contamination, extracted with a box size of 180 x 180 pixels, and sorted by similarity to reference images to discard those with low z-scores. A starting dataset of 687,949 particles was generated for 2D classification. After one round of 2D classification (200 classes), false positive and poor quality particles were discarded, resulting in 319,685 particles for 3D classification. CryoSPARC[197] was used to analyze a subset of 84,415 particles from 2D classification in order to generate an *ab initio* model. RELION 2.1[176] was then used to perform 3D classification (1 class, C7 symmetry) and manual refinement by adjusting the angular sampling degree (from 7.5^{o} to 3.7^{o} to 1.8^{o}). The initial model was then low-pass filtered to 50 Å in RELION 2.1[176], which was used as a reference in subsequent 3D classification. One round of 3D classification (10 classes, C7 symmetry) was performed to identify a homogenous subset of particles. Two out of ten 3D classes showed densities consistent with TM α-helices. Class 6 displayed a larger diameter nanodisc compared with class 8 (**Figure 3.9c**). Angular distribution plot showed that the big-nanodisc 3D class contained dominant top views of particles, whereas the small-nanodisc 3D class displayed an even particle distribution of both top and side views. Thus, 46,450 particles in the small-nanodisc 3D class were subjected to another round of 2D classification (50 classes), resulting in 38,724 particles for

3D auto-refinement, applying C7 symmetry. The resolution of the auto-refined 3D map before post-processing (unmask) was 7.7 Å on the basis of the 0.143 gold-standard Fourier Shell Correlation (FSC). RELION post-processing, with application of a soft mask, improved the resolution of the final map to 7.0 Å, and the map was sharpened with a B-factor of -899 $Å^2$. Statistics for cryoEM data collection and image processing are summarized in Table 3.3.

3.3.6 Fitting of atomic structures

UCSF Chimera[191] was used to visualize the cryoEM density map. The map was segmented using the 'Segment map' function in in Chimera. The rigid body fitting of the atomic models of LRRC8A (Protein Data Bank (PDB) code: 6g8z) and INX-6 (PDB code: 5h1q) was performed using the 'Fit-in-map' function in Chimera. All molecular graphics were generated using UCSF Chimera.

3.3.7 Fluorescent thermal stability assay (FTSA)

The thermal stability of C-terminally truncated frog Panx1 (frPanx1 (1-357)) in detergent DDM/CHS was characterized using a cysteine-reactive, coumarin-based fluorophore, CPM (N-(4-(7-diethylamino-4-methyl-3-coumarinyl) phenyl) maleimide[174]. The quantum yield increases upon temperature-induced protein unfolding when CPM binds to cysteine residues within the hydrophobic region of a protein. The frPanx1 (1-357) contains 8 cysteine residues: 4 Cys in

the extracellular loops (EL) (C66 and C84 in EL1; C248 and C267 in EL2), 3 Cys in the transmembrane (TM) domains (C40 in TM1, C218 and C230 in TM3) and 1 Cys in the cytoplasmic loop (CL) (C149). The 3 Cys resides in the TM domains are predicted to be free cysteines that are maintained in a reduced state, which would be potentially accessible for binding to CPM as the protein is thermally denatured. When bound to a Cys thiol, the emission wavelength is 463 nm.

The CPM fluorescent dye (Invitrogen) in dimethylformamide was solubilized in SEC buffer (50 mM HEPES, pH 7.5, 500 mM NaCl, 3 mM $CaCl_2$ and 0.02% DDM with 0.004% CHS) to 13.3 µM and incubated with buffer on ice for 15 min. 10 µg of Panx1 was added to the buffer containing CPM fluorescent dye and incubated on ice for another 15 min. The temperature scan from 10-90 ^{o}C was performed using a FluoroMax-3 spectrofluorometer (Horiba Jobin-Yvon), with excitation and emission wavelengths of 387 nm and 463 nm, respectively. The fluorescence-temperature profile was analyzed using non-linear regression of a Boltzmann sigmoidal equation (Origin 7.5 software, OriginLab). The melting temperature (T_m) was calculated from the inflection point of the resulting melting curve as previously described[174].

3.3.8 Protein cross-linking

Purified frPanx1 (1-357) (1-2 mg ml^{-1} in buffer composed of 50 mM HEPES pH 7.5, 500 mM NaCl, 3 mM $CaCl_2$, 0.02% DDM with 0.004% CHS) was

cross-linked by 0.1% glutaraldehyde, a nonspecific cross-linker of amine-to-amine lysine residues. After 15 min incubation at room temperature, the reaction was terminated by addition of 100 mM Tris-HCl, pH 8.0. The cross-linking was confirmed by Coomassie blue stained SDS-PAGE and Western blot analysis using anti-Strep antibodies.

3.3.9 Deglycosylation assay

Purified frPanx1 (1-357) (2-3 mg ml^{-1} in buffer composed of 50 mM HEPES, pH 7.5, 500 mM NaCl, 3 mM $CaCl_2$ and 0.02% DDM) was incubated with 2000 units of N-glycosidase F (PNGase F) (New England BioLabs) at room temperature for 1 h. PNGase F was removed by SEC on a Superpose 6 increase 10/300 GL column (GE Healthcare) equilibrated with buffer (50 mM HEPES, pH 7.5, 500 mM NaCl, 3 mM $CaCl_2$ and 0.02% DDM). The SEC peak fractions corresponding to the deglycosylated Panx1 oligomer were collected and concentrated to ~1 mg ml^{-1} using a 0.5 ml concentrator with 100 kDa cut-off (EMD Millipore), for MALDI-MS and SEC-MALS analyses. Deglycosylation was confirmed by SDS-PAGE.

3.3.10 Matrix-assisted laser desorption mass spectrometry (MALDI-MS)

Purified frPanx1 (1-357) (~20 μM in buffer composed of 50 mM HEPES, pH 7.5, 500 mM NaCl, 3 mM $CaCl_2$ and 0.02% DDM) was mixed with an

aromatic carboxylic acid matrix, spotted onto the matrix-assisted laser desorption/ionization (MALDI) sample plate, and then loaded into the mass spectrometer. Matrix-assisted laser desorption/ionization mass spectrometry (MALDI-MS) analysis was performed by the Biomolecular Analysis Facility Core at the University of Virginia.

3.3.11 Size-exclusion chromatography with multi-angle light scattering (SEC-MALS)

SEC-MALS experiments were performed at room temperature using an HPLC system, equipped with a UV detector, a miniDAWN TREOS MALS detector and an Optilab T-rEX refractive index detector (Wyatt Technologies). An aliquot (~100 µg) of purified, deglycosylated frPanx1 (1-357) in buffer (50 mM HEPES, pH 7.5, 500 mM NaCl, 3 mM $CaCl_2$ and 0.02% DDM) was injected onto a Superdex 200 Increase 10/300 GL column (GE Healthcare), equilibrated with buffer (25 mM HEPES, pH 7.5, 150 mM NaCl, 3 mM $CaCl_2$ and 0.02% DDM). The data was analyzed using the Astra software (Astra 6.1, Wyatt Technologies) on the basis of the absorption at 280 nm, light scattering, and the differential refractive index. Extinction coefficients at 280 nm and *dn/dc* values for Panx1 were estimated to be 1.472 ml mg^{-1} cm^{-1} and 0.185 mol ml g^{-2}, respectively. The *dn/dc* value for DDM was assumed to be 0.133 mol ml g^{-2} [198]. The system was normalized using Bovine Serum Albumin (BSA, Sigma).

3.3.12 Mammalian cell culture and Electrophysiology *(from Dr. Yu-Hsin Chiu, University of Virginia)*

HEK293T cells (ATCC, passage 3-14) were cultured at 37 °C with humidified air containing 5% CO_2 in Dulbecco's Modified Eagle Medium (DMEM, Gibco) containing 10% fetal bovine serum (FBS, Gibco), penicillin, streptomycin, and sodium pyruvate. Transfection was carried out using Lipofectamine2000™ (Invitrogen) according to the protocol provided by manufacturer.

Whole-cell recordings were performed at room temperature using an Axopatch 200B amplifier and pCLAMP9 software (Molecular Devices). Ramp voltage commands were applied by using the pCLAMP9 software and a Digidata 1322A digitizer (Molecular Devices). Borosilicate glass patch pipettes of 3-5 megaohm were pulled by using a micropipette puller (Sutter Instruments, P-97) and then coated with Sylgard 184 silicone (Dow Corning). HEK293T cells were plated onto poly-lysine-coated coverslips after 16-18 h of transient transfection. The bath solution contained 10 mM HEPES, pH 7.3, 140 mM NaCl, 3 KCl, 2 mM $MgCl_2$, 2 mM $CaCl_2$ and 10 mM glucose. The pipette solution contained 10 mM HEPES, pH 7.3, 30 mM tetraethylammonium chloride, 100 mM cesium methanesulfonate, 4 mM NaCl, 1 mM $MgCl_2$, 0.5 mM $CaCl_2$, 10 mM EGTA, 3 mM ATP-Mg and 0.3 mM GTP-Tris. Carbenoxolone (CBX, 50 μM) was applied in bath solutions after acquisition of steady-state Panx1 activities. Phenylephrine (PE, 20 μM in the bath solution) was used to induce α1D adrenergic receptor-mediated activation of Panx1 channels[48,68,69]. Data were filtered at 1 kHz and

digitized at a sampling rate of 2 kHz. Data were analyzed using pCLAMP and GraphPad Prism softwares, and the results were presented as mean ± s.e.m.

Chapter 4

Conclusions and Future Directions

4.1 Summary and conclusions

In summary, by the use of a combination of different techniques from molecular biology, biochemistry, electron microscopy and electrophysiology, we performed a structure-function analysis of Panx1 channels.

We used negative-stain EM and electrophysiology to explore the conformational changes and pore structure, and channel property and activity associated with caspase cleavage-mediated activation. Coomassie Blue stained SDS-PAGE, Western immunoblot and MALDI-MS analyses suggested that purified Panx1 in detergent micelles or in amphipols can be efficiently cleaved *in vitro* by caspase-3. SEC and FTSA analyses showed that both full-length and caspase-cleaved human Panx1 channels in amphipols are homogenous and thermally stable. Negative-stain EM and single-particle image analysis revealed a striking decrease in density of the central pore of Panx1, which reflects a physical displacement of C-terminal tails from the channel pore. This observation structurally supports the hypothesis that the C-terminus acts as a pore-blocking plug to maintain Panx1 channel in an inactive state, and caspase cleavage allows the C-terminal tails to dissociate from the pore and activate the channel. Electrophysiological patch recordings showed that fully activated Panx1 channels

induced by caspase cleavage have an outwardly rectifying unitary conductance (<100 pS) that accounts for voltage dependence of Panx1 current, in contrast to the existing view that Panx1 is a voltage-dependent channel with large unitary conductance (~500 pS)[49]. Taken together, we find that Panx1 channels activated by caspase cleavage display a prominent 'pore', voltage-independent gating and an outwardly rectifying unitary conductance (<100 pS) at depolarized potentials. Our results support the model that caspase cleavage activates Panx1 channels by removing the C-terminal autoinhibitory region and provide critical views for interpretation of Panx1 channel property.

We used single-particle cryoEM and electrophysiology to investigate the structure and function of Panx1 channels. We extensively screened different Panx1 constructs, expression systems and purification conditions to optimize Panx1 samples for single-particle cryoEM analysis. Consequently, the C-terminally truncated frog Panx1 at residue 357, with a Thrombin cleavage site and a Strep tag at the truncated C-terminus, was expressed in *Sf9* insect cells, extracted and purified in the detergent DDM/CHS with addition of calcium, and exchanged to amphipols, or reconstituted into lipid nanodiscs, for single-particle cryoEM analysis. We reconstructed a three-dimensional cryoEM density map of the lipid nanodisc-embedded, C-terminally truncated frog Panx1 channels at 7 Å resolution. The 3D reconstruction reveals that Panx1 is a heptameric channel, with seven subunits surrounding a central seven-fold symmetric pore axis, in contrast to hexameric connexin and octameric innexin hemichannels. A large

entrance vestibule resides at the cytoplasmic surface, whereas the extracellular surface displays a narrow pore. Our cryoEM density map clearly resolves the transmembrane (TM) helices, which fold as a 4-helix bundle in each Panx1 subunit. Despite low sequence homology and different oligomeric states, the 4-helix bundle structure of Panx1 recapitulates a similar subunit design with other oligomeric, tetra-spanning membrane protein channels such as connexins, innexins and LRRC8 protein channels. Surprisingly, unlike the disordered cytoplasmic domains in connexin channels, the cytoplasmic domains of Panx1 are well-defined and form a dome-like structure of the channel, similarly to INX-6[47] and LRRC8A[139] channels. Rigid body fitting reveals that the monomeric structure of Panx1 resembles LRRC8A channel more than INX-6, which is consistent with the sequence alignment analysis that pannexins are evolutionary closer to LRRC8 proteins than innexins[37,134]. Calcium can significantly improve the stability and homogeneity of Panx1 channels, while the mechanisms such as calcium binding sites are still unclear. Electrophysiological recordings showed that the C-terminally truncated Panx1 channels are in a closed conformation, which can be activated by α1D adrenoceptor-mediated signaling pathway. As noted previously, Panx1 channels can be activated by caspase cleavage of the distal C-terminus for ATP release, which is an irreversible process[50,78]. Panx1 channels display a large cytoplasmic vesituble likely due to the truncated C-terminus, and adopt a closed conformation presumably by forming a constricted, narrow extracellular pore, maintaining the cells alive during protein expression, assembly, transport and insertion in the plasma membrane. This result suggests

that activation of the α1D adrenoceptor results in phosphorylation of a cytoplasmic site on Panx1 that elicits a transmembrane conformational change to open the extracellular gate. Our work reveals the previously unknown architecture of pannexin channels, providing insight into the structural basis of Panx1 channels such as oligomeric state (heptameric), channel and pore dimensions, arrangement of TM helices in each subunit and potential gating mechanism by extracellular domains.

4.2 Future directions

Our 3D reconstruction of Panx1 elicits a number of new questions regarding channel function and regulation: (1) what residues at the subunit-subunit interfaces dictate oligomeric states? (2) How are conformational changes coupled to channel opening or closing? (3) What are the characteristic residues and electrostatics of channel pore pathway, resulting in different channel properties of Panx1 (permeation of large molecule such as ATP, non-selective) and LRRC8A (permeation of small ion, anion-selective)? High-resolution structures of Panx1 channels in different functional states may answer these questions, and provide insight into several discrepancies regarding Panx1 channel property such as large unitary conductance (~300-500 pS) versus comparatively small unitary conductance (<100 pS), charge non-selective versus

anion selective, and voltage-dependent gating versus voltage-independent gating. The Panx1 cryoEM density map at subnanometer resolution does not allow us to accurately build an atomic model due to lack of side chain information or high sequence homology model; however, the established methods of preparing an optimal Panx1 sample for single-particle cryoEM analysis provide an important foundation for determination of a high-resolution structure. Chemical cross-linking of Panx1 (**Figure 4.1**), removal of a potentially disordered loop region in extracellular loop 1 (EL) or cytoplasmic loop (CL), or addition of protein antibodies such as Fab, may assist to decrease the conformational heterogeneity for high-resolution structure determination in the future. 3D reconstruction without imposing symmetry will also be pursued to further investigate potential channel regulation by subunits.

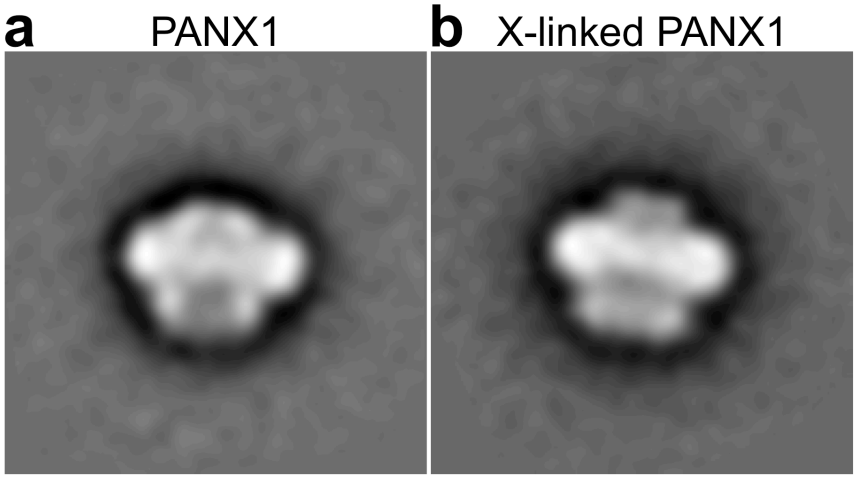

Figure 4.1. Negative-stain EM of Panx1 and X-linked Panx1 in lipid nanodiscs. Representative 2D class averages of negatively-stained Panx1 **(a)** and X-linked Panx1 **(b)** by 0.1% glutaradehyde, in lipid nanodiscs, with 826 and 806 particles, respectively. X-linked Panx1 showed more restricted structures in both cytoplasmic and extracellular regions. The particle box dimension is 357 Å.

Appendix: Chapter 3 Supplementary Figures

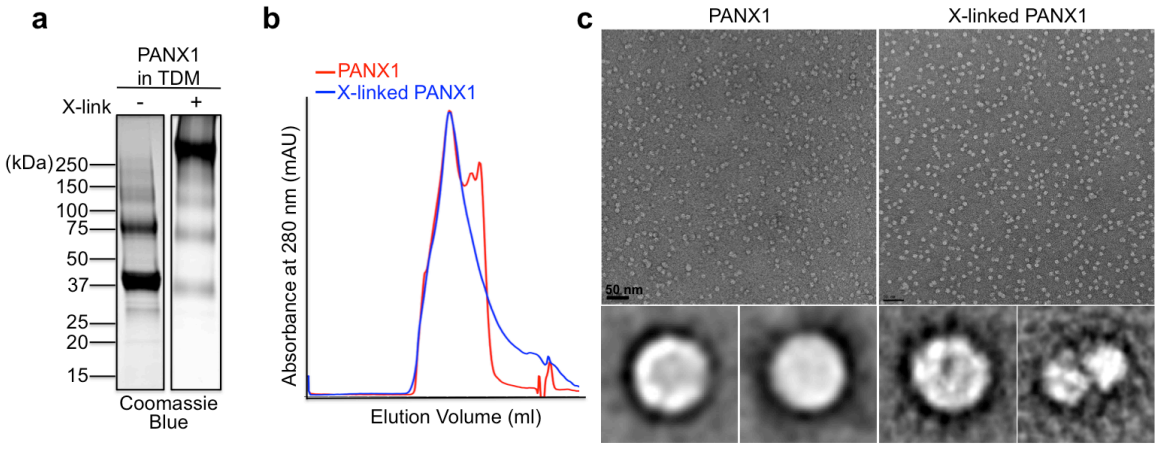

Supplementary Figure A1.1. Chemical cross-linking of full-length, human Panx1 reduced compositional heterogeneity. (a) Coomassie Blue stained SDS-PAGE showed monomeric Panx1, and oligomeric Panx1 cross-linked by 0.05% glutaradehyde. **(b)** SEC showed X-linked Panx1 (blue) was more homogenous with less dissociation compared to non X-linked Panx1 (red). **(c)** Negative-stain EM of Panx1 and X-linked Panx1. Top, raw particle eletron micrograph. Bottom, representative 2D class averages. Scale bar, 50 nm.

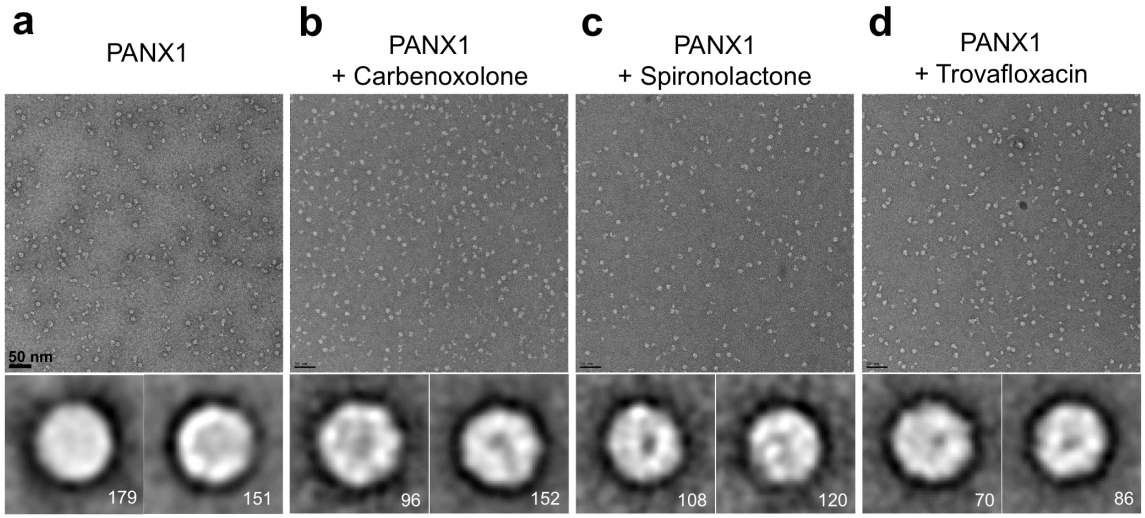

Supplementary Figure A1.2. Negative-stain EM of full-length, human Panx1 with treatment of inhibitors. Negative-stain EM of Panx1 **(a)** in amphipols, with treatment of inhibitors (100 μM) of carbenoxolone **(b)**, spironolactone **(c)** and trovafloxacin **(d)**. Top, raw particle EM image. Bottom, representative 2D class averages. Particle number in each class is indicated. Scale bar, 50 nm.

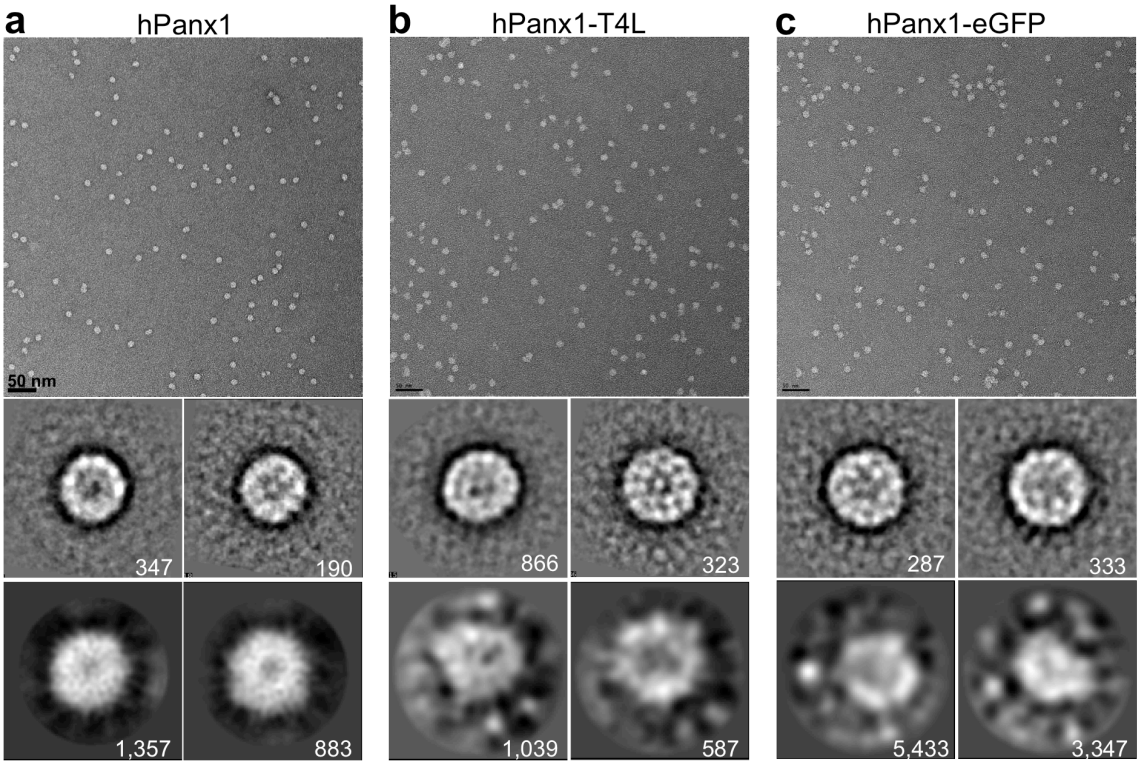

Supplementary Figure A1.3. Negative-stain EM of full-length, human Panx1 fusion proteins with T4L or eGFP. Negative-stain EM of Panx1 **(a)**, with T4L **(b)** and eGFP **(c)** fusion proteins. Top, raw particle negative-stain EM image. middle, representative 2D class averages of negatively-stained EM. Bottom, representative 2D class averages of cryoEM. Electron cryomicrographs were recorded using Falcon II direct detector of Titan Krios at UVA-MEMC. Particle number in each class is indicated. Scale bar, 50 nm.

References

1 Bruzzone, R., White, T. W. & Paul, D. L. Connections with connexins: the molecular basis of direct intercellular signaling. *Eur J Biochem* **238**, 1-27 (1996).

2 Kumar, N. M. & Gilula, N. B. The gap junction communication channel. *Cell* **84**, 381-388 (1996).

3 Evans, W. H. & Martin, P. E. Gap junctions: structure and function (Review). *Mol Membr Biol* **19**, 121-136, doi:10.1080/09687680210139839 (2002).

4 Scemes, E., Suadicani, S. O., Dahl, G. & Spray, D. C. Connexin and pannexin mediated cell-cell communication. *Neuron Glia Biol* **3**, 199-208, doi:10.1017/S1740925X08000069 (2007).

5 Rackauskas, M., Neverauskas, V. & Skeberdis, V. A. Diversity and properties of connexin gap junction channels. *Medicina (Kaunas)* **46**, 1-12 (2010).

6 Nielsen, M. S. *et al.* Gap junctions. *Compr Physiol* **2**, 1981-2035, doi:10.1002/cphy.c110051 (2012).

7 Phelan, P. *et al.* Innexins: a family of invertebrate gap-junction proteins. *Trends Genet* **14**, 348-349 (1998).

8 Phelan, P. & Starich, T. A. Innexins get into the gap. *Bioessays* **23**, 388-396, doi:10.1002/bies.1057 (2001).

9 Phelan, P. Innexins: members of an evolutionarily conserved family of gap-junction proteins. *Biochim Biophys Acta* **1711**, 225-245, doi:10.1016/j.bbamem.2004.10.004 (2005).

10 Panchin, Y. V. Evolution of gap junction proteins--the pannexin alternative. *J Exp Biol* **208**, 1415-1419, doi:10.1242/jeb.01547 (2005).

11 Skerrett, I. M. & Williams, J. B. A structural and functional comparison of gap junction channels composed of connexins and innexins. *Dev Neurobiol* **77**, 522-547, doi:10.1002/dneu.22447 (2017).

12 Panchin, Y. *et al.* A ubiquitous family of putative gap junction molecules. *Curr Biol* **10**, R473-474 (2000).

13 Baranova, A. *et al.* The mammalian pannexin family is homologous to the invertebrate innexin gap junction proteins. *Genomics* **83**, 706-716, doi:10.1016/j.ygeno.2003.09.025 (2004).

14 Shestopalov, V. I. & Panchin, Y. Pannexins and gap junction protein diversity. *Cell Mol Life Sci* **65**, 376-394, doi:10.1007/s00018-007-7200-1 (2008).

15 Fushiki, D., Hamada, Y., Yoshimura, R. & Endo, Y. Phylogenetic and bioinformatic analysis of gap junction-related proteins, innexins, pannexins and connexins. *Biomed Res* **31**, 133-142 (2010).

16 Scemes, E., Spray, D. C. & Meda, P. Connexins, pannexins, innexins: novel roles of "hemi-channels". *Pflugers Arch* **457**, 1207-1226, doi:10.1007/s00424-008-0591-5 (2009).

17 Bond, S. R. & Naus, C. C. The pannexins: past and present. *Front Physiol* **5**, 58, doi:10.3389/fphys.2014.00058 (2014).
18 Dahl, G., Qiu, F. & Wang, J. The bizarre pharmacology of the ATP release channel pannexin1. *Neuropharmacology*, doi:10.1016/j.neuropharm.2013.02.019 (2013).
19 Bruzzone, R., Hormuzdi, S. G., Barbe, M. T., Herb, A. & Monyer, H. Pannexins, a family of gap junction proteins expressed in brain. *Proc Natl Acad Sci U S A* **100**, 13644-13649, doi:10.1073/pnas.2233464100 (2003).
20 Lai, C. P. *et al.* Tumor-suppressive effects of pannexin 1 in C6 glioma cells. *Cancer Res* **67**, 1545-1554, doi:10.1158/0008-5472.CAN-06-1396 (2007).
21 Dahl, G. & Locovei, S. Pannexin: to gap or not to gap, is that a question? *IUBMB Life* **58**, 409-419, doi:10.1080/15216540600794526 (2006).
22 Dahl, G. & Keane, R. W. Pannexin: from discovery to bedside in 11±4 years? *Brain Res* **1487**, 150-159, doi:10.1016/j.brainres.2012.04.058 (2012).
23 Sosinsky, G. E. *et al.* Pannexin channels are not gap junction hemichannels. *Channels (Austin)* **5**, 193-197 (2011).
24 Locovei, S., Bao, L. & Dahl, G. Pannexin 1 in erythrocytes: function without a gap. *Proc Natl Acad Sci U S A* **103**, 7655-7659, doi:10.1073/pnas.0601037103 (2006).
25 Ransford, G. A. *et al.* Pannexin 1 contributes to ATP release in airway epithelia. *Am J Respir Cell Mol Biol* **41**, 525-534, doi:10.1165/rcmb.2008-0367OC (2009).
26 Hanner, F., Lam, L., Nguyen, M. T., Yu, A. & Peti-Peterdi, J. Intrarenal localization of the plasma membrane ATP channel pannexin1. *Am J Physiol Renal Physiol* **303**, F1454-1459, doi:10.1152/ajprenal.00206.2011 (2012).
27 Zoidl, G. *et al.* Localization of the pannexin1 protein at postsynaptic sites in the cerebral cortex and hippocampus. *Neuroscience* **146**, 9-16, doi:10.1016/j.neuroscience.2007.01.061 (2007).
28 Dolmatova, E. *et al.* Cardiomyocyte ATP release through pannexin 1 aids in early fibroblast activation. *Am J Physiol Heart Circ Physiol* **303**, H1208-1218, doi:10.1152/ajpheart.00251.2012 (2012).
29 Foote, C. I., Zhou, L., Zhu, X. & Nicholson, B. J. The pattern of disulfide linkages in the extracellular loop regions of connexin 32 suggests a model for the docking interface of gap junctions. *J Cell Biol* **140**, 1187-1197 (1998).
30 Boassa, D. *et al.* Pannexin1 channels contain a glycosylation site that targets the hexamer to the plasma membrane. *J Biol Chem* **282**, 31733-31743, doi:10.1074/jbc.M702422200 (2007).
31 Boassa, D., Qiu, F., Dahl, G. & Sosinsky, G. Trafficking dynamics of glycosylated pannexin 1 proteins. *Cell Commun Adhes* **15**, 119-132, doi:10.1080/15419060802013885 (2008).
32 Penuela, S. *et al.* Pannexin 1 and pannexin 3 are glycoproteins that exhibit many distinct characteristics from the connexin family of gap

junction proteins. *J Cell Sci* **120**, 3772-3783, doi:10.1242/jcs.009514 (2007).

33 Bruzzone, R., Barbe, M. T., Jakob, N. J. & Monyer, H. Pharmacological properties of homomeric and heteromeric pannexin hemichannels expressed in Xenopus oocytes. *J Neurochem* **92**, 1033-1043, doi:10.1111/j.1471-4159.2004.02947.x (2005).

34 Locovei, S., Wang, J. & Dahl, G. Activation of pannexin 1 channels by ATP through P2Y receptors and by cytoplasmic calcium. *FEBS Lett* **580**, 239-244, doi:10.1016/j.febslet.2005.12.004 (2006).

35 Penuela, S., Gehi, R. & Laird, D. W. The biochemistry and function of pannexin channels. *Biochim Biophys Acta* **1828**, 15-22, doi:10.1016/j.bbamem.2012.01.017 (2013).

36 Penuela, S., Bhalla, R., Nag, K. & Laird, D. W. Glycosylation regulates pannexin intermixing and cellular localization. *Mol Biol Cell* **20**, 4313-4323, doi:10.1091/mbc.E09-01-0067 (2009).

37 Abascal, F. & Zardoya, R. Evolutionary analyses of gap junction protein families. *Biochim Biophys Acta* **1828**, 4-14, doi:10.1016/j.bbamem.2012.02.007 (2013).

38 Yen, M. R. & Saier, M. H. Gap junctional proteins of animals: the innexin/pannexin superfamily. *Prog Biophys Mol Biol* **94**, 5-14, doi:10.1016/j.pbiomolbio.2007.03.006 (2007).

39 Spagnol, G., Sorgen, P. L. & Spray, D. C. Structural order in Pannexin 1 cytoplasmic domains. *Channels (Austin)* **8** (2014).

40 Wang, J. & Dahl, G. SCAM analysis of Panx1 suggests a peculiar pore structure. *J Gen Physiol* **136**, 515-527, doi:10.1085/jgp.201010440 (2010).

41 Ambrosi, C. *et al.* Pannexin1 and Pannexin2 channels show quaternary similarities to connexons and different oligomerization numbers from each other. *J Biol Chem* **285**, 24420-24431, doi:10.1074/jbc.M110.115444 (2010).

42 Bunse, S. *et al.* Single cysteines in the extracellular and transmembrane regions modulate pannexin 1 channel function. *J Membr Biol* **244**, 21-33, doi:10.1007/s00232-011-9393-3 (2011).

43 Unger, V. M., Kumar, N. M., Gilula, N. B. & Yeager, M. Three-dimensional structure of a recombinant gap junction membrane channel. *Science* **283**, 1176-1180 (1999).

44 Maeda, S. *et al.* Structure of the connexin 26 gap junction channel at 3.5 A resolution. *Nature* **458**, 597-602, doi:10.1038/nature07869 (2009).

45 Bennett, B. C. *et al.* An electrostatic mechanism for Ca(2+)-mediated regulation of gap junction channels. *Nat Commun* **7**, 8770, doi:10.1038/ncomms9770 (2016).

46 Oshima, A., Matsuzawa, T., Murata, K., Tani, K. & Fujiyoshi, Y. Hexadecameric structure of an invertebrate gap junction channel. *J Mol Biol* **428**, 1227-1236, doi:10.1016/j.jmb.2016.02.011 (2016).

47 Oshima, A., Tani, K. & Fujiyoshi, Y. Atomic structure of the innexin-6 gap junction channel determined by cryo-EM. *Nat Commun* **7**, 13681, doi:10.1038/ncomms13681 (2016).

48 Chiu, Y. H. *et al.* A quantized mechanism for activation of pannexin channels. *Nat Commun* **8**, 14324, doi:10.1038/ncomms14324 (2017).
49 Bao, L., Locovei, S. & Dahl, G. Pannexin membrane channels are mechanosensitive conduits for ATP. *FEBS Lett* **572**, 65-68, doi:10.1016/j.febslet.2004.07.009 (2004).
50 Chekeni, F. B. *et al.* Pannexin 1 channels mediate 'find-me' signal release and membrane permeability during apoptosis. *Nature* **467**, 863-867, doi:10.1038/nature09413 (2010).
51 Ma, W. *et al.* Pannexin 1 forms an anion-selective channel. *Pflugers Arch* **463**, 585-592, doi:10.1007/s00424-012-1077-z (2012).
52 Romanov, R. A. *et al.* The ATP permeability of pannexin 1 channels in a heterologous system and in mammalian taste cells is dispensable. *J Cell Sci* **125**, 5514-5523, doi:10.1242/jcs.111062 (2012).
53 Duan, S., Anderson, C. M., Keung, E. C., Chen, Y. & Swanson, R. A. P2X7 receptor-mediated release of excitatory amino acids from astrocytes. *J Neurosci* **23**, 1320-1328 (2003).
54 Jiang, H. *et al.* Stimulation of rat erythrocyte P2X7 receptor induces the release of epoxyeicosatrienoic acids. *Br J Pharmacol* **151**, 1033-1040, doi:10.1038/sj.bjp.0707311 (2007).
55 Pelegrin, P. & Surprenant, A. Pannexin-1 mediates large pore formation and interleukin-1beta release by the ATP-gated P2X7 receptor. *EMBO J* **25**, 5071-5082, doi:10.1038/sj.emboj.7601378 (2006).
56 Thompson, R. J., Zhou, N. & MacVicar, B. A. Ischemia opens neuronal gap junction hemichannels. *Science* **312**, 924-927, doi:10.1126/science.1126241 (2006).
57 Kienitz, M. C., Bender, K., Dermietzel, R., Pott, L. & Zoidl, G. Pannexin 1 constitutes the large conductance cation channel of cardiac myocytes. *J Biol Chem* **286**, 290-298, doi:10.1074/jbc.M110.163477 (2011).
58 Wang, J. *et al.* The membrane protein Pannexin1 forms two open-channel conformations depending on the mode of activation. *Sci Signal* **7**, ra69, doi:10.1126/scisignal.2005431 (2014).
59 Seminario-Vidal, L. *et al.* Rho signaling regulates pannexin 1-mediated ATP release from airway epithelia. *J Biol Chem* **286**, 26277-26286, doi:10.1074/jbc.M111.260562 (2011).
60 Ma, W., Hui, H., Pelegrin, P. & Surprenant, A. Pharmacological characterization of pannexin-1 currents expressed in mammalian cells. *J Pharmacol Exp Ther* **328**, 409-418, doi:10.1124/jpet.108.146365 (2009).
61 Silverman, W. R. *et al.* The pannexin 1 channel activates the inflammasome in neurons and astrocytes. *J Biol Chem* **284**, 18143-18151, doi:10.1074/jbc.M109.004804 (2009).
62 Qiu, F., Wang, J., Spray, D. C., Scemes, E. & Dahl, G. Two non-vesicular ATP release pathways in the mouse erythrocyte membrane. *FEBS Lett* **585**, 3430-3435, doi:10.1016/j.febslet.2011.09.033 (2011).
63 Santiago, M. F. *et al.* Targeting pannexin1 improves seizure outcome. *PLoS One* **6**, e25178, doi:10.1371/journal.pone.0025178 (2011).

64 Suadicani, S. O. *et al.* ATP signaling is deficient in cultured Pannexin1-null mouse astrocytes. *Glia* **60**, 1106-1116, doi:10.1002/glia.22338 (2012).

65 Wang, J., Jackson, D. G. & Dahl, G. Cationic control of Panx1 channel function. *Am J Physiol Cell Physiol*, doi:10.1152/ajpcell.00303.2017 (2018).

66 Seminario-Vidal, L. *et al.* Thrombin promotes release of ATP from lung epithelial cells through coordinated activation of rho- and Ca2+-dependent signaling pathways. *J Biol Chem* **284**, 20638-20648, doi:10.1074/jbc.M109.004762 (2009).

67 Gödecke, S. *et al.* Thrombin-induced ATP release from human umbilical vein endothelial cells. *Am J Physiol Cell Physiol* **302**, C915-923, doi:10.1152/ajpcell.00283.2010 (2012).

68 Billaud, M. *et al.* Pannexin1 regulates α1-adrenergic receptor- mediated vasoconstriction. *Circ Res* **109**, 80-85, doi:10.1161/CIRCRESAHA.110.237594 (2011).

69 Billaud, M. *et al.* A molecular signature in the pannexin1 intracellular loop confers channel activation by the α1 adrenoreceptor in smooth muscle cells. *Sci Signal* **8**, ra17, doi:10.1126/scisignal.2005824 (2015).

70 Blum, A. E., Joseph, S. M., Przybylski, R. J. & Dubyak, G. R. Rho-family GTPases modulate Ca(2+) -dependent ATP release from astrocytes. *Am J Physiol Cell Physiol* **295**, C231-241, doi:10.1152/ajpcell.00175.2008 (2008).

71 Iglesias, R. *et al.* P2X7 receptor-Pannexin1 complex: pharmacology and signaling. *Am J Physiol Cell Physiol* **295**, C752-760, doi:10.1152/ajpcell.00228.2008 (2008).

72 Thompson, R. J. *et al.* Activation of pannexin-1 hemichannels augments aberrant bursting in the hippocampus. *Science* **322**, 1555-1559, doi:10.1126/science.1165209 (2008).

73 Weilinger, N. L., Tang, P. L. & Thompson, R. J. Anoxia-induced NMDA receptor activation opens pannexin channels via Src family kinases. *J Neurosci* **32**, 12579-12588, doi:10.1523/JNEUROSCI.1267-12.2012 (2012).

74 Weilinger, N. L. *et al.* Metabotropic NMDA receptor signaling couples Src family kinases to pannexin-1 during excitotoxicity. *Nat Neurosci* **19**, 432-442, doi:10.1038/nn.4236 (2016).

75 Adamson, S. E. *et al.* Pannexin 1 is required for full activation of insulin-stimulated glucose uptake in adipocytes. *Mol Metab* **4**, 610-618, doi:10.1016/j.molmet.2015.06.009 (2015).

76 Velasquez, S., Malik, S., Lutz, S. E., Scemes, E. & Eugenin, E. A. Pannexin1 Channels Are Required for Chemokine-Mediated Migration of CD4+ T Lymphocytes: Role in Inflammation and Experimental Autoimmune Encephalomyelitis. *J Immunol* **196**, 4338-4347, doi:10.4049/jimmunol.1502440 (2016).

77 Qu, Y. *et al.* Pannexin-1 is required for ATP release during apoptosis but not for inflammasome activation. *J Immunol* **186**, 6553-6561, doi:10.4049/jimmunol.1100478 (2011).

78 Sandilos, J. K. *et al.* Pannexin 1, an ATP release channel, is activated by caspase cleavage of its pore-associated C-terminal autoinhibitory region. *J Biol Chem* **287**, 11303-11311, doi:10.1074/jbc.M111.323378 (2012).
79 Yang, D., He, Y., Muñoz-Planillo, R., Liu, Q. & Núñez, G. Caspase-11 Requires the Pannexin-1 Channel and the Purinergic P2X7 Pore to Mediate Pyroptosis and Endotoxic Shock. *Immunity* **43**, 923-932, doi:10.1016/j.immuni.2015.10.009 (2015).
80 Sandilos, J. K. & Bayliss, D. A. Physiological mechanisms for the modulation of pannexin 1 channel activity. *J Physiol* **590**, 6257-6266, doi:10.1113/jphysiol.2012.240911 (2012).
81 Armstrong, C. M. & Bezanilla, F. Inactivation of the sodium channel. II. Gating current experiments. *J Gen Physiol* **70**, 567-590 (1977).
82 Hoshi, T., Zagotta, W. N. & Aldrich, R. W. Biophysical and molecular mechanisms of Shaker potassium channel inactivation. *Science* **250**, 533-538 (1990).
83 Morley, G. E., Taffet, S. M. & Delmar, M. Intramolecular interactions mediate pH regulation of connexin43 channels. *Biophys J* **70**, 1294-1302, doi:10.1016/S0006-3495(96)79686-8 (1996).
84 Homma, N. *et al.* A particle-receptor model for the insulin-induced closure of connexin43 channels. *Circ Res* **83**, 27-32 (1998).
85 Moreno, A. P. *et al.* Role of the carboxyl terminal of connexin43 in transjunctional fast voltage gating. *Circ Res* **90**, 450-457 (2002).
86 Duffy, H. S. *et al.* pH-dependent intramolecular binding and structure involving Cx43 cytoplasmic domains. *J Biol Chem* **277**, 36706-36714, doi:10.1074/jbc.M207016200 (2002).
87 Delmar, M., Coombs, W., Sorgen, P., Duffy, H. S. & Taffet, S. M. Structural bases for the chemical regulation of Connexin43 channels. *Cardiovasc Res* **62**, 268-275, doi:10.1016/j.cardiores.2003.12.030 (2004).
88 Billaud, M., Sandilos, J. K. & Isakson, B. E. Pannexin 1 in the regulation of vascular tone. *Trends Cardiovasc Med* **22**, 68-72, doi:10.1016/j.tcm.2012.06.014 (2012).
89 Kurtenbach, S. *et al.* Pannexin1 channel proteins in the zebrafish retina have shared and unique properties. *PLoS One* **8**, e77722, doi:10.1371/journal.pone.0077722 (2013).
90 Qiu, F. & Dahl, G. A permeant regulating its permeation pore: inhibition of pannexin 1 channels by ATP. *Am J Physiol Cell Physiol* **296**, C250-255, doi:10.1152/ajpcell.00433.2008 (2009).
91 Bunse, S. *et al.* The potassium channel subunit Kvbeta3 interacts with pannexin 1 and attenuates its sensitivity to changes in redox potentials. *FEBS J* **276**, 6258-6270, doi:10.1111/j.1742-4658.2009.07334.x (2009).
92 Bunse, S., Schmidt, M., Prochnow, N., Zoidl, G. & Dermietzel, R. Intracellular cysteine 346 is essentially involved in regulating Panx1 channel activity. *J Biol Chem* **285**, 38444-38452, doi:10.1074/jbc.M110.101014 (2010).
93 Lohman, A. W. *et al.* S-nitrosylation inhibits pannexin 1 channel function. *J Biol Chem* **287**, 39602-39612, doi:10.1074/jbc.M112.397976 (2012).

94 Samuels, S. E., Lipitz, J. B., Wang, J., Dahl, G. & Muller, K. J. Arachidonic acid closes innexin/pannexin channels and thereby inhibits microglia cell movement to a nerve injury. *Dev Neurobiol* **73**, 621-631, doi:10.1002/dneu.22088 (2013).
95 Wang, J., Ma, M., Locovei, S., Keane, R. W. & Dahl, G. Modulation of membrane channel currents by gap junction protein mimetic peptides: size matters. *Am J Physiol Cell Physiol* **293**, C1112-1119, doi:10.1152/ajpcell.00097.2007 (2007).
96 Silverman, W., Locovei, S. & Dahl, G. Probenecid, a gout remedy, inhibits pannexin 1 channels. *Am J Physiol Cell Physiol* **295**, C761-767, doi:10.1152/ajpcell.00227.2008 (2008).
97 Iglesias, R., Spray, D. C. & Scemes, E. Mefloquine blockade of Pannexin1 currents: resolution of a conflict. *Cell Commun Adhes* **16**, 131-137, doi:10.3109/15419061003642618 (2009).
98 Wang, J., Jackson, D. G. & Dahl, G. The food dye FD&C Blue No. 1 is a selective inhibitor of the ATP release channel Panx1. *J Gen Physiol* **141**, 649-656, doi:10.1085/jgp.201310966 (2013).
99 Poon, I. K. *et al.* Unexpected link between an antibiotic, pannexin channels and apoptosis. *Nature* **507**, 329-334, doi:10.1038/nature13147 (2014).
100 Boyce, A. K. J., Epp, A. L., Nagarajan, A. & Swayne, L. A. Transcriptional and post-translational regulation of pannexins. *Biochim Biophys Acta* **1860**, 72-82, doi:10.1016/j.bbamem.2017.03.004 (2018).
101 Begandt, D. *et al.* Pannexin channel and connexin hemichannel expression in vascular function and inflammation. *BMC Cell Biol* **18**, 2, doi:10.1186/s12860-016-0119-3 (2017).
102 Lohman, A. W. *et al.* Pannexin 1 channels regulate leukocyte emigration through the venous endothelium during acute inflammation. *Nat Commun* **6**, 7965, doi:10.1038/ncomms8965 (2015).
103 Xiao, F., Waldrop, S. L., Khimji, A. K. & Kilic, G. Pannexin1 contributes to pathophysiological ATP release in lipoapoptosis induced by saturated free fatty acids in liver cells. *Am J Physiol Cell Physiol* **303**, C1034-1044, doi:10.1152/ajpcell.00175.2012 (2012).
104 Poornima, V., Vallabhaneni, S., Mukhopadhyay, M. & Bera, A. K. Nitric oxide inhibits the pannexin 1 channel through a cGMP-PKG dependent pathway. *Nitric Oxide* **47**, 77-84, doi:10.1016/j.niox.2015.04.005 (2015).
105 Dahl, G. ATP release through pannexon channels. *Philos Trans R Soc Lond B Biol Sci* **370**, doi:10.1098/rstb.2014.0191 (2015).
106 Taruno, A. ATP Release Channels. *Int J Mol Sci* **19**, doi:10.3390/ijms19030808 (2018).
107 Sridharan, M. *et al.* Pannexin 1 is the conduit for low oxygen tension-induced ATP release from human erythrocytes. *Am J Physiol Heart Circ Physiol* **299**, H1146-1152, doi:10.1152/ajpheart.00301.2010 (2010).
108 Kawamura, M., Ruskin, D. N. & Masino, S. A. Metabolic autocrine regulation of neurons involves cooperation among pannexin hemichannels,

adenosine receptors, and KATP channels. *J Neurosci* **30**, 3886-3895, doi:10.1523/JNEUROSCI.0055-10.2010 (2010).

109 Iglesias, R., Dahl, G., Qiu, F., Spray, D. C. & Scemes, E. Pannexin 1: the molecular substrate of astrocyte "hemichannels". *J Neurosci* **29**, 7092-7097, doi:10.1523/JNEUROSCI.6062-08.2009 (2009).

110 Iwabuchi, S. & Kawahara, K. Functional significance of the negative-feedback regulation of ATP release via pannexin-1 hemichannels under ischemic stress in astrocytes. *Neurochem Int* **58**, 376-384, doi:10.1016/j.neuint.2010.12.013 (2011).

111 Huang, Y. J. *et al.* The role of pannexin 1 hemichannels in ATP release and cell-cell communication in mouse taste buds. *Proc Natl Acad Sci U S A* **104**, 6436-6441, doi:10.1073/pnas.0611280104 (2007).

112 Dando, R. & Roper, S. D. Cell-to-cell communication in intact taste buds through ATP signalling from pannexin 1 gap junction hemichannels. *J Physiol* **587**, 5899-5906, doi:10.1113/jphysiol.2009.180083 (2009).

113 Woehrle, T. *et al.* Hypertonic stress regulates T cell function via pannexin-1 hemichannels and P2X receptors. *J Leukoc Biol* **88**, 1181-1189, doi:10.1189/jlb.0410211 (2010).

114 Woehrle, T. *et al.* Pannexin-1 hemichannel-mediated ATP release together with P2X1 and P2X4 receptors regulate T-cell activation at the immune synapse. *Blood* **116**, 3475-3484, doi:10.1182/blood-2010-04-277707 (2010).

115 Schenk, U. *et al.* Purinergic control of T cell activation by ATP released through pannexin-1 hemichannels. *Sci Signal* **1**, ra6, doi:10.1126/scisignal.1160583 (2008).

116 Vandenbeuch, A., Anderson, C. B. & Kinnamon, S. C. Mice Lacking Pannexin 1 Release ATP and Respond Normally to All Taste Qualities. *Chem Senses* **40**, 461-467, doi:10.1093/chemse/bjv034 (2015).

117 Tordoff, M. G. *et al.* Normal Taste Acceptance and Preference of PANX1 Knockout Mice. *Chem Senses* **40**, 453-459, doi:10.1093/chemse/bjv025 (2015).

118 Taruno, A. *et al.* CALHM1 ion channel mediates purinergic neurotransmission of sweet, bitter and umami tastes. *Nature* **495**, 223-226, doi:10.1038/nature11906 (2013).

119 Poon, I. K., Lucas, C. D., Rossi, A. G. & Ravichandran, K. S. Apoptotic cell clearance: basic biology and therapeutic potential. *Nat Rev Immunol* **14**, 166-180, doi:10.1038/nri3607 (2014).

120 Kanneganti, T. D. *et al.* Pannexin-1-mediated recognition of bacterial molecules activates the cryopyrin inflammasome independent of Toll-like receptor signaling. *Immunity* **26**, 433-443, doi:10.1016/j.immuni.2007.03.008 (2007).

121 Séror, C. *et al.* Extracellular ATP acts on P2Y2 purinergic receptors to facilitate HIV-1 infection. *J Exp Med* **208**, 1823-1834, doi:10.1084/jem.20101805 (2011).

122 Orellana, J. A. *et al.* Pannexin1 hemichannels are critical for HIV infection of human primary CD4+ T lymphocytes. *J Leukoc Biol* **94**, 399-407, doi:10.1189/jlb.0512249 (2013).
123 Katsura, K., Kristián, T. & Siesjö, B. K. Energy metabolism, ion homeostasis, and cell damage in the brain. *Biochem Soc Trans* **22**, 991-996 (1994).
124 Martin, R. L., Lloyd, H. G. & Cowan, A. I. The early events of oxygen and glucose deprivation: setting the scene for neuronal death? *Trends Neurosci* **17**, 251-257 (1994).
125 Dirnagl, U., Iadecola, C. & Moskowitz, M. A. Pathobiology of ischaemic stroke: an integrated view. *Trends Neurosci* **22**, 391-397 (1999).
126 Gulbransen, B. D. *et al.* Activation of neuronal P2X7 receptor-pannexin-1 mediates death of enteric neurons during colitis. *Nat Med* **18**, 600-604, doi:10.1038/nm.2679 (2012).
127 Karatas, H. *et al.* Spreading depression triggers headache by activating neuronal Panx1 channels. *Science* **339**, 1092-1095, doi:10.1126/science.1231897 (2013).
128 Vessey, D. A., Li, L. & Kelley, M. Pannexin-I/P2X 7 purinergic receptor channels mediate the release of cardioprotectants induced by ischemic pre- and postconditioning. *J Cardiovasc Pharmacol Ther* **15**, 190-195, doi:10.1177/1074248409360356 (2010).
129 Vessey, D. A., Li, L. & Kelley, M. Ischemic preconditioning requires opening of pannexin-1/P2X(7) channels not only during preconditioning but again after index ischemia at full reperfusion. *Mol Cell Biochem* **351**, 77-84, doi:10.1007/s11010-011-0713-9 (2011).
130 Nishida, M. *et al.* P2Y6 receptor-Galpha12/13 signalling in cardiomyocytes triggers pressure overload-induced cardiac fibrosis. *EMBO J* **27**, 3104-3115, doi:10.1038/emboj.2008.237 (2008).
131 Penuela, S. *et al.* Loss of pannexin 1 attenuates melanoma progression by reversion to a melanocytic phenotype. *J Biol Chem* **287**, 29184-29193, doi:10.1074/jbc.M112.377176 (2012).
132 Furlow, P. W. *et al.* Mechanosensitive pannexin-1 channels mediate microvascular metastatic cell survival. *Nat Cell Biol* **17**, 943-952, doi:10.1038/ncb3194 (2015).
133 Xiong, X. X. *et al.* Probenecid protects against transient focal cerebral ischemic injury by inhibiting HMGB1 release and attenuating AQP4 expression in mice. *Neurochem Res* **39**, 216-224, doi:10.1007/s11064-013-1212-z (2014).
134 Abascal, F. & Zardoya, R. LRRC8 proteins share a common ancestor with pannexins, and may form hexameric channels involved in cell-cell communication. *Bioessays* **34**, 551-560, doi:10.1002/bies.201100173 (2012).
135 Voss, F. K. *et al.* Identification of LRRC8 heteromers as an essential component of the volume-regulated anion channel VRAC. *Science* **344**, 634-638, doi:10.1126/science.1252826 (2014).

136 Qiu, Z. *et al.* SWELL1, a plasma membrane protein, is an essential component of volume-regulated anion channel. *Cell* **157**, 447-458, doi:10.1016/j.cell.2014.03.024 (2014).
137 Siebert, A. P. *et al.* Structural and functional similarities of calcium homeostasis modulator 1 (CALHM1) ion channel with connexins, pannexins, and innexins. *J Biol Chem* **288**, 6140-6153, doi:10.1074/jbc.M112.409789 (2013).
138 Ma, Z. *et al.* Calcium homeostasis modulator 1 (CALHM1) is the pore-forming subunit of an ion channel that mediates extracellular Ca2+ regulation of neuronal excitability. *Proc Natl Acad Sci U S A* **109**, E1963-1971, doi:10.1073/pnas.1204023109 (2012).
139 Deneka, D., Sawicka, M., Lam, A. K. M., Paulino, C. & Dutzler, R. Structure of a volume-regulated anion channel of the LRRC8 family. *Nature*, doi:10.1038/s41586-018-0134-y (2018).
140 Willecke, K. *et al.* Structural and functional diversity of connexin genes in the mouse and human genome. *Biol Chem* **383**, 725-737, doi:10.1515/BC.2002.076 (2002).
141 Gerido, D. A. & White, T. W. Connexin disorders of the ear, skin, and lens. *Biochim Biophys Acta* **1662**, 159-170, doi:10.1016/j.bbamem.2003.10.017 (2004).
142 Martínez, A. D., Acuña, R., Figueroa, V., Maripillan, J. & Nicholson, B. Gap-junction channels dysfunction in deafness and hearing loss. *Antioxid Redox Signal* **11**, 309-322, doi:10.1089/ars.2008.2138 (2009).
143 Wingard, J. C. & Zhao, H. B. Cellular and Deafness Mechanisms Underlying Connexin Mutation-Induced Hearing Loss - A Common Hereditary Deafness. *Front Cell Neurosci* **9**, 202, doi:10.3389/fncel.2015.00202 (2015).
144 Lee, J. R. & White, T. W. Connexin-26 mutations in deafness and skin disease. *Expert Rev Mol Med* **11**, e35, doi:10.1017/S1462399409001276 (2009).
145 Richard, G. Connexins: a connection with the skin. *Exp Dermatol* **9**, 77-96 (2000).
146 Beyer, E. C., Ebihara, L. & Berthoud, V. M. Connexin mutants and cataracts. *Front Pharmacol* **4**, 43, doi:10.3389/fphar.2013.00043 (2013).
147 Paznekas, W. A. *et al.* Connexin 43 (GJA1) mutations cause the pleiotropic phenotype of oculodentodigital dysplasia. *Am J Hum Genet* **72**, 408-418, doi:10.1086/346090 (2003).
148 Bergoffen, J. *et al.* Connexin mutations in X-linked Charcot-Marie-Tooth disease. *Science* **262**, 2039-2042 (1993).
149 Unwin, P. N. & Zampighi, G. Structure of the junction between communicating cells. *Nature* **283**, 545-549 (1980).
150 Unwin, P. N. & Ennis, P. D. Two configurations of a channel-forming membrane protein. *Nature* **307**, 609-613 (1984).
151 Oshima, A., Tani, K., Hiroaki, Y., Fujiyoshi, Y. & Sosinsky, G. E. Three-dimensional structure of a human connexin26 gap junction channel

reveals a plug in the vestibule. *Proc Natl Acad Sci U S A* **104**, 10034-10039, doi:10.1073/pnas.0703704104 (2007).

152 Fleishman, S. J., Unger, V. M., Yeager, M. & Ben-Tal, N. A Calpha model for the transmembrane alpha helices of gap junction intercellular channels. *Mol Cell* **15**, 879-888, doi:10.1016/j.molcel.2004.08.016 (2004).

153 Makowski, L., Caspar, D. L., Phillips, W. C. & Goodenough, D. A. Gap junction structures. V. Structural chemistry inferred from X-ray diffraction measurements on sucrose accessibility and trypsin susceptibility. *J Mol Biol* **174**, 449-481 (1984).

154 Stebbings, L. A. *et al.* Gap junctions in Drosophila: developmental expression of the entire innexin gene family. *Mech Dev* **113**, 197-205 (2002).

155 Bauer, R. *et al.* Intercellular communication: the Drosophila innexin multiprotein family of gap junction proteins. *Chem Biol* **12**, 515-526, doi:10.1016/j.chembiol.2005.02.013 (2005).

156 Altun, Z. F., Chen, B., Wang, Z. W. & Hall, D. H. High resolution map of Caenorhabditis elegans gap junction proteins. *Dev Dyn* **238**, 1936-1950, doi:10.1002/dvdy.22025 (2009).

157 Phelan, P. *et al.* Mutations in shaking-B prevent electrical synapse formation in the Drosophila giant fiber system. *J Neurosci* **16**, 1101-1113 (1996).

158 Bauer, R., Lehmann, C., Martini, J., Eckardt, F. & Hoch, M. Gap junction channel protein innexin 2 is essential for epithelial morphogenesis in the Drosophila embryo. *Mol Biol Cell* **15**, 2992-3004, doi:10.1091/mbc.e04-01-0056 (2004).

159 Starich, T. A., Lee, R. Y., Panzarella, C., Avery, L. & Shaw, J. E. eat-5 and unc-7 represent a multigene family in Caenorhabditis elegans involved in cell-cell coupling. *J Cell Biol* **134**, 537-548 (1996).

160 Starich, T. A., Miller, A., Nguyen, R. L., Hall, D. H. & Shaw, J. E. The Caenorhabditis elegans innexin INX-3 is localized to gap junctions and is essential for embryonic development. *Dev Biol* **256**, 403-417 (2003).

161 Jentsch, T. J. VRACs and other ion channels and transporters in the regulation of cell volume and beyond. *Nat Rev Mol Cell Biol* **17**, 293-307, doi:10.1038/nrm.2016.29 (2016).

162 Pedersen, S. F., Okada, Y. & Nilius, B. Biophysics and Physiology of the Volume-Regulated Anion Channel (VRAC)/Volume-Sensitive Outwardly Rectifying Anion Channel (VSOR). *Pflugers Arch* **468**, 371-383, doi:10.1007/s00424-015-1781-6 (2016).

163 Hyzinski-García, M. C., Rudkouskaya, A. & Mongin, A. A. LRRC8A protein is indispensable for swelling-activated and ATP-induced release of excitatory amino acids in rat astrocytes. *J Physiol* **592**, 4855-4862, doi:10.1113/jphysiol.2014.278887 (2014).

164 Zhang, Y. *et al.* SWELL1 is a regulator of adipocyte size, insulin signalling and glucose homeostasis. *Nat Cell Biol* **19**, 504-517, doi:10.1038/ncb3514 (2017).

165 Planells-Cases, R. *et al.* Subunit composition of VRAC channels determines substrate specificity and cellular resistance to Pt-based anti-cancer drugs. *EMBO J* **34**, 2993-3008, doi:10.15252/embj.201592409 (2015).
166 Kubota, K. *et al.* LRRC8 involved in B cell development belongs to a novel family of leucine-rich repeat proteins. *FEBS Lett* **564**, 147-152, doi:10.1016/S0014-5793(04)00332-1 (2004).
167 Ye, Z. C., Oberheim, N., Kettenmann, H. & Ransom, B. R. Pharmacological "cross-inhibition" of connexin hemichannels and swelling activated anion channels. *Glia* **57**, 258-269, doi:10.1002/glia.20754 (2009).
168 Gaitán-Peñas, H. *et al.* Investigation of LRRC8-Mediated Volume-Regulated Anion Currents in Xenopus Oocytes. *Biophys J* **111**, 1429-1443, doi:10.1016/j.bpj.2016.08.030 (2016).
169 Syeda, R. *et al.* LRRC8 Proteins Form Volume-Regulated Anion Channels that Sense Ionic Strength. *Cell* **164**, 499-511, doi:10.1016/j.cell.2015.12.031 (2016).
170 Vergis, J. M., Purdy, M. D. & Wiener, M. C. A high-throughput differential filtration assay to screen and select detergents for membrane proteins. *Anal Biochem* **407**, 1-11, doi:10.1016/j.ab.2010.07.019 (2010).
171 Tribet, C., Audebert, R. & Popot, J. L. Amphipols: polymers that keep membrane proteins soluble in aqueous solutions. *Proc Natl Acad Sci U S A* **93**, 15047-15050 (1996).
172 Althoff, T., Mills, D. J., Popot, J. L. & Kühlbrandt, W. Arrangement of electron transport chain components in bovine mitochondrial supercomplex I1III2IV1. *EMBO J* **30**, 4652-4664, doi:10.1038/emboj.2011.324 (2011).
173 Ludtke, S. J., Baldwin, P. R. & Chiu, W. EMAN: semiautomated software for high-resolution single-particle reconstructions. *J Struct Biol* **128**, 82-97, doi:10.1006/jsbi.1999.4174 (1999).
174 Alexandrov, A. I., Mileni, M., Chien, E. Y., Hanson, M. A. & Stevens, R. C. Microscale fluorescent thermal stability assay for membrane proteins. *Structure* **16**, 351-359, doi:10.1016/j.str.2008.02.004 (2008).
175 Adair, B. D. & Yeager, M. Electron microscopy of integrins. *Methods Enzymol* **426**, 337-373, doi:10.1016/S0076-6879(07)26015-X (2007).
176 Scheres, S. H. RELION: implementation of a Bayesian approach to cryo-EM structure determination. *J Struct Biol* **180**, 519-530, doi:10.1016/j.jsb.2012.09.006 (2012).
177 Cheng, Y., Grigorieff, N., Penczek, P. A. & Walz, T. A primer to single-particle cryo-electron microscopy. *Cell* **161**, 438-449, doi:10.1016/j.cell.2015.03.050 (2015).
178 Rosenthal, P. B. & Henderson, R. Optimal determination of particle orientation, absolute hand, and contrast loss in single-particle electron cryomicroscopy. *J Mol Biol* **333**, 721-745 (2003).
179 Rosenbaum, D. M. *et al.* GPCR engineering yields high-resolution structural insights into beta2-adrenergic receptor function. *Science* **318**, 1266-1273, doi:10.1126/science.1150609 (2007).

180 Cherezov, V. *et al.* High-resolution crystal structure of an engineered human beta2-adrenergic G protein-coupled receptor. *Science* **318**, 1258-1265, doi:10.1126/science.1150577 (2007).
181 Rasmussen, S. G. *et al.* Crystal structure of the β2 adrenergic receptor-Gs protein complex. *Nature* **477**, 549-555, doi:10.1038/nature10361 (2011).
182 Paulsen, C. E., Armache, J. P., Gao, Y., Cheng, Y. & Julius, D. Structure of the TRPA1 ion channel suggests regulatory mechanisms. *Nature* **520**, 511-517, doi:10.1038/nature14367 (2015).
183 Pernstich, C., Senior, L., MacInnes, K. A., Forsaith, M. & Curnow, P. Expression, purification and reconstitution of the 4-hydroxybenzoate transporter PcaK from Acinetobacter sp. ADP1. *Protein Expr Purif* **101**, 68-75, doi:10.1016/j.pep.2014.05.011 (2014).
184 Thompson, J. D., Higgins, D. G. & Gibson, T. J. CLUSTAL W: improving the sensitivity of progressive multiple sequence alignment through sequence weighting, position-specific gap penalties and weight matrix choice. *Nucleic Acids Res* **22**, 4673-4680 (1994).
185 Slotboom, D. J., Duurkens, R. H., Olieman, K. & Erkens, G. B. Static light scattering to characterize membrane proteins in detergent solution. *Methods* **46**, 73-82, doi:10.1016/j.ymeth.2008.06.012 (2008).
186 Liao, M., Cao, E., Julius, D. & Cheng, Y. Structure of the TRPV1 ion channel determined by electron cryo-microscopy. *Nature* **504**, 107-112, doi:10.1038/nature12822 (2013).
187 Lu, P. *et al.* Three-dimensional structure of human γ-secretase. *Nature* **512**, 166-170, doi:10.1038/nature13567 (2014).
188 Vanden Abeele, F. *et al.* Functional implications of calcium permeability of the channel formed by pannexin 1. *J Cell Biol* **174**, 535-546, doi:10.1083/jcb.200601115 (2006).
189 Mi, W. *et al.* Structural basis of MsbA-mediated lipopolysaccharide transport. *Nature* **549**, 233-237, doi:10.1038/nature23649 (2017).
190 Oshima, A. Structure of an innexin gap junction channel and cryo-EM sample preparation. *Microscopy (Oxf)* **66**, 371-379, doi:10.1093/jmicro/dfx035 (2017).
191 Pettersen, E. F. *et al.* UCSF Chimera--a visualization system for exploratory research and analysis. *J Comput Chem* **25**, 1605-1612, doi:10.1002/jcc.20084 (2004).
192 Michalski, K. & Kawate, T. Carbenoxolone inhibits Pannexin1 channels through interactions in the first extracellular loop. *J Gen Physiol* **147**, 165-174, doi:10.1085/jgp.201511505 (2016).
193 Ritchie, T. K. *et al.* Chapter 11 - Reconstitution of membrane proteins in phospholipid bilayer nanodiscs. *Methods Enzymol* **464**, 211-231, doi:10.1016/S0076-6879(09)64011-8 (2009).
194 Zheng, S. Q. *et al.* MotionCor2: anisotropic correction of beam-induced motion for improved cryo-electron microscopy. *Nat Methods* **14**, 331-332, doi:10.1038/nmeth.4193 (2017).

195 Zhang, K. Gctf: Real-time CTF determination and correction. *J Struct Biol* **193**, 1-12, doi:10.1016/j.jsb.2015.11.003 (2016).
196 Scheres, S. H. Semi-automated selection of cryo-EM particles in RELION-1.3. *J Struct Biol* **189**, 114-122, doi:10.1016/j.jsb.2014.11.010 (2015).
197 Punjani, A., Rubinstein, J. L., Fleet, D. J. & Brubaker, M. A. cryoSPARC: algorithms for rapid unsupervised cryo-EM structure determination. *Nat Methods* **14**, 290-296, doi:10.1038/nmeth.4169 (2017).
198 Strop, P. & Brunger, A. T. Refractive index-based determination of detergent concentration and its application to the study of membrane proteins. *Protein Sci* **14**, 2207-2211, doi:10.1110/ps.051543805 (2005).